

DISSERTATION

Studying flux pinning phenomena in BaFe_2As_2 based superconducting single crystals and single crystalline thin films

Ausgeführt zum Zwecke der Erlangung des akademischen Grades eines Doktors der
technischen Wissenschaften unter der Leitung von

Privatdoz. Dipl.-Ing. Dr. techn. Michael Eisterer
E141
Atominstitut

eingereicht an der Technischen Universität Wien
Fakultät für Physik

von

Dipl.-Ing. Ventsislav Mishev
Matrikelnummer: 0527209
Hohlweggasse 32/2/6
1030 Wien, Österreich

To my grandfather (11.4.1929-05.01.2014).

Danksagung

Als Erstes möchte ich mich bei meinem Betreuer, Michael Eisterer, für über 3 unvergesslichen Jahre bedanken. Ohne seine exzellente wissenschaftliche Betreuung wäre es für mich keinesfalls möglich, in dieser Zeit meine Dissertation zu einem erfolgreichen Ende zu bringen. Außerdem habe ich auch abseits der beruflichen Seite ein ausgezeichnetes Verhältnis mit ihm genossen, was hoffentlich noch für lange Jahre aufrecht erhalten bleibt und noch weiter sich entwickeln wird. Danke dir, Mike!

Außerdem möchte ich mich bei der ganzen Gruppe Tieftemperaturphysik und Supraleitung, geleitet vom Franz Sauerzopf, für eine wunderbare Reise durch die Welt der Physik und generell des Lebens bedanken. Alle Kollegen aus der Gruppen unterstützen mich mit allen Mitteln seit mittlerweile mehr als 5 Jahren in meiner Zeit als Student und später als Dissertant. Was noch dazu kommt ist das hervorragende soziale und Arbeitsklima, was in unserem Labor in dieser Zeit herrschte. Es ist praktisch unmöglich, alle Kollegen namentlich zu erwähnen, aber ich bedanke mich vom ganzen Herzen beim Franz, Martin, Thomas, Hannes, David Fischer, May, Rainer, Murphy, Florian und Johann.

Ein herzliches Danke schön gibt es für den ehemaligen Leiter unserer Gruppe, Harald Weber, der mich seit meinem ersten Tag in der Gruppe als Student förderte und eine große Rolle bei meinen Fortschritten in der Wissenschaft spielte. Ohne ihn hätte ich die Chance nicht gehabt, die wunderbare Welt der Supraleitung in diesem Licht kennen zu lernen.

Ich möchte mich auch sehr, sehr herzlich bei meinen Kollegen aus Japan bedanken. Die Gruppe in AIST, geleitet vom Hiroshi Eisaki, hat die Proben hergestellt, die diese Arbeit ermöglichten und ich hatte auch die Ehre ein ausgezeichnetes Verhältnis mit allen Mitgliedern derselben zu genießen. Außerdem möchte ich mich bei Yoshihiko Takano, Leiter unserer Partnergruppe in NIMS, bedanken, da er mir die Chance gab, für 4 Monate in seiner Gruppe in Tsukuba zu arbeiten. Hiroshi, Takano-san, minna-san: Arigatou

godzaimasu!

Ich möchte mich besonders bei meinen Eltern bedanken für ihre Bemühungen, mir einen guten Start im Leben zu geben und dann später bei meiner Seite zu stehen als ich Hilfe brauchte. Besonders möchte ich auch meinen Großeltern danken, vor allem meiner Großmutter, die in den letzten knappen 10 Jahren sich immer um mich kümmerte wie ich meine Heimat besuchte. Auch bei meiner Schwester bedanke ich mich für die moralische Unterstützung.

An dieser Stelle möchte ich mich bei meinen Freunden für Alles bedanken, was sie für mich getan haben und noch immer tun. Ich fühle mich gesegnet, da ich während meiner bescheidenen Lebensdauer bereits so zahlreiche fantastische Leute kennen lernen konnte. Es ist wirklich schwer, alle an dieser Stelle zu erwähnen, aber ich werde es mir trotzdem erlauben, ein paar Namen explizit zu schreiben. Ich danke euch, Lorenz und Georgi, Josef, Bernie, Maxi, Oli, Wolfi, Martin, Stefan, Nasko, Vladi, Ani, Megi, Kremi, Natalia und Olga. Und ein kräftiges Danke an das ganze Tsukubateam! Die Zeiten mit euch bleiben für immer in meinem Herzen.

Und hier möchte ich ein sehr spezielles Danke an meiner Lebensgefährtin, Lili, aussprechen. Ohne sie wäre mein Leben eine viel ... düstere Angelegenheit. Danke dir, Lili, für Alles.

Kurzfassung

Das Hauptziel dieser Dissertation ist die Erforschung von Flussverankerung in BaFe_2As_2 basierten supraleitenden Einkristallen und einkristallinen dünnen Filmen mittels unterschiedlichen experimentellen Techniken sowie die theoretische Beschreibung von diesem Phänomen. Supraleitung kann entweder durch externen Druck oder durch Dotierung in diesem Material hervorgerufen werden. Für diese Studie stehen hochqualitative Einkristalle zur Verfügung. Die unterschiedliche Dotierung hat wesentlichen Einfluss auf die supraleitende Eigenschaften der Kristalle, vor allem bei wichtigen Parameter wie die Übergangstemperatur T_c , die kritische Stromdichte J_c , das obere kritische Feld B_{c2} und das Irreversibilitätsfeld B_{irr} .

Das Ziel der Dissertation ist, ein vertieftes Verständnis in die Eigenschaften der unterschiedlich dotierten Einkristalle zu bekommen und anhand der gewonnenen Informationen die Kristalle untereinander zu vergleichen. Um dieses Ziel zu erreichen, werden gut etablierte Messmethoden aus dem Bereich der Supraleitung wie zum Beispiel Magnetisierungs- und Transportstrommessungen angewandt. Die Letzteren sind für das Bestimmen der Irreversibilitätslinien in Einkristallen sowie die kritischen Stromdichten in dünnen Filmen geeignet. Magnetisierungsmessungen sind vor allem bei der Bestimmung von der Übergangstemperatur und der kritischen Stromdichte in supraleitenden Einkristallen nützlich. Der Grund warum J_c aus Magnetisierungsmessungen bestimmt werden muss ist die Tatsache, dass makroskopische Transportströme von über 1000 A für Proben mit größerem Querschnitt und hohen kritischen Stromdichten nötig wären.

Winkelaufgelöste Magnetisierungsmessungen von Einkristallen sind besonders interessant. Diese stellen gleichzeitig große Herausforderungen was die Auswertung der experimentellen Messergebnisse anbetrifft. Die größte Schwierigkeit ist das Verändern des kritischen Zustandes für unterschiedliche Orientierungen im externen Magnetfeld. Zusätzlich muss noch berücksichtigt werden, dass die kritischen Ströme, im Gegensatz zu

Transportstrommessungen an dünnen Filmen, nicht nur eine vorgegebene Richtung haben. Dieses Messungsartefakt verursacht eine weitere Komplikation, nämlich Ströme, die variablen Lorentzkraften ausgesetzt werden, je nach Orientierung des Kristalls und der Stromschleifen zu dem angelegten Feld. Die korrekte Auswertung dieses komplexen Experimentes wird in dieser Studie erfolgreich durchgeführt und es werden zahlreiche hochinteressante Ergebnisse bezüglich der Anisotropie der kritischen Stromdichte in Einkristallen sowohl im schwachen als auch im starken Verankerungslimit gewonnen.

Ein weiteres interessantes Forschungsthema sind die winkelaufgelösten Transportstrommessungen an dünnen Filmen, vor allem wenn Drehungen um zwei aufeinander orthogonalen Achsen möglich sind. So ein Messaufbau ermöglicht eine extensive Studie des Einflusses der Orientierung und Größe der Lorentzkraft auf die kritische Stromdichte. In dieser Dissertation wird der Fall von planaren Defekten in einem einkristallinen Dünnsfilm erforscht. Die erhaltenen Ergebnisse ermöglichten das Postulieren eines Modells für die kritische Stromdichte in diesem Grenzfall, wobei nur ein einziger Parameter benötigt wurde.

Ein weiterer Punkt der von Interesse ist, ist der Einfluss von artifiziellen Verankerungszentren auf die supraleitenden Eigenschaften der unterschiedlich dotierten Einkristalle. Dies ist vor allem deswegen wichtig, da das Optimieren der Flussverankerung in supraleitenden Materialien für deren Relevanz für technologische Anwendungen eine entscheidende Rolle spielt. Bestrahlung mit schnellen Neutronen stellt eine Möglichkeit dar, eine isotrope und stark verankernde Defektstruktur in den Supraleitern zu erzeugen. Eine umfassende Studie der Effekte dieser Bestrahlungstechnik auf T_c , J_c , B_{c2} , B_{irr} wurde durchgeführt, zahlreiche wichtige Ergebnisse wurden erzielt, unter anderem die bis dato höchste gemessene kritische Stromdichte in einem $BaFe_2As_2$ basierten Einkristall (nach dem besten Wissen des Autors).

Abstract

The main goal of this PhD thesis is the study of flux pinning phenomena in BaFe_2As_2 based superconducting single crystals and single crystalline thin films through various experimental techniques and their theoretical description. Superconductivity in this system is induced either by applying pressure or by doping. High quality crystals with different dopants are available for this study. The difference in the dopant has a profound impact on the various superconducting properties of the crystals, especially benchmark values such as the transition temperature T_c , the critical current density J_c , the upper critical field B_{c2} and irreversibility line B_{irr} .

The aim of the thesis is to obtain insight into the properties of the differently doped crystals and to compare them to each other. In order to achieve this objective, established techniques within the field of superconductivity such as magnetization and transport measurements will be utilized. The latter are useful for the determination of the irreversibility line of bulk samples as well as the critical current densities in thin films. Magnetization measurements, on the other hand, can be utilized in order to establish the transition temperature as well as J_c in single crystals. The reason why J_c has to be evaluated from magnetization measurements are the high macroscopic currents which can reach values above 10^3 A for crystals with a large cross section and high critical currents.

Angle-resolved magnetization measurements on single crystals are of particular interest. They represent a significant challenge with regard to the evaluation of the experimental results. The main difficulty is posed by the changes in the critical state for different orientations in an external applied field. Furthermore, the supercurrents do not flow in the same direction during magnetization measurements as is the case in thin films during transport measurements. This leads to the additional complication of currents exposed to variable Lorentz forces depending on the orientation of the sample and the current loops with regard to the applied magnetic field. The proper evaluation of this complex

experiment is performed successfully within this study, revealing highly interesting results regarding the anisotropy of the critical current density in single crystals in the weak and strong pinning limits.

Another intriguing research topic are angle-resolved transport current measurements on thin films involving rotation along two axes orthogonal to each other. Such a setup allows a thorough study of the influence of the direction and magnitude of the Lorentz force on the critical current density. In this thesis, the case of pinning by planar defects in a single crystalline film was examined. The obtained results allowed the establishment of a scaling model for the critical current density in this pinning scenario by using a single parameter.

One further point of interest is the influence of artificial pinning centers on the superconducting properties of the individual single crystals. This is an important facet particularly when considering the suitability of a given material for technological applications. Fast neutron irradiation enables the creation of an isotropic and strongly pinning defect structure in the crystals. A thorough study was subsequently carried out on T_c , J_c , B_{c2} and the irreversibility line B_{irr} which returned multiple valuable results, among them the highest, to the author's knowledge, critical current densities in a BaFe_2As_2 based superconductor measured until the present day.

List of Symbols

| | |
|--------------------------|--|
| α | Angle between the applied field and the c -axis of the film in the 6 T setup; Angle used to explain the anisotropic Bean model |
| χ | Magnetic susceptibility |
| ΔT_c | Superconducting transition width |
| δT_c | Decrease in the transition temperature after irradiation |
| ϵ | Scaling parameter |
| η | Critical current anisotropy in the main orientations $\frac{J_c(H\ ab)}{J_c(H\ c)}$ |
| η_{pin} | Effective pinning parameter |
| γ | Anisotropy of the upper critical field |
| κ | Ginzburg-Landau parameter |
| λ | Magnetic penetration depth |
| λ_{ab} | Magnetic penetration depth within the ab -planes |
| μ_0 | Vacuum permeability |
| ϕ_0 | Elementary flux quantum |
| Φ_t | Fast neutron fluence |
| ρ, ρ_{lt} | Electric resistivity |
| σ_{ns} | Phase boundary energy per unit area |
| φ, θ | Rotation angles in the 6 T setup |

| | |
|-----------------------------------|---|
| ϑ | Angle between the applied field and the c -axis of the superconductor |
| ϑ_B | Angle between B and the c -axis |
| $\vec{e}_1, \vec{e}_2, \vec{e}_3$ | Unit vectors in the film coordinate system |
| \vec{H}_s | Stray magnetic field |
| \vec{r} | Distance vector |
| $\xi(0K)$ | Projected coherence at 0 K |
| ξ | Coherence length |
| ξ_{ab} | Coherence length within the ab -planes |
| ξ_c | Coherence length along the c -axis |
| A | Cross-section of a crystal |
| a, b, c | Geometric dimensions of a superconductor |
| ab – planes | The planes spanned by the [100] and [010] crystallographic directions |
| B | Magnetic induction |
| b | Reduced field |
| B^*, H^* | Bean penetration field |
| B^\perp | Out-of-plane component of the magnetic induction |
| B_{c1}, H_{c1} | Lower critical field |
| B_{c2}, H_{c2} | Upper critical field |
| B_{c2}^c, B_{c2}^{ab} | Upper critical fields in the main orientations |
| B_c, H_c | Thermodynamical critical magnetic field |
| B_{irr} | Irreversibility field |
| B_{irr}^c, B_{irr}^{ab} | Irreversibility fields in the main orientations |
| B_{onset} | Onset field of the second maximum in the critical current density |

| | |
|--------------------------------|---|
| $B_{\text{sf}}, H_{\text{sf}}$ | Self-field of the superconductor |
| c – axis | The [001] direction in Ba-122 based superconductors |
| D | Demagnetization factor |
| E | Electric field; Energy |
| E_{cr} | Electric field criterion |
| E_{c} | Condensation energy |
| E_{p} | Pinning energy |
| F_{L} | Lorentz force |
| F_{L}^{\parallel} | In-plane Lorentz force component |
| F_{L}^{\perp} | Out-of-plane Lorentz force component |
| f_{p} | Elementary pinning force |
| $F_{\text{p}}^{\text{max}}$ | Maximum volume pinning force |
| $F_{\text{V}}, F_{\text{p}}$ | Volume pinning force |
| H | Magnetic field |
| H_{a} | Applied or external magnetic field |
| h_{peak} | Peak position of the volume pinning force |
| H_{rem} | Remanent field of a superconducting magnet |
| I | Transport current |
| I_{c} | Transport critical current |
| J | Current density |
| J_{c} | Critical current density under maximum Lorentz force |
| $J_{\text{c}}^{\text{VLF}}$ | Critical current density under variable Lorentz force |

| | |
|-----------------------|---|
| J_c^a, J_c^b, J_c^c | Critical current densities along the respective side/crystallographic direction of the superconductor |
| J_c^{ab} | In-plane critical current density |
| J_d | Depairing current density |
| l | Distance between the voltage leads in transport measurements |
| M | Magnetization |
| m | Magnetic moment |
| m_-, m_+ | Branches of the magnetic moment in magnetization loops |
| m_{irr} | Irreversible magnetic moment |
| n | n-value |
| R | Electric resistance |
| r | Rotation axis in the vector Vibrating Sample Magnetometer |
| r_d | Radius of irradiation-induced defect |
| T | Temperature |
| t | Reduced temperature |
| $T^{10\%}, T^{90\%}$ | Temperatures at 10% and 90% of the maximum response signal in susceptibility measurements |
| T_c | Transition temperature |
| T_c^{mid} | Transition temperature as determined from the middle of the superconducting transition |
| T_c^{onset} | Transition temperature as determined from the onset of superconductivity |
| U | Voltage |
| $U^{90\%}, U^{10\%}$ | 90% and 10% of the voltage during resistive measurements |

| | |
|---------------------|--|
| U_c | Voltage criterion |
| U_{offset} | Offset voltage |
| V | Volume |
| v_{sh} | Shielding fraction |
| V_s | Volume shielded by the Meissner currents |
| RRR | Residual resistivity ratio |

Contents

| | | |
|----------|---|-----------|
| 1 | Introduction | 21 |
| 2 | Theory | 23 |
| 2.1 | Type-I and type-II superconductors | 23 |
| 2.2 | Bean model of the critical state | 26 |
| 2.3 | Transport critical current density | 29 |
| 2.4 | Anisotropy of the upper critical field | 30 |
| 3 | Samples | 32 |
| 3.1 | Single crystals | 32 |
| 3.2 | Thin films | 33 |
| 4 | Experiment | 38 |
| 4.1 | Magnetometry | 38 |
| 4.1.1 | Susceptibility measurements in a 1 T SQUID | 38 |
| 4.1.2 | Magnetization loops in a 7 T SQUID | 40 |
| 4.1.3 | Angle resolved magnetization loops in a vector Vibrating Sample Magnetometer | 43 |
| 4.2 | Transport current measurements | 46 |
| 4.2.1 | 6 T system | 46 |
| 4.2.2 | 17 T system | 51 |
| 4.3 | Fast neutron irradiation | 52 |
| 5 | Results and discussion | 55 |
| 5.1 | Critical current anisotropy of the Co-doped BaFe ₂ As ₂ thin film | 55 |
| 5.2 | Critical current anisotropy in Ba-122 based superconducting single crystals | 65 |

| | | |
|----------|--|------------|
| 5.3 | Effects of fast neutron irradiation | 76 |
| 5.3.1 | Changes in the transition temperature | 76 |
| 5.3.2 | Changes in the in-plane critical current density after neutron irradiation | 81 |
| 5.3.3 | The J_c -anisotropy conundrum for $H_a \parallel ab$ | 92 |
| 5.3.4 | Upper critical fields, irreversibility lines and coherence lengths | 93 |
| 5.3.5 | Analysis of the volume pinning force | 102 |
| 6 | Conclusion | 105 |

List of Figures

| | | |
|-----|---|----|
| 2.1 | Magnetization of an ideal (a) and real (b) type-I superconductor in an external applied field | 24 |
| 2.2 | Magnetization curve of a clean type-II superconductor | 25 |
| 2.3 | Graphic representation of a clean type-II superconductor (left) and one with pinning centers (right) [27] | 27 |
| 2.4 | Bean model of the critical state (figure taken from the original publication [26]) | 28 |
| 3.1 | Phase diagram of the Ba-122 system (from [38]). The top panel shows the emergence of superconductivity with doping, while the bottom panel reveals the effect of applied external pressure on the parent BaFe_2As_2 compound. | 34 |
| 3.2 | Crystallography of the Ba-122 parent compound | 35 |
| 3.3 | An enlarged image of the Co-doped Ba-122 single crystal Co#4 (dimensions available in Tab. 3.1 | 35 |
| 3.4 | Hall scan of the remanent magnetic profile in a pristine K-doped single crystal at $T= 10$ K | 36 |
| 3.5 | (a) An optical image of the Co-doped Ba-122 thin film; (b) A TEM picture (performed by E Reich, IFW Dresden) taken parallel to the a -axis which reveals planar defects aligned with the Fe-As planes of the film | 37 |
| 4.1 | An example for the evaluation of the AC susceptibility measurement on a single crystal | 39 |
| 4.2 | Magnetization loops at different temperatures after zero-field cooling | 41 |
| 4.3 | Magnetization loops at different temperatures after field-cooling at 7 T | 42 |

| | | |
|------|--|----|
| 4.4 | Sample curves from the VSM with r parallel to either a (left panel) or b (right panel) for $\angle(H_a, c) = 75^\circ$ | 45 |
| 4.5 | Evaluation of T_c of a Co-doped BaFe ₂ As ₂ from a resistive measurement | 47 |
| 4.6 | I_c evaluation via power-law fit | 49 |
| 4.7 | Rotation axes in the two-axes goniometer | 50 |
| 4.8 | Different configurations for the two-axes goniometer measurements | 50 |
| 4.9 | Sample resistive transitions and the evaluation criteria used to obtain B_{c2} and B_{irr} in the particular orientation | 52 |
| 4.10 | Connection adapter used for resistive measurements in the 17 T setup | 53 |
| 5.1 | J_c anisotropy in the Co-doped Ba-122 film at different temperatures and fields in the maximum Lorentz force configuration | 56 |
| 5.2 | Anisotropy of the critical current density in the main orientations for different fields and temperatures | 57 |
| 5.3 | $J_c(\varphi = 90^\circ)$ at different fields and temperatures | 59 |
| 5.4 | VLF scans of the Co-doped Ba-122 film at different temperatures and angles φ | 60 |
| 5.5 | In-plane scan at 15 K and different fields | 61 |
| 5.6 | Highly zoomed-in image around $\varphi = 90^\circ$ at 15 K and 6 T | 62 |
| 5.7 | Dependence of the critical current density on α for different temperatures and fields | 64 |
| 5.8 | Scaling of the critical current density to the out-of-plane component of the magnetic field at 10 K | 65 |
| 5.9 | J_c in differently doped Ba-122 single crystals in the main orientation $\vartheta = 0^\circ (H_a \parallel c)$ | 68 |
| 5.10 | $J_c(\vartheta)$ of K#4 at 25 K and different fields (left panel) and application of pure field scaling to the results (right panel) | 70 |
| 5.11 | Angular evolution of the fishtail effect in a Co-doped Ba-122 single crystal at 17.5 K | 71 |
| 5.12 | $J_c(\vartheta)$ of Co#1 at 17.5 K and different fields (left panel) and application of pure field scaling to the results (right panel) | 72 |
| 5.13 | $J_c(\vartheta)$ of Co#3 at 17.5 K and different fields (left panel) and application of both field and critical current scaling to the results (right panel) | 73 |

| | | |
|------|--|----|
| 5.14 | The figure shows the significance of the size of a defect which pins a vortex core. a) shows an unpinned vortex core for $H_a \parallel c$, while d) illustrates the shrinkage of a vortex core with θ . b) and e) show the change in the pinning energy from $E_p \propto \xi_{ab}^2 r_d$ to $E_p \propto \xi_{ab}^2 \epsilon(\theta) r_d$ due to the interaction of a large defect (radius $\geq \xi_{ab}$) with the vortex core in each case, while c) and f) illustrate the constant pinning energy ($E_p \propto r_d^3$) when a small defect pins the vortex core. | 74 |
| 5.15 | T_c in differently doped Ba-122 single crystals in the pristine state and after irradiation to different fast neutron fluences | 77 |
| 5.16 | Energy dependence of the neutron fluence in the TRIGA-MARK II reactor in the Atominstitut [91] | 79 |
| 5.17 | J_c in a Co-doped Ba-122 single crystal pristine and after irradiation to different fast neutron fluences | 82 |
| 5.18 | J_c in a P-doped Ba-122 single crystal pristine and after irradiation to different fast neutron fluences | 85 |
| 5.19 | B_{onset} of the pristine Co- and P-doped crystals | 86 |
| 5.20 | Difference in the magnetic moment in two subsequent magnetization measurements in the SQUID (solid line) and in the VSM (dotted line) | 88 |
| 5.21 | J_c in a K-doped Ba-122 single crystal pristine and after irradiation to different fast neutron fluences | 89 |
| 5.22 | Resistive transitions for the three crystal types in the pristine state . . . | 95 |
| 5.23 | Resistive transitions for the three crystal types after irradiation to $\Phi_t = 1.8 \times 10^{21} \text{ m}^{-2}$ | 96 |
| 5.24 | Resistive transitions for the three crystal types after irradiation to $\Phi_t = 3.6 \times 10^{21} \text{ m}^{-2}$ | 97 |
| 5.25 | B_{c2S} and ILs of the differently doped Ba-122 single crystals: (a) Co-doped crystal, pristine; (b) Co-doped crystal, $\Phi_t = 1.8 \times 10^{21} \text{ m}^{-2}$; (c) Co-doped crystal, $\Phi_t = 3.6 \times 10^{21} \text{ m}^{-2}$; (d) P-doped crystal, pristine; (e) P-doped crystal, $\Phi_t = 1.8 \times 10^{21} \text{ m}^{-2}$; (f) P-doped crystal, $\Phi_t = 3.6 \times 10^{21} \text{ m}^{-2}$; (g) K-doped crystal, pristine; (h) K-doped crystal, $\Phi_t = 1.8 \times 10^{21} \text{ m}^{-2}$; (i) K-doped crystal, $\Phi_t = 3.6 \times 10^{21} \text{ m}^{-2}$; | 99 |

| | |
|--|-----|
| 5.26 Normalized volume pinning force as a function of the reduced field in pristine (left panel) and irradiated (right panel) differently doped Ba-122 single crystals | 103 |
|--|-----|

List of Tables

| | | |
|-----|--|-----|
| 3.1 | Nomenclature of the single crystals examined within the thesis | 34 |
| 5.1 | T_c s and transition widths of the single crystals before and after irradiation | 78 |
| 5.2 | Depairing current density and effective pinning parameter of the differently doped single crystals | 91 |
| 5.3 | Resistivity ratios of the pristine and irradiated crystals | 98 |
| 5.4 | Extrapolated coherence lengths in the pristine single crystals | 102 |

Chapter 1

Introduction

The discovery of superconductivity at a temperature of 26 K in the iron-based compound $\text{LaO}_{1-x}\text{F}_x\text{FeAs}$ ($x = 0.05-0.12$) (1111 system) by Kamihara et al [1] brought enthusiasm and renewed vigor to the superconductivity community. Scores of new iron-based superconductor families were discovered in a matter of months, among them the so-called pnictides. The name ‘pnictides’ is used for chemical compositions which include one of the elements from the 5th group (N, P, As, Sb, Bi) as the anion. Among the most promising of the iron-based superconductors is the BaFe_2As_2 family (Ba-122 system). The parent compound is typically doped with different dopants [2, 3, 4, 5]. As of the present moment, transition temperatures of almost 40 K have been attained in potassium-doped Ba-122 system [3], while upper critical fields B_{c2} above 100 T also have been reported for the same superconductor [6]. The 122 system also shows a very moderate B_{c2} anisotropy $\gamma = \frac{B_{c2}^{ab}}{B_{c2}^c}$ of less than 2 at low temperatures [7, 8]. This is in stark contrast to the higher T_c cuprate superconductors which typically show γ of over five. The combination of these physical properties makes this material a very interesting research topic not only in terms of fundamental physics, but also in view of possible technological applications. The Ba-122 family is of great interest due to its very high upper critical fields and also relatively cheap production costs. There have already been reports of very high critical currents in wires with Ba-122 based superconductors [9]. Additionally, there are high hopes that the new discovery could also provide new insight into the long-standing question regarding the theory of high-temperature superconductivity.

One of the main research areas covers the phenomenon of flux pinning in the Ba-122 family. It is of crucial importance to applications in particular due to its paramount im-

portance for achieving high critical currents. Accordingly, a lot of effort has been invested into examining the influence of doping and introducing artificial pinning centers by particle irradiation [10, 11, 12, 13, 14] on the flux pinning properties of the Ba-122 family. The introduction of a pinning landscape into a superconductor can influence its fundamental parameters, including the transition temperature, critical current density, upper critical field and irreversibility line. A careful study is necessary in order to quantify these changes. While polycrystalline materials are required for the fabrication of superconducting wires, cables and tapes, it is important to understand flux pinning within a single grain first before the problem of granularity can be tackled. This is made possible by the production and subsequent study of high-quality Ba-122 single crystals and single crystalline thin films. The effects of doping, the introduction of artificial pinning centers and the sample geometry (bulks or thin films) within the Ba-122 family are analyzed in this thesis.

Chapter 2

Theory

2.1 Type-I and type-II superconductors

The differences between type-I and type-II superconductors are examined in detail by Abrikosov [15] within the framework of the Ginzburg-Landau theory [16]. Iron-based superconductors, like all technologically relevant superconducting materials, are type-II superconductors. The main difference between type-I and type-II superconductors, easily observed in simple magnetization curves ($M - H$ curves), is their respective interaction with a magnetic field. The former exhibit an ideal diamagnetic behaviour (magnetic susceptibility $\chi = -1$), also known as the Meissner-Ochsenfeld effect [17], shielding the externally applied field almost entirely. The field can only penetrate the superconductor within the so-called magnetic penetration depth λ when demagnetization effects are neglected. This behavior holds with increasing applied field H_a until the critical field H_c is reached, when an abrupt drop in the magnetization M is observed, indicating that the sample is no longer in the superconducting state (see Fig.2.1(a)). However, this ideal curve cannot be achieved for real samples due to their finite geometry. For a real type-I superconductor, the demagnetization factor D changes the effective field and forces a flux penetration into the superconductor. The magnetization curve is altered as a result (see Fig. 2.1(b)). A new state called the ‘intermediate state’ is introduced. The Ginzburg-Landau theory predicts that the only stable solution to this physical problem is represented by an array of alternating superconducting and normally conducting regions in the superconductor. The first experimental proof of the intermediate state was provided by Meshkovsky [18]. Multiple experimental results subsequently showed the

existence of a lamella-like structure [19, 20, 21] when a type-I superconductor is in the intermediate state.

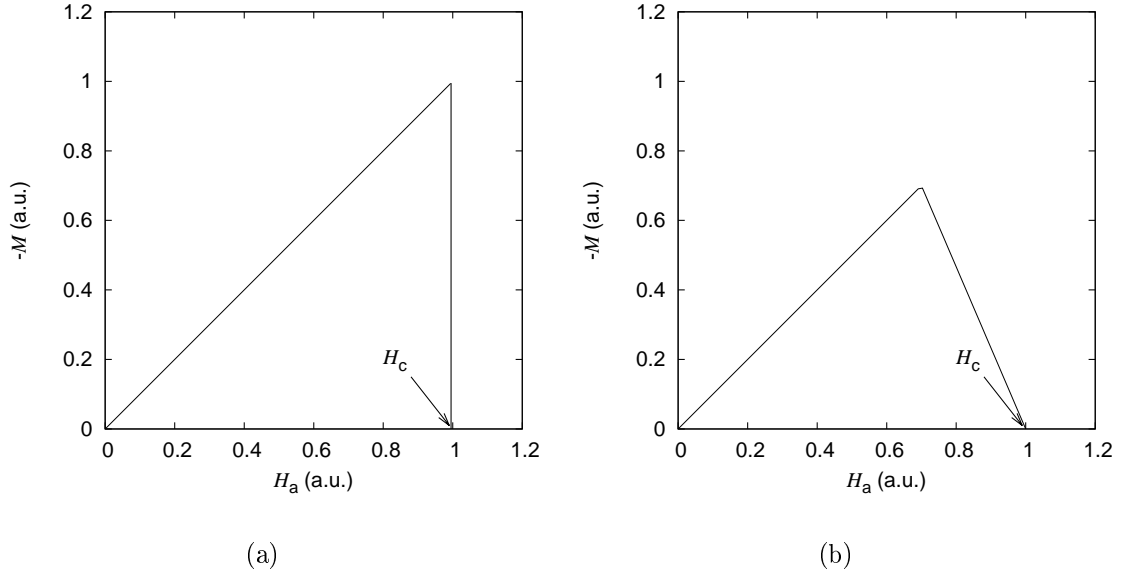


Figure 2.1: Magnetization of an ideal (a) and real (b) type-I superconductor in an external applied field

Type-II superconductors also have a Meissner phase where the whole volume of an ideal type-II superconductor, with the exception of the London penetration depth, is shielded if an external magnetic field is applied. However, this behavior no longer persists over the whole phase diagram, even for an ideal sample. The magnetic flux enters these materials at a material-dependent field called the lower critical field H_{c1} without destroying superconductivity in the whole volume of the sample. The flux penetrates the superconductor in the form of flux lines, which are typically aligned in a hexagonal lattice [22] in the case of a clean type-II superconductor. The individual flux lines can move freely through the sample when a force is applied on them (for instance Lorentz force F_L) if there is no mechanism to pin them down. The magnetization curve of a clean type-II superconductor can be observed in Fig. 2.2. Superconductivity persists in the sample up to an upper critical field H_{c2} and the magnetization is reversible.

The reason for the different behavior of the two superconductor types is found in the phase boundary energy per unit area σ_{ns} ('ns' denotes normally conducting and

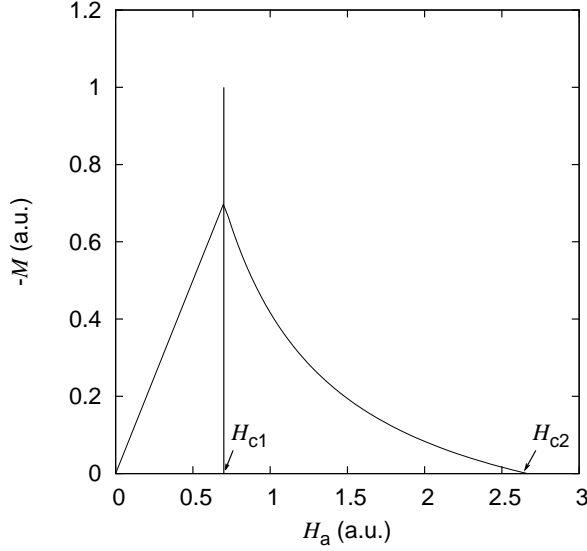


Figure 2.2: Magnetization curve of a clean type-II superconductor

superconducting). With the help of the Ginzburg-Landau parameter κ

$$\kappa = \frac{\lambda}{\xi} \quad (2.1)$$

where ξ is the coherence length, it is possible to examine whether building an additional phase boundary is energetically advantageous. σ_{ns} can be calculated for the the two extreme cases of $\kappa \ll 1$ and $\kappa \gg 1$, i. e. $\xi \gg \lambda$ and $\xi \ll \lambda$, respectively. The following solutions are obtained:

$$\sigma_{\text{ns}} = 1.89\xi\mu_0 \frac{H_c^2}{2}, \text{ for } \kappa \ll 1 \quad (2.2)$$

$$\sigma_{\text{ns}} = -1.1\lambda\mu_0 \frac{H_c^2}{2}, \text{ for } \kappa \gg 1 \quad (2.3)$$

Concurrently, the term becomes zero for $\kappa = \frac{1}{\sqrt{2}} = 0.707$. This means that superconductors with a very low κ have to use up energy when a new phase boundary between normally conducting and superconducting regions is created. By contrast, when κ is rather high, it is energetically favorable to maximize the boundary area. Therefore, magnetic flux penetrates type-II superconductors as flux lines, thus balancing between the energy gained (phase boundary energy) and lost (condensation energy in the volume permeated by flux).

Typically, the mixed state of a type-II superconductor spans a significantly larger

region than its Meissner state. The upper field limit is given by $H_{c2}(T)$ (or $B_{c2}(T)$) which can be calculated from the following equation:

$$B_{c2}(T) = \frac{\phi_0}{2\pi\mu_0\xi^2(T)} \quad (2.4)$$

where $\phi_0 = 2.07 \cdot 10^{-15}$ Wb is the elementary flux quantum. Subsequently, $\xi(T)$ can be expressed directly from Eq. 2.4:

$$\xi(T) = \sqrt{\frac{\phi_0}{2\pi\mu_0 B_{c2}(T)}} \quad (2.5)$$

Since it is difficult to obtain $B_{c2}(T)$ at low temperatures due its rather high values, $\xi(T)$ can be estimated with the help of a fit function of the following form:

$$\xi(T) = \xi(0 \text{ K})(1 - t^{1.5})^{-0.5} \quad (2.6)$$

where $t = \frac{T}{T_c}$ is the so called reduced temperature.

2.2 Bean model of the critical state

The previous section describes ideal type-II superconductors and their fundamental differences to type-I superconductors. An ‘ideal’ type-II superconductor is a clean one, i. e. there are no crystallographic defects such as dislocations, planar defects, substitute or missing atoms, among others. The consequence is that flux lines can move freely within the sample, resulting in a reversible $M(H)$ dependence (see Fig. 2.2). However, in reality it is common that there are crystallographic defects present in the superconductor which can pin the flux lines. In a real superconductor, i. e. in the presence of randomly distributed crystallographic defects which pin the flux lines, if a sufficiently small current is transported through the sample in the presence of an applied field orthogonal to the current (see Fig. 2.3), then the resultant Lorentz force is compensated by a volume pinning force F_V (or F_p):

$$\vec{F}_L = \vec{J} \times \vec{B} = -\vec{F}_V \quad (2.7)$$

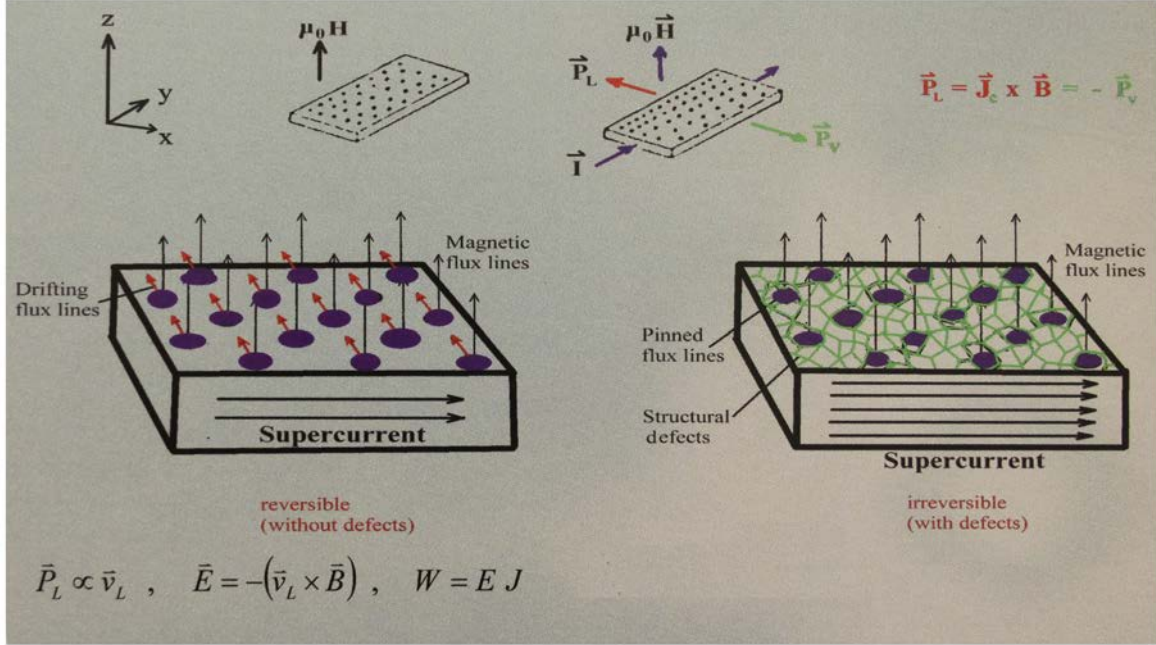


Figure 2.3: Graphic representation of a clean type-II superconductor (left) and one with pinning centers (right) [27]

This equilibrium is described as the critical state of a type-II superconductor by Bean [23] and London [24]. They suggested a single physical magnitude, namely the critical current density J_c which depends on the material and is used to calculate the magnetization in a superconductor. The Bean model, named after its creator, states that a constant critical current density, independent on the magnetic induction B , flows through a superconducting sample once the so-called Bean penetration field H^* has been reached. Fig. 2.4 illustrates a cross-section of a superconducting sample and the resulting magnetic profile inside the sample for an increasing applied field (left panel) and the current density distribution (right panel). The magnetic induction inside the superconductor shows a linear decrease from the outermost parts of the sample towards its innermost point. The magnetic flux penetrates into the center of the sample when H^* has been reached. A further increase in H_a merely shifts the magnetic profile upwards without changing J_c . In case of a reversal of the applied field by a total of $2 \cdot H^*$, the magnetic profile inside the superconductor is also completely reversed. The Bean model, coupled with the definition of the magnetic moment m , can be applied to calculate J_c for a known m :

$$\vec{m} = \frac{1}{2} \int \vec{r} \times \vec{J}(\vec{r}) dV \quad (2.8)$$

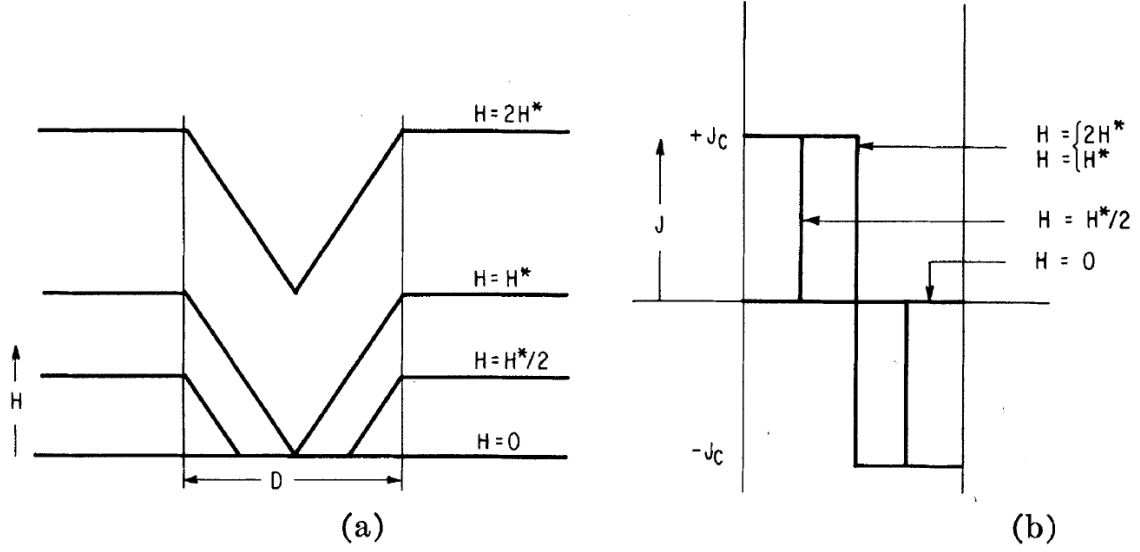


Figure 2.4: Bean model of the critical state (figure taken from the original publication [26])

where \vec{r} is the distance vector and V is the volume where the current flows through.

For a cuboidal sample with the sides a, b and c , volume $V = abc$, where the applied field H_a is parallel to c , the following equation [25] shows how to calculate J_c :

$$J_c = \frac{4|m_{irr}|}{Vb(1 - \frac{b}{3a})}, a \geq b \quad (2.9)$$

where $|m_{irr}|$ represents the magnitude of the irreversible magnetic moment resulting from the currents flowing within the sample. This well-known relation is valid when the currents flowing along a and b are isotropic ($J_c^a = J_c^b$). An extension of the model is necessary when considering cuboidal samples which do not display isotropic currents ($J_c^a \neq J_c^b$) [28]. Analytical solutions can be found for an $|m_{irr}|$ caused by a current distribution within the cuboidal sample described previously, with $J_c^a \neq J_c^b$ and $H_a \parallel c$:

$$J_c^a = \frac{4|m_{irr}|}{Vb(1 - \frac{b}{3a} \frac{J_c^a}{J_c^b})}, \frac{a}{b} \geq \frac{J_c^a}{J_c^b} \quad (2.10)$$

Equation 2.10 can be easily adjusted in case the condition $\frac{a}{b} \geq \frac{J_c^a}{J_c^b}$ is not fulfilled and one obtains:

$$J_c^b = \frac{4|m_{irr}|}{Va(1 - \frac{a}{3b} \frac{J_c^b}{J_c^a})}, \frac{a}{b} < \frac{J_c^a}{J_c^b} \quad (2.11)$$

The Bean model is a simple, yet very useful theoretical explanation of flux penetration into a type-II superconductor. It provides the backbone for the evaluation of J_c from magnetization measurements. The setups used for these experiments are discussed in detail in Sec. 4.1.2 and 4.1.3.

2.3 Transport critical current density

It is necessary to tackle the theoretical understanding of critical currents when a macroscopic transport current flows through the superconductor. In this case, the upper limit of J_c is the so called depairing current density J_d , provided from the Ginzburg-Landau theory:

$$J_d = \frac{\phi_0}{3\sqrt{3}\lambda^2\xi\mu_0} \quad (2.12)$$

This is the transport current density at which the Cooper pairs are broken and superconductivity is destroyed in the sample. However, this theoretical limit cannot be obtained in real materials. In reality, the pinning properties of the superconductor determine the practically achievable current densities. It is necessary to consider the interaction between vortex matter and a transport current flowing through the superconductor to explain this phenomenon

When no external field is present, the flux lines in the superconductor are created by the transport current-induced magnetic field. They cannot move as long as the available pinning force is sufficient to compensate the Lorentz force. This equilibrium holds if the current is not higher than a certain value at which F_L exceeds the pinning force. This limit is the definition of J_c in terms of transport current measurements. Once $J > J_c$, the flux lines start flowing through the superconductor and an electric field is caused. In reality, though, even if the applied current is relatively low ($J \ll J_c$) there is still another available mechanism for displacing a flux line: thermal activation [29]. This means that a flux line can be depinned due to the finite thermal energy and moves through the superconductor, preferably in the direction of the Lorentz force, causing a very small electric field E . This regime is known as ‘thermally assisted flux flow’. As the current increases, the flux lines start creeping under the influence of the increasing Lorentz force on them since the pinning force is no longer sufficient to hold them in place. The jumps against the Lorentz force are negligibly few. As a result, the flux lines start

to move in the direction of F_L , thus a finite voltage $U \propto E$ can be measured as the so called ‘flux creep’ regime settles in. However, superconductivity is still not destroyed at this point. In case the current becomes larger than J_c , the flux lines flow freely through the superconductor (‘flux flow regime’) until J_d is reached. At this point the sample is no longer superconducting. It is worth noting that it is not straight-forward to experimentally access the whole phase diagram $E(J)$ of the three individual regimes. The biggest problem stems from energy dissipation in the form of heat in the superconductor during the flux creep regime. This can cause a rapid change in temperature and bring it above T_c .

The evaluation of J_c from transport current measurements, which links theory with experiment, is presented in Sec. 4.2.1.

2.4 Anisotropy of the upper critical field

The previous two sections cover one of the main features of type-II superconductors, namely the critical current density. Another important facet of these materials is the upper critical field B_{c2} . The classical, low temperature ($T_c < 20$ K) type-II superconductors such as NbTi and NbSn₃ have B_{c2} s which are nearly independent on the orientation of their crystallographic structure to an applied magnetic field. Therefore these materials are known as ‘isotropic’ superconductors. However, there have been reports of materials with clear anisotropic behavior of B_{c2} as early as 1976 [30]. The discovery of the cuprates [31] gave new prominence to this phenomenon due to the strongly anisotropic B_{c2} of these materials. To understand the root for this strong anisotropy, it is necessary to examine the crystal structure of these materials. The cuprates, as well as the pnictides, are layered materials where superconductivity takes place in the Cu-O or Fe-As planes, also known as the ab -planes. The axis perpendicular to the latter is called the c -axis. These crystallographic differences lead to pronounced variations of the Fermi surface properties such as the Fermi velocities [32], depending of the orientation of the applied field. While there are many previous studies on this phenomenon, the feature of particular interest is the difference in the upper critical field in the main orientations: $H_a \parallel ab$ and $H_a \parallel c$. It is well known that the pnictides and cuprates have nearly isotropic properties in the ab planes, therefore the case $H_a \parallel c$ is rather straightforward and the respective $B_{c2} = B_{c2}^c$

can be calculated using Eq. 2.4:

$$B_{c2}^c(T) = \frac{\phi_0}{2\pi\mu_0\xi_{ab}^2(T)} \quad (2.13)$$

where ξ_{ab} is the coherence length within the ab -planes. When $H_a \parallel ab$, the currents confining the flux lines flow not only within the Fe-As planes, but also along the c -axis. In this configuration $B_{c2} = B_{c2}^{ab}$ and the mathematical equation is:

$$B_{c2}^{ab}(T) = \frac{\phi_0}{2\pi\mu_0\xi_c(T)\xi_{ab}(T)} \quad (2.14)$$

where ξ_c is the coherence length along the c -axis. Having written down the equations which define the upper critical fields in the main orientations, it is possible to define an anisotropy parameter γ . It is given by the following equation:

$$\gamma := \frac{B_{c2}^{ab}}{B_{c2}^c} = \frac{\xi_{ab}}{\xi_c} \quad (2.15)$$

This parameter has an important role when applying various scaling approaches to data from angle-resolved experiments.

Chapter 3

Samples

3.1 Single crystals

BaFe₂As₂-based superconducting single crystals with different dopants were researched in this thesis. The basic properties of this system are examined in the following paragraphs. The crystal structure of the parent compound at room temperature is shown in Fig. 3.2. It has a tetragonal structure at room temperature which undergoes a transition to orthorhombic at about 140 K [49]. BaFe₂As₂ has a *c*-axis of about 1.3 nm. Further details on the crystallography of the parent compound can be found elsewhere [49].

There are two ways of inducing superconductivity in BaFe₂As₂. The first method involves applying pressure (bottom panel of Fig. 3.1) [33, 34, 35, 36, 37], while the second one is based on doping (top panel of Fig. 3.1) [2, 3, 4, 5]. Either way, a phase transition from antiferromagnetism to superconductivity is observed at low temperatures (see Fig. 3.1).

Three different types of doping exist, depending on the doping site and valence of the dopant. Electron-doped materials include Ba(Fe_{1-x}Co_x)₂As₂ and Ba(Fe_{1-x}Ni_x)₂As₂ since Co and Ni have a higher valence than Fe. They have transition temperatures T_c of about 25 and 21 K respectively. Electrically neutral doping can also induce superconductivity in this material, for instance when As is replaced by P. Finally, the highest T_c is obtained when hole doping is performed, for example when Ba is substituted by K. This compound was first reported by Rotter et al., with a transition temperature close to 40 K. Additionally, an upper critical field B_{c2}^{ab} (0 K) of over 100 T has been surmised [6] for the K-doped system.

The single crystals which were analyzed in the course of this thesis comprised all three doping types. Multiple optimally doped Ba-122 single crystals with either Co, P or K doping were provided by the National Institute for Advanced Industrial Science and Technology (AIST), Tsukuba, Japan. The samples were synthesized via the self-flux method [44, 45, 46]. The nominal chemical compositions of the crystals are $\text{Ba}(\text{Fe}_{0.94}\text{Co}_{0.06})_2\text{As}_2$, $\text{BaFe}_2(\text{As}_{0.7}\text{P}_{0.3})_2$ and $\text{Ba}_{0.6}\text{K}_{0.4}\text{Fe}_2\text{As}_2$. An examination with an optical microscope showed that the crystals had very nice growth, nearly perfect cuboidal shape which is in good agreement with the compounds' tetragonal crystal structure at room temperature, indicating an excellent crystal growth. A typical crystal with the dimensions $2.31 \times 1.78 \times 0.184 \text{ mm}^3$ is shown in Fig. 3.3. The shiny black surface is almost as smooth as glass. This is another indication for a good crystal growth. The lateral dimensions of the crystals were determined with an optical microscope. Next, the density of each material is calculated by using the known elementary cell dimensions and nominal doping levels. The mass of each crystal is measured with a micro-gram scale, therefore it is easy to calculate the total volume. Since the lateral dimensions are known already, it is straightforward to calculate an average thickness for each single crystal. This parameter did not show big variations (resolution of an optical microscope) due to the excellent crystal growth. The absolute precision of the geometric dimensions is about 1-2 μm .

In total, there were 16 available high-quality crystals. Table 3.1 shows the ones which took on a more prominent role in this work, introducing the nomenclature which will be used throughout it as well. The name of the individual crystal contains the dopant. V denotes the volume of the crystal, a , b and c are the sides. A detailed crystallographic study on the Ba-122 family can be found elsewhere [49].

As an example for the good quality of the crystals, Fig. 3.4 shows the remanent Bean profile in a K-doped single crystal at 10 K, obtained by micro Hall mapping.

3.2 Thin films

Besides single crystals, a single crystalline Co-doped Ba-122 thin film, provided by IFW Dresden, was studied. A photograph of the film can be seen in Fig. 3.5(a). The lateral

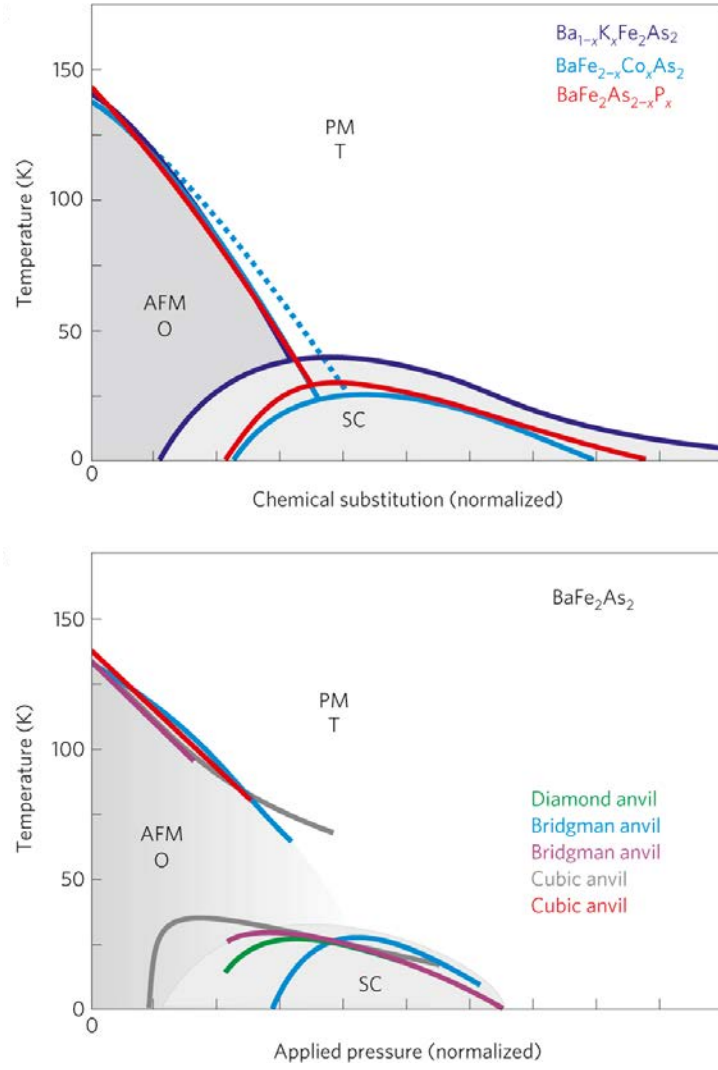


Figure 3.1: Phase diagram of the Ba-122 system (from [38]). The top panel shows the emergence of superconductivity with doping, while the bottom panel reveals the effect of applied external pressure on the parent $BaFe_2As_2$ compound.

| Sample | V (mm^3) | a (mm) | b (mm) | c (mm) |
|------------------|----------------|----------|----------|----------|
| Co#1 | 0.153 | 2.38 | 0.836 | 0.077 |
| Co#3 | 0.34 | 2.018 | 0.914 | 0.182 |
| Co#4 | 0.76 | 2.31 | 1.78 | 0.184 |
| P#1 | 0.50 | 2.54 | 2.25 | 0.088 |
| P#2 | 0.164 | 2.61 | 0.67 | 0.094 |
| K#4 | 0.06 | 1.7 | 0.568 | 0.06 |
| K#5 | 0.36 | 1.85 | 1.5 | 0.129 |
| K#5 ₁ | 0.016 | 0.88 | 0.46 | 0.04 |

Table 3.1: Nomenclature of the single crystals examined within the thesis

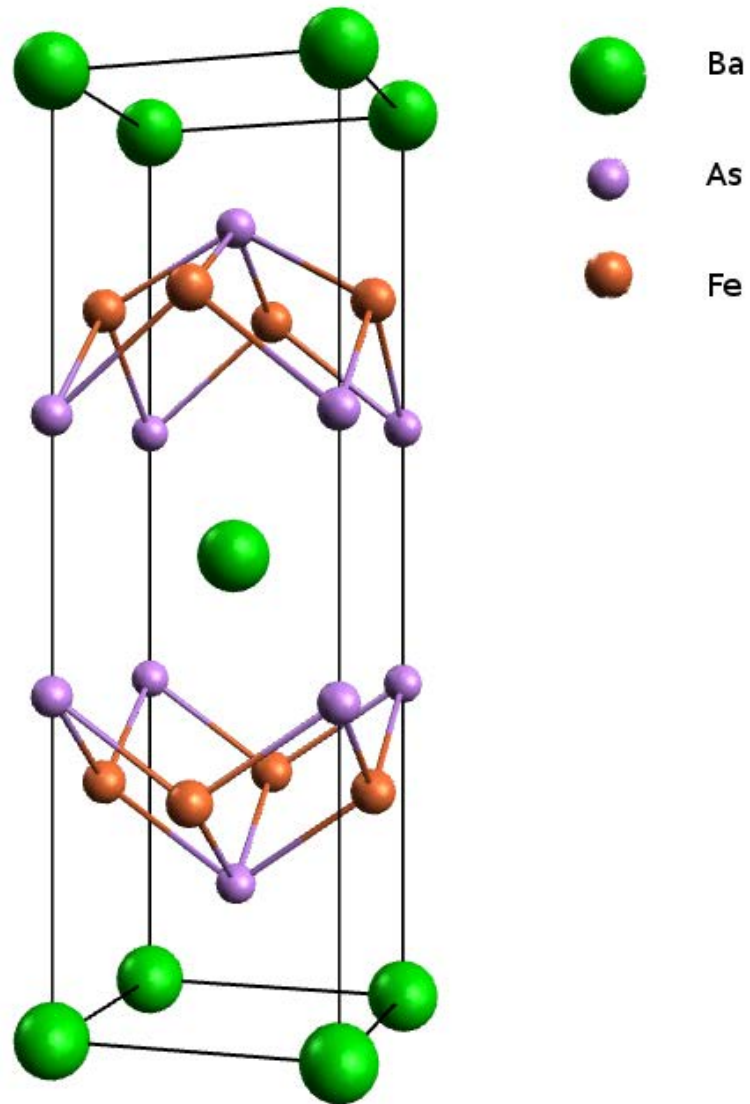


Figure 3.2: Crystallography of the Ba-122 parent compound

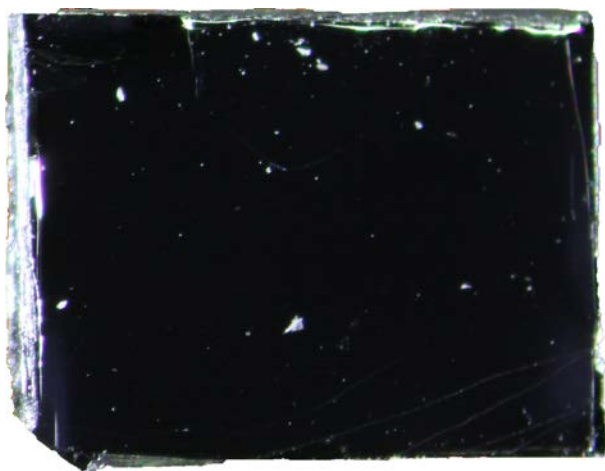


Figure 3.3: An enlarged image of the Co-doped Ba-122 single crystal Co#4 (dimensions available in Tab. 3.1)

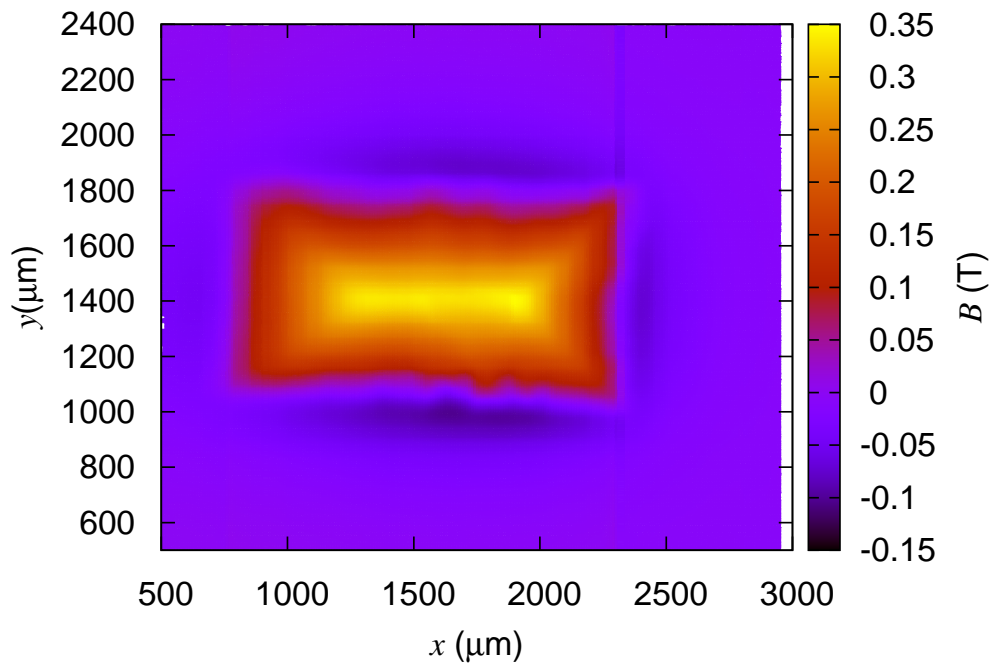


Figure 3.4: Hall scan of the remanent magnetic profile in a pristine K-doped single crystal at $T = 10$ K

dimensions of the superconducting bridge (blackish hue) are $0.585 \times 0.877 \text{ mm}^2$. The length of the substrate is 10 mm. The film's nominal composition is $\text{Ba}(\text{Fe}_{0.9}\text{Co}_{0.1})_2\text{As}_2$. Pulsed Laser Deposition (PLD) was used to deposit a buffer Fe-layer with a thickness of 15 nm onto a MgO substrate. The superconducting film is subsequently deposited via PLD onto the Fe-layer and has a thickness of about 80 nm [50]. A thin (several nanometers) Au-Pt layer protects the superconductor, in particular against excessive humidity.

Transition electron microscopy studies performed on a separate film which had been prepared under the same conditions revealed the presence of planar defects along the ab -planes (Fig. 3.5(b)). Their role with respect to flux pinning is elaborated in Sec. 5.1.

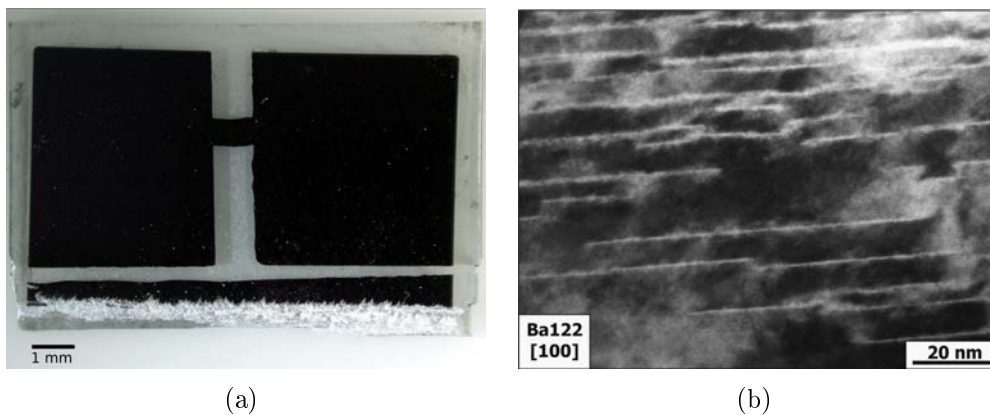


Figure 3.5: (a) An optical image of the Co-doped Ba-122 thin film; (b) A TEM picture (performed by E Reich, IFW Dresden) taken parallel to the a -axis which reveals planar defects aligned with the Fe-As planes of the film

Chapter 4

Experiment

4.1 Magnetometry

4.1.1 Susceptibility measurements in a 1 T SQUID

AC susceptibility measurements in a 1 T SQUID are suitable for determining the transition temperature of the available single crystals. A magnetic field amplitude of 0.1 mT was used for the measurements. Unless otherwise stated, the sample is mounted with its c -axis parallel to the applied field. The starting temperature is several Kelvin lower than the expected T_c for the respective compound. The temperature is ramped upwards in predefined steps. A very good temperature stability is needed for precise T_c measurements. To that end, the measurement sequence pauses for five minutes after the temperature has been stabilized to the desired value. Subsequently, the AC susceptibility is measured and the sequence continues with the next temperature step.

Different criteria can be used for the evaluation of T_c . These include the onset of superconductivity T_c^{onset} , mid-point T_c^{mid} and inflection tangent T_c^{tan} criteria. Also, the transition width can be determined from $T^{10\%} - T^{90\%} = \Delta T_c$, where $T^{10\%}$ and $T^{90\%}$ are the respective temperatures at 10% and 90% of the maximum response signal. A broader transition indicates stronger inhomogeneity in a superconductor. Fig. 4.1 illustrates a real measurement evaluated in accordance to the individual criteria. In this particular measurement, T_c^{onset} is nearly identical to T_c^{tan} , that is why only T_c^{tan} is labeled in the figure. A combination of T_c^{onset} and ΔT_c is used in this thesis when evaluating the AC susceptibility measurements. In the following sections $T_c = T_c^{\text{onset}}$.

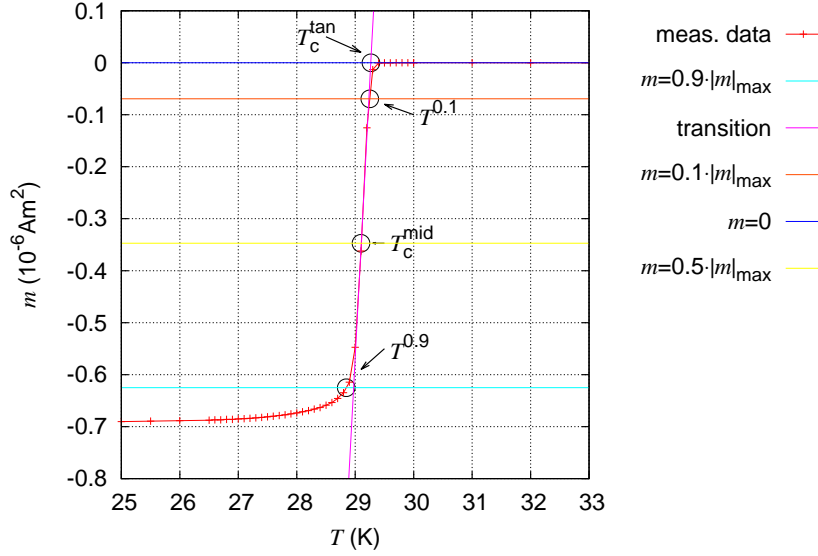


Figure 4.1: An example for the evaluation of the AC susceptibility measurement on a single crystal

The 1 T SQUID is also suitable for establishing the so called shielding fraction v_{sh} of a superconductor. This parameter describes the quotient $\frac{V_s}{V}$ of the volume V_s shielded by the Meissner currents and the physical volume V of the superconductor. For an ideal single crystal, it is expected that $v_{\text{sh}} = 100\% = 1$. In reality, the shielding fraction is rarely 100% due to surface degradation/inhomogeneities which lead to a reduction in v_{sh} . Nevertheless, this is a good test to establish whether a crystal is of sufficiently high quality. In this work, all crystals show $v_{\text{sh}} > 90\%$ and most of them eclipse 95%. It is important to keep in mind that v_{sh} shows only the shielded volume, which means the actual superconducting volume is not accessible by this measurement. The usual procedure to determine v_{sh} involves a measurement of the Meissner slope. The amplitude of the AC field is ramped step-wise (0.01 mT steps), typically from 0.01 to 0.2 mT. In the Meissner phase, the applied field is shielded from the inner of the superconductor (lambda notwithstanding) (see Sec. 2.1):

$$\vec{B} = \mu_0(\vec{H}_a + \vec{M} + \vec{H}_s) = 0 \quad (4.1)$$

where \vec{H}_s is the stray field. It can be estimated if D which depends on the geometry of the crystal and its orientation to the external applied field is known. The magnetization can be expressed via the measured magnetic moment and returns $M = \frac{m}{V_s}$. The equation

can be rewritten to:

$$V_s = \frac{m(1 - D)}{H} \quad (4.2)$$

Having calculated V_s , it is easy to use the already known physical volume and calculate v_{sh} . The experiment is typically performed for the smallest possible D , therefore the crystal is mounted in the configuration $H_a \parallel ab$. For the available crystals, the resulting demagnetization factor is about 0.1 in this orientation.

4.1.2 Magnetization loops in a 7 T SQUID

Additionally, a 7 T SQUID is available for establishing J_c in the main orientations ($H_a \parallel ab, c$) from magnetization loops. The latter are a standard technique for determining J_c in superconducting single crystals. Magnetometry is usually the only way to access this quantity in bulk samples due to the large macroscopic currents necessary to reach J_c (exception: crystals structured via Focused Ion Beam (FIB) [52] where transport current measurements are also possible). The main advantages of the 7 T SQUID are the high applied field and its high measurement precision. The Reciprocating Sample Option (RSO) of the 7 T SQUID returns m with an absolute precision of about 10^{-10} Am². The maximum external field of 7 T allows the evaluation of magnetization measurements on crystals with large Bean penetration field B^* of up to a few Tesla. However, the 7 T SQUID has some limitations when it comes to measuring very high magnetic moments. For instance, the RSO cannot record magnetic moments above $1.25 \cdot 10^{-3}$ Am². This nuisance is solved with help of standard DC (Direct Current) measurements which allow precise measurement of moments up to about 10^{-2} Am² [53].

The standard procedure when measuring magnetization loops starts with cooling down the sample at zero field to the desired temperature. After that, a negative field larger than $2 \cdot H^*$ is applied to the crystal. Subsequently, the field is set back to zero. As a result, the crystal is fully magnetized (see Sec. 2.2). The applied field is now at 0. Next, H_a is incremented step-wise and the magnetic moment is measured at each field until the maximum applied field, typically 7 T, is reached. This segment of the loop will be referred to as the increasing field branch or m_+ . After this, the field is reduced to zero, measuring m at the the same field steps as in m_+ . A sample of loops at different temperatures is presented in Fig. 4.2. The region immediately after the reversal of the

field direction shows how the inversion of the magnetic profile in the superconductor affects the magnetic moment (see Sec. 2.2). The profile is fully reversed after the external field is changed by $2 \cdot H^*$. The region between the maximum of the applied field H_a^{\max} and $H_a^{\max} - 2 \cdot H^*$ cannot be used for the evaluation of J_c since the current does not flow uniformly in the crystal at this stage.

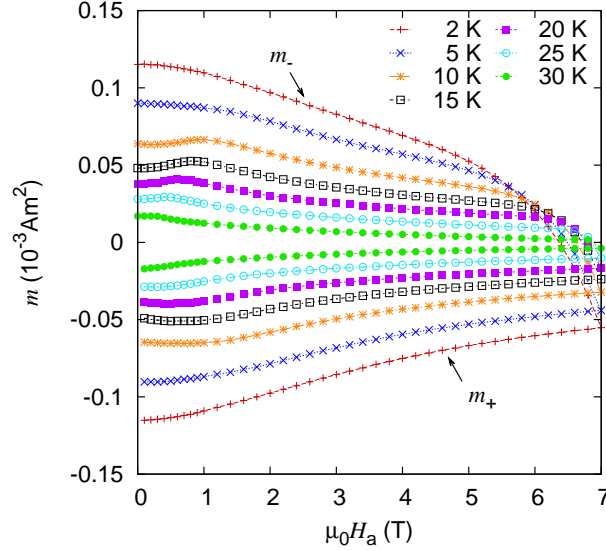


Figure 4.2: Magnetization loops at different temperatures after zero-field cooling

In case of a very large penetration field (above 3 T), it is advantageous to perform field cooling at -7 T from a temperature above T_c . After the desired measurement temperature has been reached, the field is then increased step-wise to 7 T and the magnetic moment is recorded at each step. This method is useful since only $1 \cdot B^*$ is needed to fully magnetize the whole crystal instead of $2 \cdot B^*$. As an example, a field-cooled measurement on a Ba-122 single crystal with particularly high signal is shown in Fig. 4.3. When comparing Fig. 4.2 and Fig. 4.3, it becomes apparent that m_+ is located in the fourth quadrant in both cases, while m_- is in the first or third quadrant respectively. Please note that the magnetic moment is steadily negative in magnetization loops performed according to the described field cooling procedure, therefore m_- has a negative value, but the direction of the self-field is still parallel to the applied field.

The strong drops in magnetization at certain fields which are visible in Fig. 4.3 result from so called flux jumps [41, 42]. This phenomenon is typically observed in larger samples with very high currents. The change in B causes a change in the force exerted on the flux lines, which can occasionally result in a spontaneous depinning of flux lines which

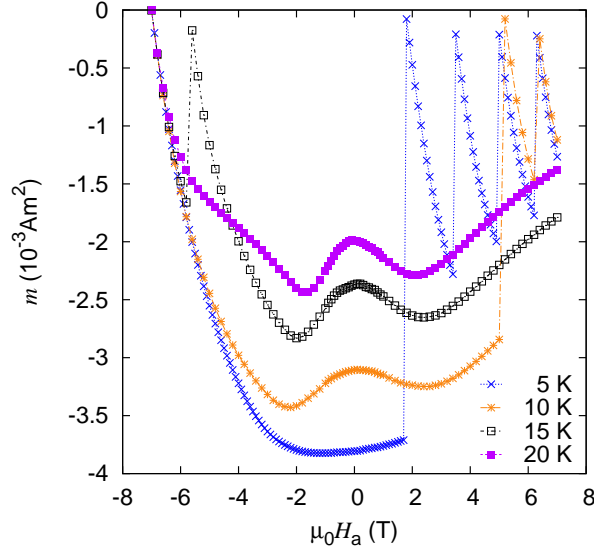


Figure 4.3: Magnetization loops at different temperatures after field-cooling at 7 T

in turn causes an avalanche-like reaction and the entire superconductor is permeated by magnetic flux. A careful look at the measured magnetic moment shows a non-zero signal after each individual flux jump, albeit sometimes very small. This is in contrast to the zero signal measured immediately after the field-cooling to the desired temperature. Since the re-magnetization of the sample has already started in between the two field steps, the flux jump can only have taken place in-between steps as well. One way to try and prevent flux jumps is to use a smaller field ramp rate and a smaller step size when performing the magnetization measurements, while reducing the volume of the crystal can also be useful.

Both of the aforementioned measurement modes allow a simple, direct calculation of $m_{\text{irr}}(H_a)$ using the two segments of the curve $m_+(H_a)$ and $m_-(H_a)$. This leads however to the dependence of the irreversible magnetic moment on the external applied field H_a , while ideally one would like to calculate a dependence on the magnetic induction B :

$$\vec{B} = \mu_0(\vec{H}_a + \vec{M} + \vec{H}_{\text{sf}}) \quad (4.3)$$

where H_{sf} is the self-field of the superconductor. H_{sf} is caused by the critical currents flowing through the crystal and its influence on B is particularly strong when both J_c and V are large. The evaluation of H_{sf} is based on the Biot-Savart law and can be performed automatically using a computer program [43].

4.1.3 Angle resolved magnetization loops in a vector Vibrating Sample Magnetometer

Another device for magnetization measurements is the vector Vibrating Sample Magnetometer (VSM) [39]. The main advantage of this device is that both components of the magnetic moment (parallel and orthogonal to the applied field H_a) are recorded by two sets of Malinson coils [40]. The sample periodically oscillates within the coil system with an amplitude and frequency which are set prior to the measurement. The temperature of the cryostat can be varied down to 2.2 K, while the superconducting magnet can reach fields of up to 5 T and is oriented transversally to the sample rod's symmetry axis.

The VSM can measure magnetic moments up to about $2 \cdot 10^{-3} \text{ Am}^2$ at an amplitude of 1.5 mm. Since the VSM measures an induced voltage via the Malinson coils which is then converted into magnetic moment, it is possible to measure even higher moments if the amplitude is reduced, because the induced voltage is proportional to the amplitude of the oscillation. The noise level in the VSM is about 10^{-7} Am^2 , distinctively higher than in the 7 T SQUID, but this is usually not significant since most crystals have a large volume of about 0.5 mm^3 and high critical currents, resulting in typical magnetic moments exceeding $1 \cdot 10^{-4} \text{ Am}^2$.

The VSM can be used for magnetization measurements (loops) similar to the 7 T SQUID (see Sec. 4.1.2). One notable difference (besides the lower available applied field) is the fact that the external field in the VSM is not set step-wise, but is rather swept at a fixed rate (0.15 T/h) and the two magnetic moments are recorded during the field sweep. T typically deviates by about $\pm 0.02 \text{ K}$ during the measurement. Such fluctuations are negligible for most of the temperature range. They become significant only at temperatures close to T_c .

The VSM is equipped with two stepper motors. The first one is used for the vertical alignment of the sample. The aim is to position it precisely between the two Malinson coil sets. The second one rotates the sample rod, making it possible to measure the dependence of m on the angle ϑ between the applied field and the c -axis of the single crystals. Prior to the start of a $m(\vartheta, T, B)$ measurement, it is necessary to establish the starting position of the VSM rotating motor. This objective can be fulfilled by completing magnetization loops at different ϑ and searching for the position where the parallel component of the magnetic moment reaches its minimum while the orthogonal

component disappears entirely. This occurs when the crystal is in the orientation $H_a \parallel ab$ according to the definition of the magnetic moment (see Eq. 2.8). As a result, the position $\vartheta = 90^\circ$ has been determined. Care has to be taken during the procedure that the crystal is always uniformly magnetized, therefore it is advantageous to position the crystal at higher temperatures $t \approx 0.8 - 0.9$.

With help of the vector VSM, it is possible to evaluate the anisotropy of the critical current density in a single crystal via magnetization measurements [54]. The supercurrents were found to flow parallel to the ab -planes up to $\vartheta = 75^\circ$ because of the high aspect ratio of the crystal geometry (typically $a \geq 2b \geq 10c$). When $\vartheta \neq 0^\circ$, currents (J_c) flowing under maximum Lorentz force (perpendicular to H_a) and currents flowing under variable Lorentz force (J_c^{VLF}) have to be distinguished. Both current densities were evaluated by applying the anisotropic Bean model (see Sec. 2.2) to the data of two subsequent measurements. During the first measurement, the sample was mounted with the rotation axis r of the VSM parallel to a . This means that J_c flows parallel to a and J_c^{VLF} - to b , respectively. According to Eq. 2.10 and 2.11 the irreversible magnetic moment m_{irr} is given by:

$$|m_{\text{irr}}|(r \parallel a) = \frac{J_c V b (1 - \frac{b}{3a} \frac{J_c}{J_c^{\text{VLF}}})}{4}, \frac{a}{b} \geq \frac{J_c}{J_c^{\text{VLF}}} \quad (4.4)$$

In the case $\frac{a}{b} < \frac{J_c}{J_c^{\text{VLF}}}$, the expression changes to:

$$|m_{\text{irr}}|(r \parallel a) = \frac{J_c^{\text{VLF}} V a (1 - \frac{a}{3b} \frac{J_c^{\text{VLF}}}{J_c})}{4}, \frac{a}{b} < \frac{J_c}{J_c^{\text{VLF}}} \quad (4.5)$$

The sample was then remounted with r parallel to b . In this configuration, a and b have to be exchanged in the above expressions. J_c and J_c^{VLF} can be extracted from the two measurements and these equations.

J_c and J_c^{VLF} are typically not equal. The reduced Lorentz forces usually result in higher currents. This difference can cause an interesting feature, namely two individual H^* . The penetration field is dependent on the current density, the geometry of the single crystal and its orientation in the external field. Fig. 4.4 shows two separate measurements, with r parallel to either a or b , at the same angle $\vartheta = 75^\circ$. The difference in the magnitude of the magnetic moment components from one figure to the other is easily explained. The stronger current J_c^{VLF} flows along $a > b$ in the configuration illustrated in Fig. 4.4(b) which causes the larger signal.

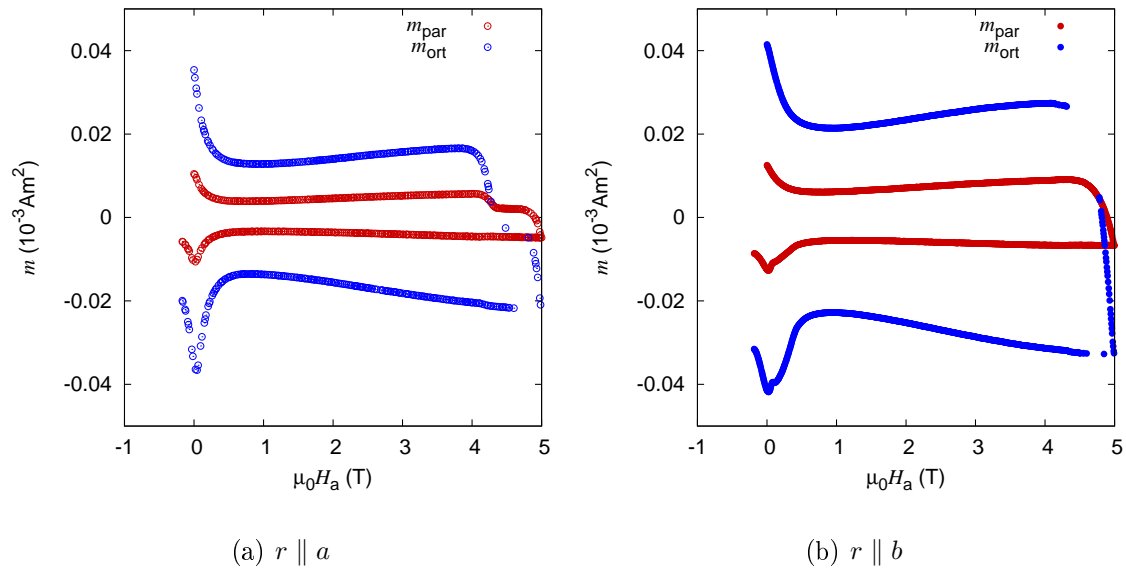


Figure 4.4: Sample curves from the VSM with r parallel to either a (left panel) or b (right panel) for $\angle(H_a, c) = 75^\circ$

A comparison of the respective regions immediately after the reversal of the field (H_a between 5 and 4.5 T) shows that two individual ‘ H^* ’s are clearly visible in the left panel, while the feature is indistinguishable in the right panel. In Fig. 4.4(a), $J_c^{VLF} > J_c$ flows along b and in Fig. 4.4(b) - along a . Even though the problem of the anisotropic Bean model and in particular the resulting current profiles have already been studied extensively [55], this is an unexplained feature and presents an interesting topic for further research. It does not represent a problem for the evaluation of the critical current density from the magnetization loops.

The VSM measurements are evaluated in a similar manner to the ones performed in the 7 T SQUID. The only major difference in the evaluation is the fact that H_{sf} is no longer necessarily parallel or anti-parallel to H_a , depending on ϑ . An extension of the available evaluation software takes this into account and allows the extraction of $J_c(B, \vartheta)$. It is worth noting at this point that the variable direction of the self-field means that the angle ϑ does not coincide with the angle $B \angle c$ -axis at all applied fields. In particular for crystals with strong self-fields, the difference is quite large (several tens of degrees) at high ϑ . This has to be considered when plotting evaluated data from angle-resolved measurements.

In case the irreversible magnetic moment is not large (small sample size, low currents), the background signal becomes relevant and has to be accounted for during the evalua-

tion. The first factor which has to be considered are unwanted vibrations of the system, particularly the coils. They can completely distort the measured signal. Therefore great care is taken to ensure that no incident collisions with the cryostat take place during the measurement. Additionally, the upper part of the system which includes the vibrator is connected to the cryostat with a special brass piece which dampens the vibrations and does not transfer them onto the coil system. Background signal can also be caused by the crystal itself, the sample holder and rod, as well as by the teflon tape and silicon strip holding the sample in place during the measurement. All materials involved in the sample placement have very low susceptibilities ($\chi \approx 0$) and do not cause a large signal. The crystals are of high quality and show almost no reversible background signal in measurements above T_c which indicates the absence of excess iron (a common occurrence in low quality iron-based superconducting single crystals). Most of the measurements carried out on the available Ba-122 samples showed irreversible moments above 10^{-4}Am^2 , while a typical background signal amounts to several 10^{-6}Am^2 , therefore the latter is negligible. In the few cases when the background was in the order of magnitude of m_{irr} , it was estimated via a hyperbolic tangent fit through the measurement data and accounted for during the evaluation procedure.

4.2 Transport current measurements

4.2.1 6 T system

Transport current measurements in the 6 T setup are used to establish J_c and T_c in the thin film. When measuring the transition temperature, a small current should be selected to protect the film on one hand and to prevent excessive heating which would falsify the results, on the other hand. The measurement was therefore performed with a transport current $I = 1 \mu\text{A}$. The temperature as measured by a Cernox sensor positioned close to the film decreases from 35 to 15 K with a ramp of 12 K per hour. The voltage drop across the bridge in the film is measured by a standard four-probe method. The electric contacts were made via pogo pins, with small indium pads inserted between the surface of the film and the pin to protect the sample from mechanical damage and to improve conductivity. Two current and two voltage leads are thus placed on the surface of the film, which is the basis for the four-probe measurement technique. The leads are intertwined pair-wise

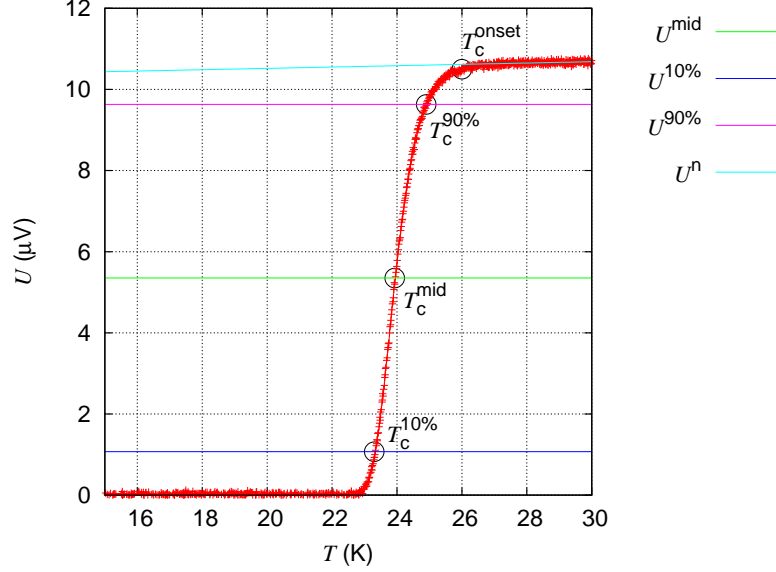


Figure 4.5: Evaluation of T_c of a Co-doped BaFe_2As_2 from a resistive measurement

in order to prevent induction voltages caused by the ramping or change in polarity of the current. The physical parameter which varies with temperature is the resistivity ρ . The change in the measured voltage is proportional to the change in the resistivity. The recorded $U(T)$ curves can therefore be used for the evaluation of T_c .

There are multiple available criteria for the evaluation of T_c , similar to the ones described in Sec. 4.1.1. They include the onset of superconductivity, mid-point, tangent criterion, zero resistivity and so on. In this case a sample evaluation is shown in Fig. 4.5, where T_c^{onset} and T_c^{mid} are self-explanatory and the transition width ΔT_c is also calculated from the difference between $U^{90\%} - U^{10\%}$.

The setup includes a 6 T split-coil magnet in a gas flow helium cryostat. Three current sources are available, ranging from 5 nA to 150 A. The currents are limited to below 1 A in case of the available thin film due to the combination of a small cross-section ($\approx 0.08 \times 500 \mu\text{m}^2$) and the expected J_c of about $1 \cdot 10^{10} \text{ Am}^{-2}$.

A two-axes goniometer is used for measuring the critical current density as well as the transition temperature [56]. It has two rotation axes which are orthogonal to each other (see Fig. 4.7, the two rotation angles are called φ and θ), allowing multiple measurement configurations. The maximum current which can be transported through this sample rod is 5 A, therefore it suits the requirements of the particular film. Fig. 4.8(a) shows the standard out-of-plane configuration where the transport current I is orthogonal to H_a at

all positions and only the orientation of H_a to the c -axis changes. Fig. 4.8(b) displays a so-called variable Lorentz force (VLF) measurement where H_a changes its orientation with respect to both the c -axis of the film and also to I . The latter results in a non-constant magnitude of the resulting Lorentz force, thus the name variable Lorentz force measurements. A special case of the VLF configuration occurs when $\theta = 90^\circ$. In this position, only the magnitude of F_L changes with φ since H_a is parallel to the ab -planes for all angles φ . This configuration represents a so-called in-plane scan (Fig. 4.8(c)).

The measurements include recording $I - V$ curves at different temperatures, applied fields and sample orientations. A Hall sensor mounted on the sample rod allows monitoring the rotation along the φ axis. Tracking the precise position of the film when it is rotated along the θ -axis represents a bigger challenge due to the lack of a hall probe on the sample stage. It is therefore necessary to establish the starting position θ prior to inserting the sample rod in the cryostat. An optical alignment of the sample stage with a precision of about 1° is possible. The stage is rotated by a stepper motor which exhibits good reproducibility (in the range of a few hundredths of a degree) of the rotation, allowing multiple measurement cycles without removing the rod from the cryostat.

The evaluation of J_c from the $I - V$ curves is based on a power-law fit through the acquired data. The fitted function has the following form:

$$U = U_c \left(\frac{I}{I_c} \right)^n + U_{\text{offset}}, \quad (4.6)$$

where $U_c = 0.08\mu\text{V}$ is the voltage criterion calculated by multiplying the electric field criterion $E_{\text{cr}} = 1 \frac{\mu\text{V}}{\text{cm}}$ with the distance between the voltage leads (about 0.8 mm), I_c is the critical current $= J_c A$ (A is the cross-section of the superconductor) and n is the so-called n -value of the power law fit. The parameter U_{offset} describes a constant offset voltage caused by the temperature gradient between the voltage leads and their different chemical potential. Fig. 4.6 shows an evaluated $I - V$ curve where $I_c \approx 29.7 \text{ mA}$, $n \approx 18$, $U_{\text{offset}} \approx 0.33 \mu\text{V}$. Due to the large amount of data recorded during the measurements, an automatized procedure is necessary to evaluate all data sets in a reasonable time frame. To this end, a Python script was created which used the fitting functionality of the graphical plotting interface Gnuplot [57]. The user has to provide the correct U_c as well as an estimated value of I_c and n to begin the evaluation procedure. A maximum of 1000 iteration steps are allowed per fit in order to avoid infinite loops which could occur,

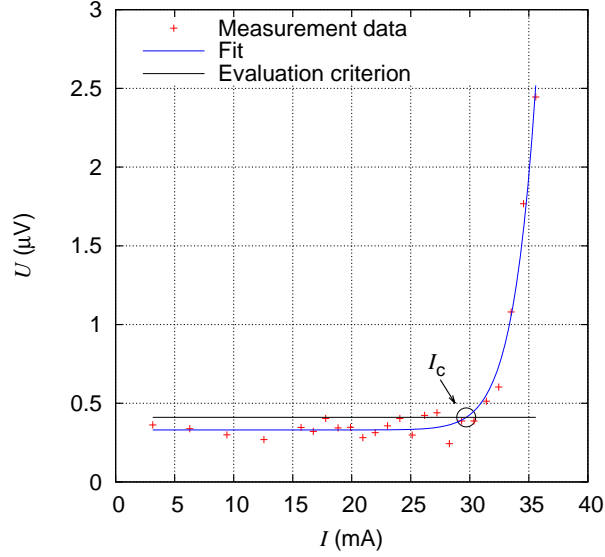


Figure 4.6: I_c evaluation via power-law fit

for instance, if the superconductor quenches during the measurement. The quality of the power-law fit is dependent on the whole curve and not only on the transition region. Due to the low currents necessary (below 1 A), there is no significant rise in temperature caused by contact resistance between the current leads and the superconductor or by heating of the current leads themselves. Warming up the sample could result in a baseline voltage signal prior to the transition, which in turn eschews the values obtained for I_c and particularly n . In such a case it is possible to use a log-log representation of the data and place a fit only through the transition region. The has a linear form and its crossing point with U_c returns I_c , while its slope represents the n -value. Since the film examined during the course of this thesis showed beautiful $I - V$ curves without notable baselines, it was possible to apply the power-law fit without causing a significant error in I_c or n . This choice was made since the parameter of interest, J_c , varies only slightly depending on the evaluation method. Additionally, a previous version of the evaluation software based on the power-law fit was already available, therefore it was considerably less time-consuming to adapt it than to create a new routine which uses a fit in a log-log representation.

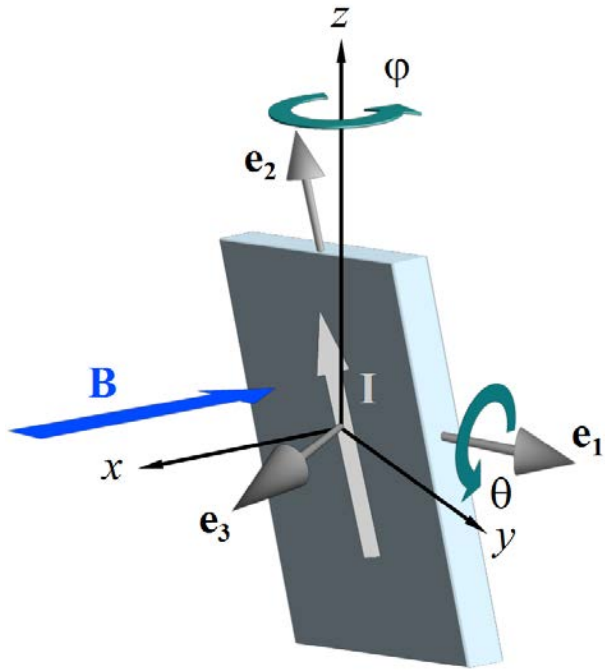


Figure 4.7: Rotation axes in the two-axes goniometer

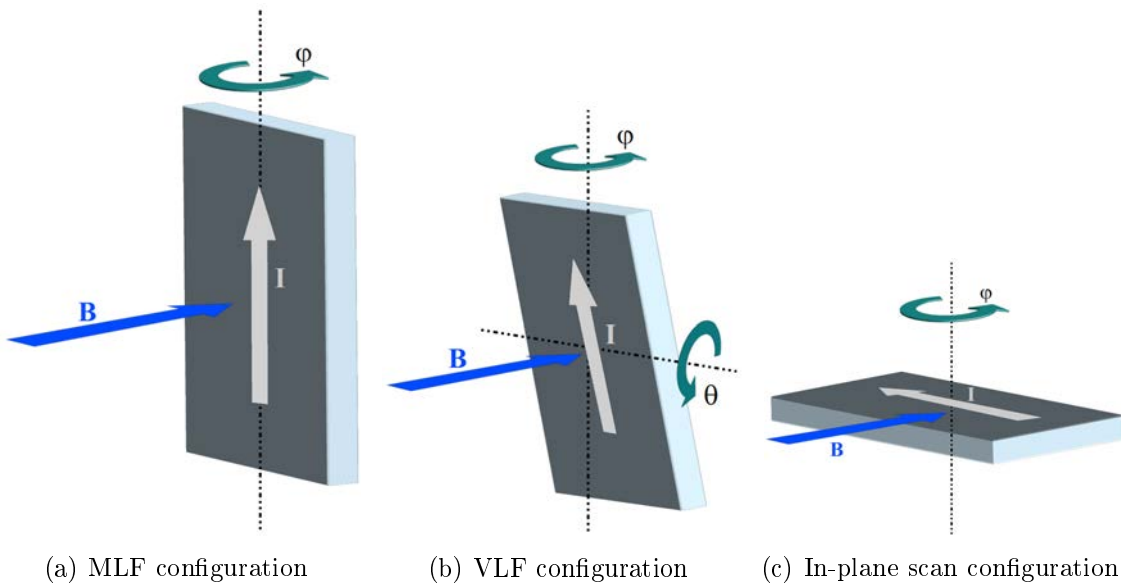


Figure 4.8: Different configurations for the two-axes goniometer measurements

4.2.2 17 T system

The main drawback of the 6T setup introduced in the previous subsection is its limited maximum applied field. In particular the high B_{c2} of Ba-122 based single crystals necessitate the availability of huge applied fields in order to measure B_{c2} from T_c all the way to almost 0 K. Although there was no access to such extreme magnetic fields, a 17 T setup is present and can be used for measuring B_{c2} , even if the temperature range is limited. The limitations are dependent on the maximum upper critical fields of the individual crystals.

The measurement system has a hybrid NbTi-Nb₃Sn magnet which can reach fields of above 17 T, whereby the field range between 15 and 17 T is accessible only if the helium bath in which the magnet is immersed is undercooled to about 2 K. As a result, the maximum applied field for the B_{c2} measurements is 15 T. Resistivity measurements at different fields are performed to obtain the respective transitions to the superconducting state. The experiments are based on a standard four-probe configuration. Due to the relatively small size of the crystals (typical lateral dimensions of $2 \times 2 \text{ mm}^2$), it was necessary to create an adapter which could be used for placing the electrical contacts on the sample without causing mechanical damage or structural decomposition to it. Ideally, one would require good electrical contacts with minimal pressure exerted on the crystal's surface and no usage of chemical solvents. Therefore, indium press contacts are a good option since they provide both protection for the sample and excellent electrical conductivity due to indium's high ductility at temperatures in the range of a few K. The adapter is shown in Fig. 4.10. The single crystal mounted on it is P#2, its geometry is given in Tab. 3.1.

The measurements were carried out at 15 T, 12 T, 10 T, 8 T, 6 T, 4 T, 2 T, 1 T, 0.5 T, 0.25 T and 0 T. The field of the superconducting magnet is parallel to the sample rod used for the experiment. It is necessary to perform two separate measurement cycles to obtain the resistive transitions for both $H_a \parallel ab$ and $H_a \parallel c$. The temperature is ramped very slowly (10 K per hour) so that the crystal has basically the same temperature as the Cernox sensor placed right next to it. The transport currents which are used for the resistive measurements are in the range of 1-5 mA, therefore small enough to prevent heating up the crystal.

The evaluation of the respective upper critical fields is based on a resistivity criterion.

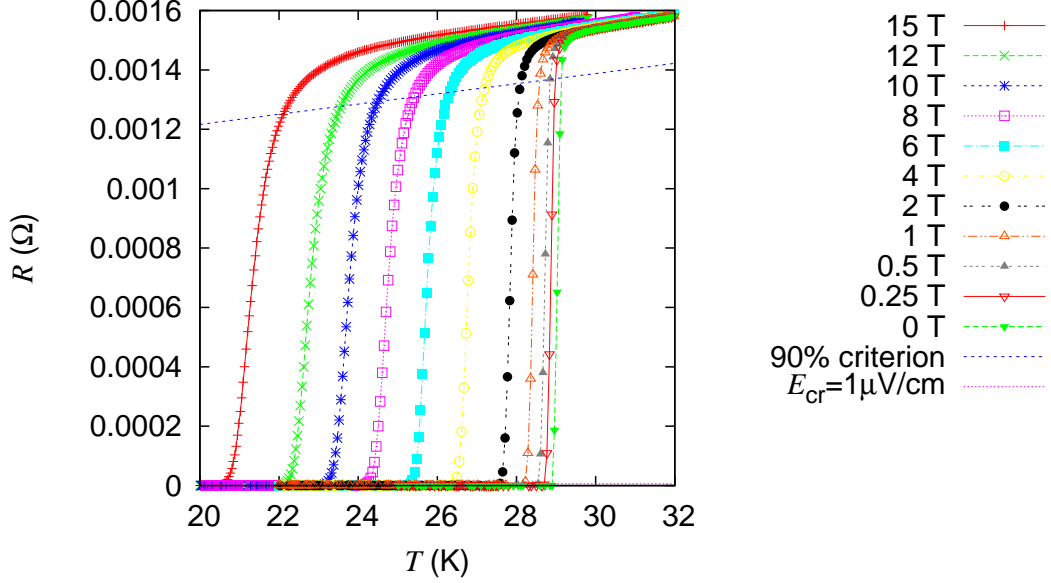


Figure 4.9: Sample resistive transitions and the evaluation criteria used to obtain B_{c2} and B_{irr} in the particular orientation

Typical values are 90% and 10% of the resistivity a few Kelvin prior to the onset of superconductivity. The 90% criterion was used in this study. A further parameter can be evaluated from the same transitions, namely the irreversibility line B_{irr} . Since these experiments involve transport current through a superconducting single crystal which undergoes a transition to the superconducting phase, it is possible to use the same criterion E_{cr} as in Sec. 4.2.1 and obtain the field and temperature at which the crystal can carry only a negligibly small critical current density, i. e. $J_c \approx 0$. This is an important parameter since, in contrast to classical low-temperature superconductors, the irreversibility line and the upper critical field can have distinctively different values. A sample evaluation of the two magnitudes from a set of resistive transitions is shown in Fig. 4.9.

4.3 Fast neutron irradiation

The fast neutron (E_n) irradiation is performed in a TRIGA Mark-II reactor situated in the Atominstitut, Vienna University of Technology. This is a well-established technique for the creation of an uncorrelated defect structure in a superconductor and multiple studies have been carried out on different superconducting materials (cuprates [58, 59, 60, 61], Nb_3Sn [62, 63], MgB_2 [64, 65], $Bi_2Sr_2Ca_{n-1}Cu_nO_{2n+4+x}$ [66], pnictides [10, 67, 68]). It is

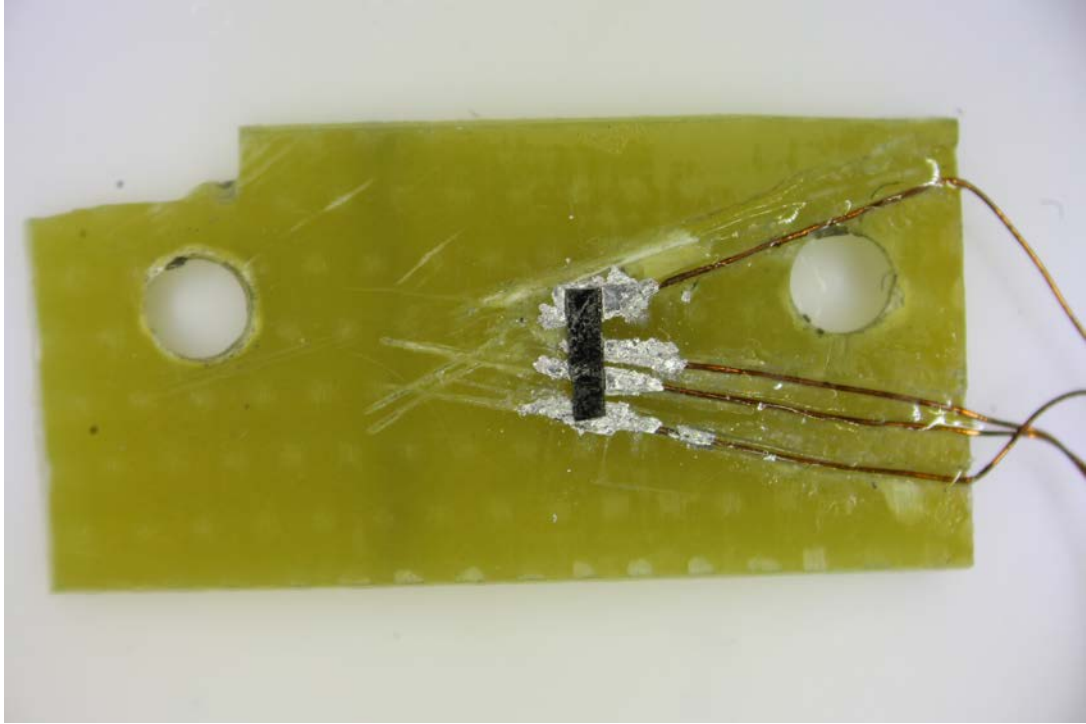


Figure 4.10: Connection adapter used for resistive measurements in the 17 T setup

not possible to experimentally establish the exact size, number and position of the created defects since the samples are radioactive after the irradiation which makes a TEM (Transmission electron microscope) study extremely difficult and time-consuming. The small number of successfully performed TEM studies on fast neutron irradiated superconductors suggest that the defects have radii of up to several nanometers in cuprates and MgB_2 [58, 65]. Monte Carlo simulations show that defects ranging from point defects to cascades are expected [69]. The defect density is also not easily calculated. It is dependent not only on the neutron fluence but also on the sample's chemical composition, with no data being available for pnictides to the knowledge of the author. Previous studies on cuprates [69] have shown that the resulting defect density (given in m^{-3}) is roughly equal five m^{-1} times the fast neutron fluence (given in m^{-2}).

The superconductors are placed in a quartz tube prior to the insertion in the reactor core. Additionally, a nickel foil is inserted in the same tube. It provides information about the actual fast neutron fluence Φ_t experienced by the samples. The nickel foil is activated by the fast neutrons and Ni subsequently decays into Co-58 and Co-60 which are well-known γ -emitters. The resulting γ emission from the two Co isotopes, together with the time elapsed after the start of the irradiation and the mass of the nickel foil can

be used to calculate the fast neutron fluence to which the foil and the crystals inside the quartz tube have been subjected.

The irradiated samples are safeguarded in a specially designed safe in an isotope storage chamber. The material used for the construction of the safe is lead and its door is several centimeters thick to reduce the radiation dose. The irradiated samples are kept in a closed glass which also contains silica gel as means of protection against potential damage caused by humidity.

Chapter 5

Results and discussion

5.1 Critical current anisotropy of the Co-doped BaFe_2As_2 thin film

The available superconducting thin film is well-suited for measurements in the 6 T setup. Firstly, it is important to establish the transition temperature and compare it with literature as a criterion for the quality of the superconductor. The measurement returned a T_c^{onset} of about 26 K as well as a ΔT_c of about 1.6 K. These figures compare well to measurements on films with similar chemical composition and structural architecture [50].

The next objective is to establish $J_c(T, B, \varphi, \theta)$. The selected measurement temperatures are 20, 18, 15, 12, 10, 8 and 5 K. The applied fields are 6 T, 3 T, 1 T, 0.5 T and 0.1 T for all temperatures except 20 K. Since 20 K is already close to T_c , J_c is rather low even for small fields. Therefore, the maximum applied field at this temperature was 0.5 T. B is nearly identical with the $\mu_0 H_a$ since the superconducting bridge has a very small cross section and the self-field resulting from the transport current is in the region of a few tenths μT . The obvious exception is if the applied field is 0.

The available measurement configurations as regards φ and θ have already been presented in Sec. 4.2.1 (see Fig. 4.8). The most basic and well-established configuration is the maximum Lorentz force anisotropy measurement, graphically shown in Fig. 4.8(a). The evaluated $J_c(T, B, \varphi, \theta = 0)$ can be seen in Fig. 5.1 for $T = 15, 10$ and 5 K.

The curves show two maxima which coincide with the positions $H_a \parallel ab$ ($\varphi =$

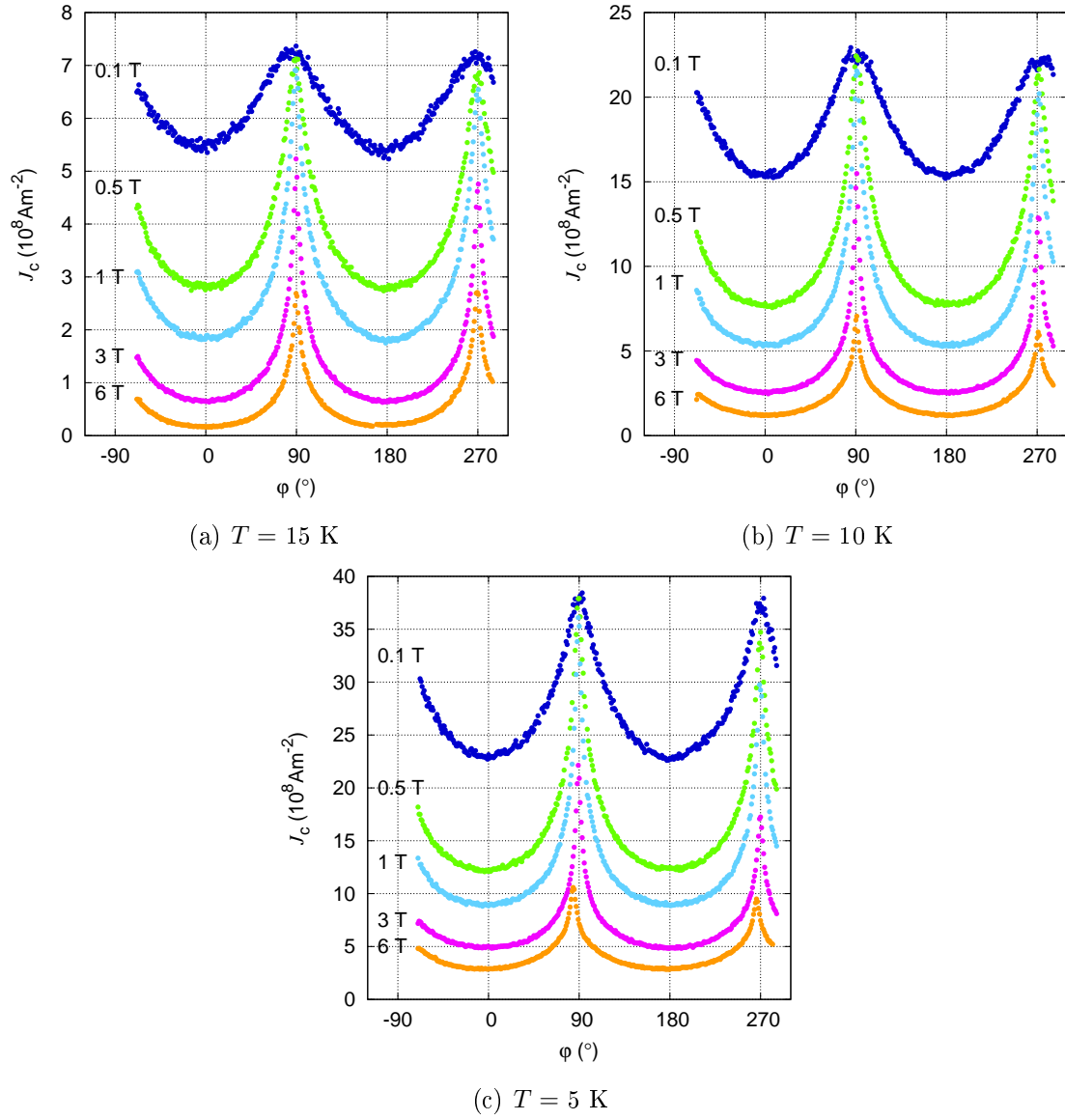


Figure 5.1: J_c anisotropy in the Co-doped Ba-122 film at different temperatures and fields in the maximum Lorentz force configuration

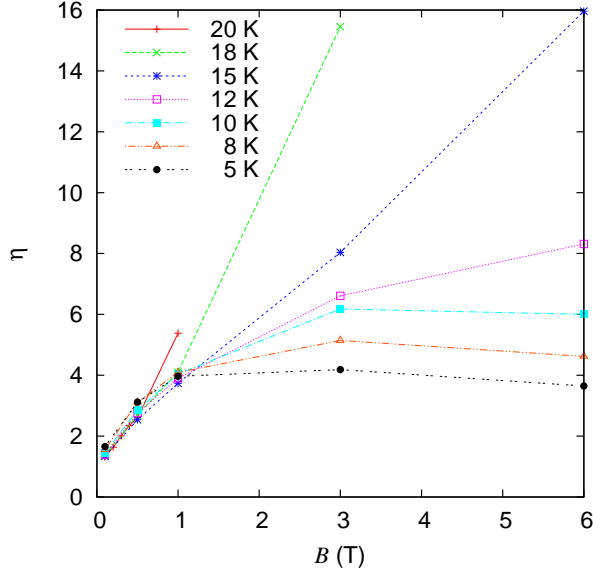


Figure 5.2: Anisotropy of the critical current density in the main orientations for different fields and temperatures

90° and 270°). The only exception is observed at 5 K and 6 T, where the whole curve is shifted by about 5 degrees. A hall probe mounted parallel to the φ -axis shows that the rotation of the sample rod did not deviate from the expected course. This means that the most probable cause for the shift in the J_c curve is a slight movement of the film itself in-between measurements. It is well-known that J_c is anisotropic in Ba-122 thin films due to the anisotropy γ of B_{c2} [50, 71]. In optimally doped Co-doped Ba-122, γ is about 2 at low temperatures [8]. Bearing these facts in mind, it is interesting to plot the anisotropy of the critical current density:

$$\eta = \frac{J_c(H_a \parallel ab)}{J_c(H_a \parallel c)} \quad (5.1)$$

Fig. 5.2 shows η for different temperatures and fields. It is obvious that η changes drastically with temperature and field. This behavior can be easily explained when the anisotropy of B_{c2} and the presence of the planar defects are considered. The upper critical field for $H_a \parallel c$ is reached first and superconductivity is destroyed, therefore $J_c(H_a \parallel c, T) = 0$, while $J_c(H_a \parallel ab, T) \neq 0$. Therefore the high η at high temperatures and fields can be traced back to the anisotropy of the upper critical field. The low field behavior is also easy to understand. The value of η at 0 T is 1 by definition and increases with field. The larger η at 20 K and 1 T is due to the relative proximity to T_c and

respectively low upper critical field. The remaining temperatures show similar values of η up to 1 T. The fact that all temperatures besides 20 K have basically the same η at an intermediate field (1 T) is interesting since both γ and the irreversibility fields vary greatly within the observed temperature range. It is fairly reasonable to suggest that the planar defects which are parallel to the ab -planes and were revealed by TEM studies (see Sec. 3.2) are the dominant factor for the behavior of η up to this field. The behavior of η at higher fields such as 3 and 6 T and temperatures below 15 K is a combination of the temperature dependence of the irreversibility fields and the presence of the planar defects. They act as anisotropic pinning centers, i. e. the flux lines are pinned more efficiently when they are parallel to the defects. In addition to the planar defects, the effect of intrinsic pinning of the flux lines between the Fe-As planes has to be considered as a possible cause for the observed effect. In Co-doped Ba-122, the lattice parameter c is about 1.3 nm [3], while $\xi(0\text{ K}) \approx 1.2\text{ nm}$ [8]. What's more, the radius of the flux lines grows with temperature in accordance to Eq. 2.6. It is therefore highly unlikely that the flux lines will be pinned efficiently between the Fe-As planes, which would lead to a suppression in the condensation energy (this effect is known as intrinsic pinning). In addition, the influence of the planar defects is also revealed in the dependence of $J_c(H_c \parallel ab)$ on B shown in Fig. 5.3. The curves are nearly constant for B up to 1 T, while a well-pronounced dependence on B ($B \leq 1\text{ T}$) has been reported previously [50]. Another interesting feature is observed in Fig. 5.1. The maxima of the critical current at $\varphi = 90^\circ$ & $\varphi = 270^\circ$ do not have the same magnitude. When comparing the magnitudes of the two peaks in J_c in Figs. 5.1(a)- 5.1(c), the one at $\varphi = 90^\circ$ is steadily higher. Similar effects have been reported for cuprates [70] and can be traced back to the different surface barriers in the orientations $\varphi = 90^\circ$ & $\varphi = 270^\circ$. In one case, the Lorentz force acting on the flux lines points to the Fe-buffer layer, while in the other it is directed towards the Au-Pt protective layer. The former is true for $\varphi = 90^\circ$ and higher critical current densities were measured in this orientation. It is conceivable that the reason for this effect is rooted in the different contributions to the pinning of the flux lines of the two surface layers. The Fe-buffer has to be extremely smooth (nm-scale) to enable a homogeneous film growth. This simultaneously creates a very efficient surface barrier for the flux lines within the film. Therefore, when the Lorentz force points in the direction of the buffer layer it is able to use the barrier as a pinning site, resulting

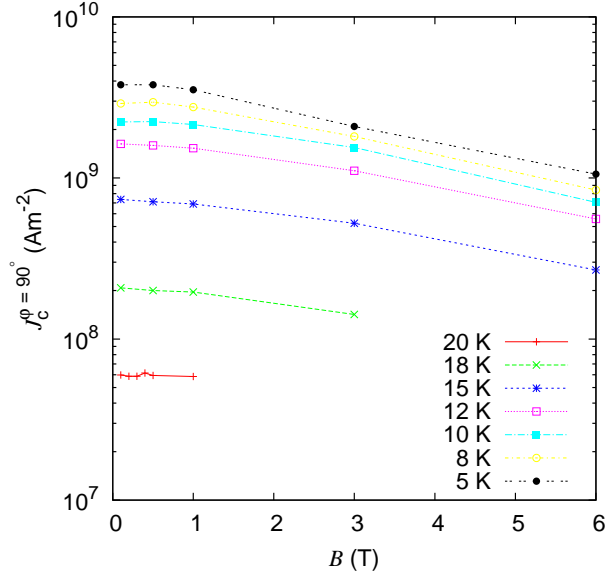
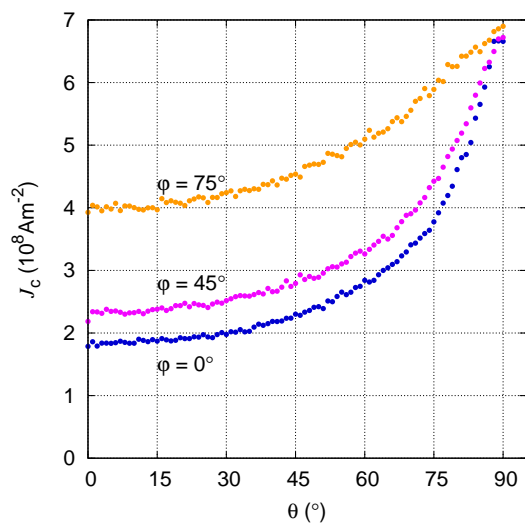


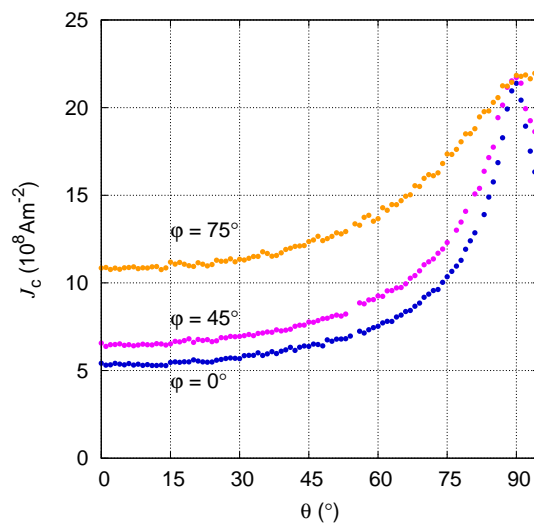
Figure 5.3: $J_c(\varphi = 90^\circ)$ at different fields and temperatures

in an increased J_c . By contrast, the surface layer of Au-Pt is placed simply as means of physical protection, therefore there is no necessity for a smoothness comparable to the one of the Fe-layer. As a result, pinning is expected to be less efficient when the Lorentz force points to the Au-Pt layer and indeed a lower J_c is obtained in this orientation ($\varphi = 270^\circ$). The observed effect increases with B ($B \leq 3$ T) and is more pronounced at low temperatures. This finding is rather interesting since Harrington et al. report that while the difference in the peaks does become more pronounced at lower temperatures, it peaks at about $B = 0.18$ T, contrary to the observations for the Ba-122 thin film. One possible explanation for this difference is the fact that the Ba-122 film examined in this thesis is single crystalline, while the YBCO-based film studied by Harrington et al. is polycrystalline. Additional research is needed to clarify the exact reason for the observed behavior in the Ba-122 film.

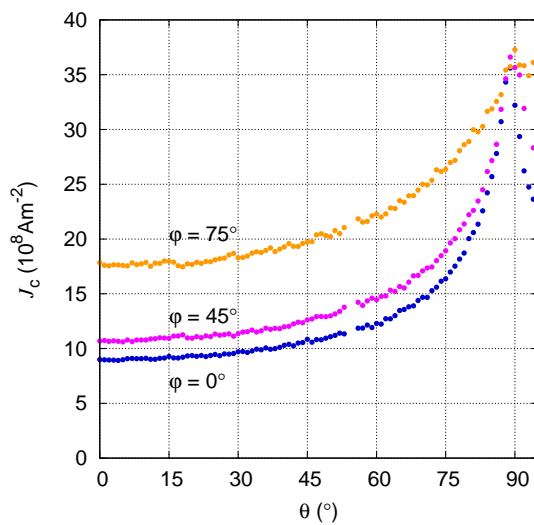
After the completion of the scans in maximum Lorentz force (MLF) orientation, the critical current density is established in variable Lorentz force (VLF) configurations. These measurements are performed at several constant φ angles ($\varphi = 0^\circ, 12.5^\circ, 25^\circ, 45^\circ, 60^\circ, 75^\circ$) and variable θ at the same temperatures and fields as the MLF scans. For $\varphi = 0^\circ$, $\theta = 0^\circ$ corresponds to $H_a \parallel c$ and $\theta = 90^\circ$ - to $H_a \parallel ab$ as well as $H_a \parallel I$. The results for several temperatures and φ s at 1 T are shown in Fig. 5.4. It is clear that J_c increases with rising φ for $\theta \neq 90^\circ$. Interestingly, at $\theta = 90^\circ$ the curves collapse onto the same point. This



(a) $T = 15$ K



(b) $T = 10$ K



(c) $T = 5$ K

Figure 5.4: VLF scans of the Co-doped Ba-122 film at different temperatures and angles φ

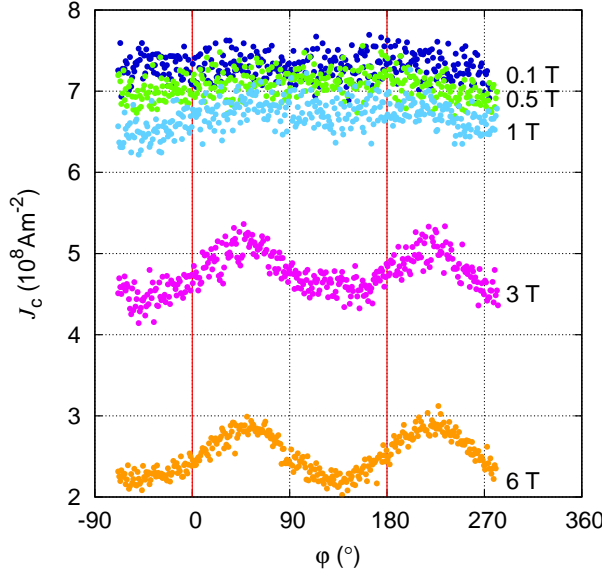


Figure 5.5: In-plane scan at 15 K and different fields

is not expected, since the Lorentz force becomes 0 at $\varphi = 90^\circ, \theta = 90^\circ$ and is not zero for the other φ s. The in-plane scans provide further insight into this seemingly illogical result. In this configuration, only the magnitude of F_L is varied and not the orientation of the applied field to the crystallography of the film. A typical result of an in-plane scan is shown in Fig. 5.5 where the red lines mark the positions for which $F_L = 0$. The orientation of the Lorentz force is steadily perpendicular to the ab -planes, it is only the magnitude that changes. The results are striking. No Lorentz force-free peaks emerge which is in contrast to previous results on anisotropic superconducting thin films (based on cuprate superconductors) which show clear force-free peaks [72]. Complicating matters further are two maxima which emerge at high fields (3 and 6 T) but at seemingly arbitrary positions in terms of the Lorentz force. They are positioned about 45° away from the force-free positions and are 180° apart. A very simple explanation would be a slight geometric misalignment caused by a tilt of the superconducting film with respect to the MgO substrate as well as inaccuracy in the θ alignment. As already explained previously, the starting position of the angle θ is determined optically with a precision of about 1° . Moreover, private communication with the group which fabricated the film revealed that the film is expected to have a tilt of up to 0.5 degrees in the $[110]$ -direction. A total tilt of about 1.5° is therefore plausible. To examine whether this misalignment can cause peaks of the magnitude observed in Fig. 5.5, a highly magnified image around

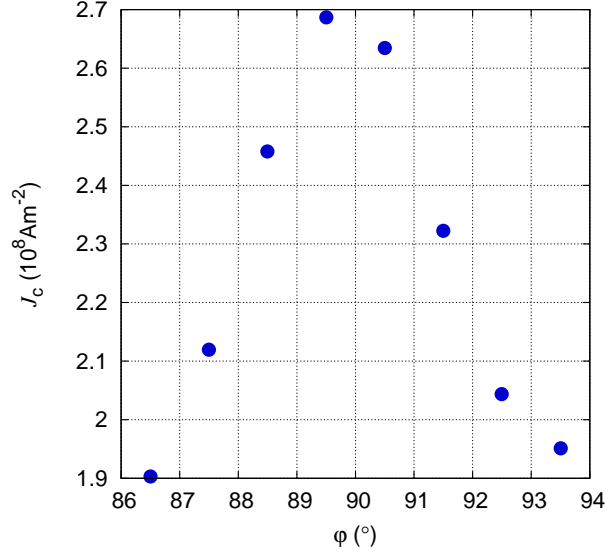


Figure 5.6: Highly zoomed-in image around $\varphi = 90^\circ$ at 15 K and 6 T

$\varphi = 90^\circ$ at 15 K and 6 T is plotted in Fig. 5.6. The peak in both figures has approximately the same value of $2.7 \times 10^8 \text{ Am}^{-2}$. The minimum in the in-plane scan has a value of about $2.3 \times 10^8 \text{ Am}^{-2}$. The next step is to locate the positions in the MLF scan where these J_c s are measured. Fig. 5.6 shows that the peak is extremely sharp and that the critical current drops to from 2.7 to about $2.1 \times 10^8 \text{ Am}^{-2}$ after rotating φ by just 2 degrees. A linear interpolation between the individual data points reveals that J_c decreases from its maximum to $2.3 \times 10^8 \text{ Am}^{-2}$ when φ is approximately 1.5° away from the position where $H_a \parallel ab$. This finding shows that the peaks observed in the in-plane scan are most certainly related to a geometric misalignment of the superconducting film. However, the bigger question still remains: Why are there no force-free peaks in this sample. The search for an answer to this riddle starts with the examination of the Lorentz force and in particular of its vector character.

F_L was already defined in Sec. 2.2. Having already observed the strong J_c anisotropy in MLF scans, resulting from the anisotropic pinning centers in the film, it is sensible to write down the Lorentz force in two components which are either parallel or orthogonal to the ab -planes of the superconductor. To this end, it is necessary to elaborate on the difference between the coordinate systems of the cryostat and the film itself. The rotations take place along axes which are fixed to the cryostat as shown in Fig. 4.7. The labels of the cryostat coordinate system are xyz . It is relatively straight-forward to calculate the Lorentz force in this coordinate system. The following equation shows F_L in dimension

force per length (I_c corresponds to the critical current):

$$\mathbf{F}_L = I_c B \begin{pmatrix} 0 \\ \cos \theta \\ -\sin \varphi \sin \theta \end{pmatrix} \quad (5.2)$$

Note that the Lorentz force is 0 per definition along the x -axis since $B \parallel x$. However, it is obvious that the crystallographic structure of the film does not remain fixed to these coordinates during the anisotropy scans, therefore a transformation to a film coordinate system is necessary to break down the Lorentz force as desired. The vectors e_1, e_2 and e_3 (see Fig. 4.7) can be expressed via the two angles θ and φ :

$$\mathbf{e}_1 = \begin{pmatrix} -\sin \varphi \\ \cos \varphi \\ 0 \end{pmatrix}, \quad \mathbf{e}_2 = \begin{pmatrix} \cos \varphi \sin \theta \\ \sin \varphi \sin \theta \\ \cos \theta \end{pmatrix}, \quad \mathbf{e}_3 = \begin{pmatrix} \cos \varphi \cos \theta \\ \sin \varphi \cos \theta \\ -\sin \theta \end{pmatrix}. \quad (5.3)$$

The introduction of a coordinate system fixed to the sample allows expressing the component of the Lorentz force which is parallel to the ab planes (in-plane Lorentz force) in dependence of θ and φ :

$$\mathbf{F}_L^{\parallel} = -I_c B \cos \alpha \begin{pmatrix} -\sin \varphi \\ \cos \varphi \\ 0 \end{pmatrix} \quad (5.4)$$

where $\alpha \angle H_a, c$ and $\cos \alpha := \cos \varphi \cos \theta$. The absolute value of the in-plane component of the Lorentz force is:

$$F_L^{\parallel} = -I_c B \cos \alpha \quad (5.5)$$

This result means that the angular dependence of the in-plane Lorentz force is reduced to the angle α . This finding becomes very intriguing in light of the in-plane scan results. In this configuration $\theta = 90$, therefore $F_L^{\parallel} = 0$ due to $\cos \alpha = \cos \varphi \cos \theta = 0$. This means that the critical current in the film remains unchanged (if geometric misalignment is neglected) when $F_L^{\parallel} = 0$. Expanding this idea further, it is tempting to consider the notion that J_c depends solely on the in-plane component of the Lorentz force in all configurations. To prove the validity of this approach, it is useful to map the results of all scans in MLF and VLF configurations to α and plot the results for different temperatures

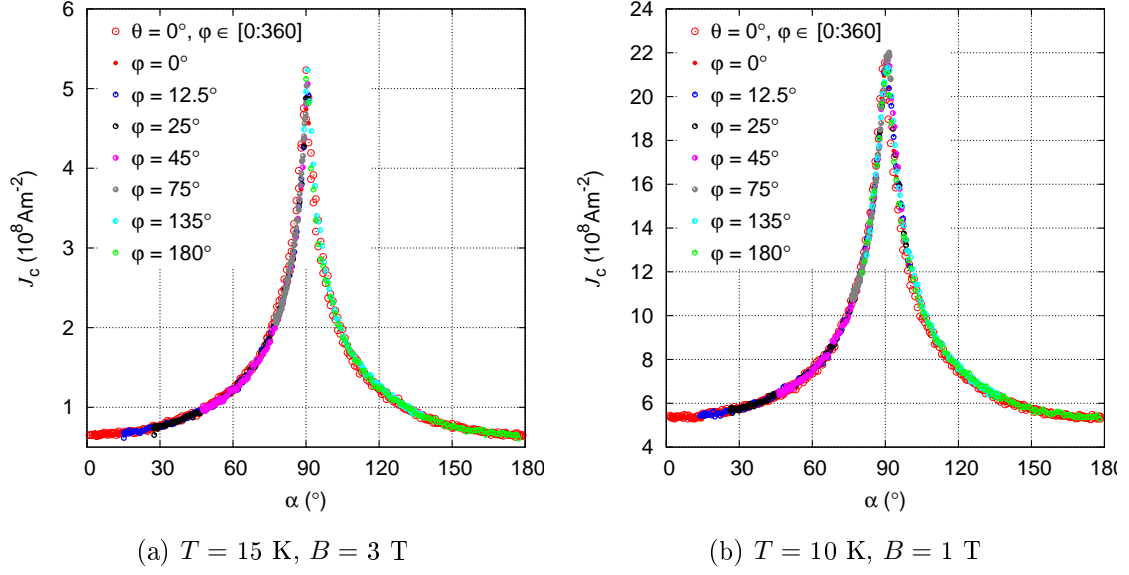


Figure 5.7: Dependence of the critical current density on α for different temperatures and fields

and fields. Two examples at different fields and temperatures are shown in Fig. 5.7. The mapping of J_c to α functions remarkably well. In essence, this is the final and most telling confirmation that J_c depends only on the orientation between the applied field and the crystallographic structure of the film. This effect can be described as one dimensional pinning behavior, with the sole dimension of importance being α [51]. A further conclusion is that the out-of-plane Lorentz force F_L^\perp is completely compensated by the planar defects, which are by far the strongest pinning centers in the film.

An alternative approach to the α -scaling is presented by Tachiki and Takahashi in the case of pancake vortices in layered superconductors [73]. However, pancake vortices are not expected in the examined film since the ratio between the lattice parameter c and the radius of the flux lines is too low. In addition, the data from the MLF scans does not follow the predictions of the model when scaled to the out-of-plane component of the magnetic field $B^\perp = B \cos(\varphi)$. $J_c(B^\perp)$ is shown in Fig. 5.8. For fields below 1 T, the peak values of the critical current density collapse onto a single point, which is in contradiction to the predictions of the Tachiki/Takahashi model. This finding does however support the argument that the current limiting mechanism is the in-plane Lorentz force. As the field increases, the J_c value at the peak decreases, thus the B^\perp scaling loses its validity. The reason is the increasing effect of vortex-vortex interaction. These considerations provide ample arguments in favor of the α scaling since it is independent on the density

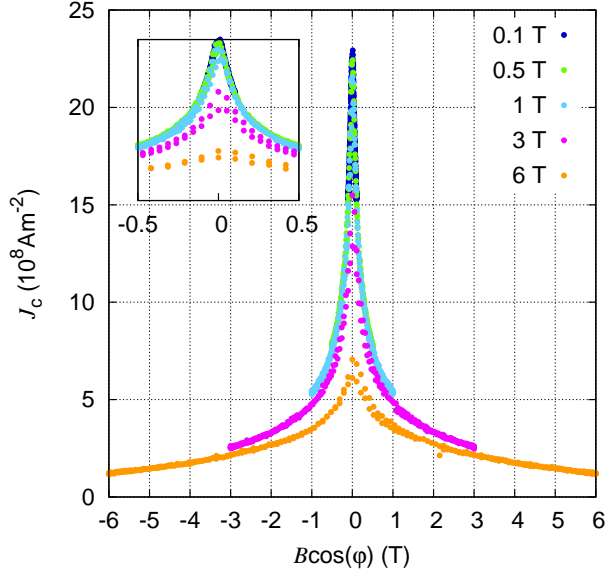


Figure 5.8: Scaling of the critical current density to the out-of-plane component of the magnetic field at 10 K

of vortices and is derived purely from geometric considerations.

The results obtained from the measurements on the superconducting thin film provided the first milestone result within the thesis. The extreme case of highly anisotropic planar defects in a thin film led to the observation of a one-dimensional pinning behavior, whereby J_c is limited merely by the in-plane component of the Lorentz force and is independent on the magnitude of its out-of-plane component.

5.2 Critical current anisotropy in Ba-122 based superconducting single crystals

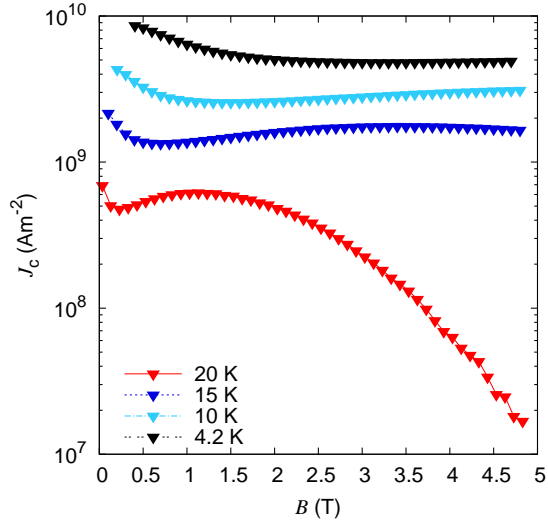
The previous section showed the anisotropy of the critical current density in a single crystalline thin film based on a Co-doped Ba-122 superconductor and its one dimensional pinning behavior. The presence of planar defects caused the unique effect. It is also well-known that a wide variety of pinning defects result from the growth process of a thin film [74]. It is therefore rather difficult to draw conclusions regarding the role of a particular defect class unless it has a contribution as dominant as for instance observed in Sec. 5.1. However, there is another sample class beside thin films which allows the characterization and examination of flux pinning within a single superconducting grain:

single crystals.

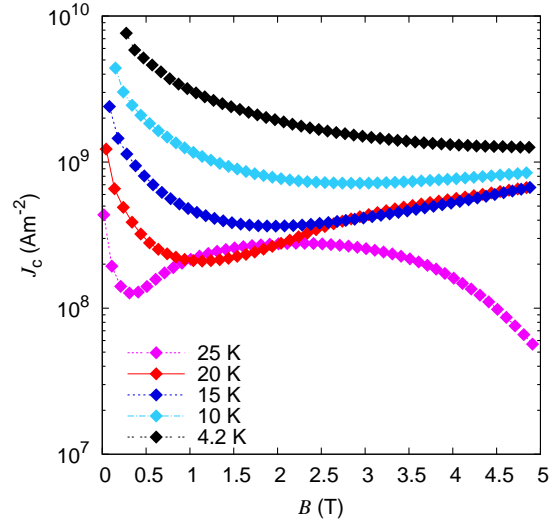
Numerous studies on the critical current density in differently doped Ba-122 based superconducting single crystals have been performed already [10, 11, 13, 14, 100]. Yet there is one important link which is missing, namely the critical current anisotropy. Due to the very high currents necessary to achieve J_c in single crystals, transport measurements are almost impossible (with the exception of FIB structured crystals [52]). Even though magnetization measurements are a long-standing and well-established technique for determining J_c in bulk superconductors, there has been no quantitative study on the dependence of the critical currents on the orientation of the applied field to the orientation of the crystal. This is made possible in this work by a combination of the vector VSM and an evaluation procedure which takes into account the effects of variable Lorentz forces and the changing orientation of the self-field. The following paragraphs provide details on the results and conclusions drawn from the experiments.

The special properties of the VSM were already described in detail in Sec. 4.1.3. The first task is to prepare suitable crystals for the angle resolved measurements. The quality of the available Ba-122 samples was excellent, but there are additional requirements which have to be met. These are connected to the application of the anisotropic Bean model. It is imperative to properly evaluate the critical current density flowing under maximum (J_c) and variable Lorentz forces (J_c^{VLF}) in the crystal. Please note that, as already mentioned previously, the currents flow steadily within the ab -planes for a broad angular range up to $\vartheta = \angle H_a, c \approx 75^\circ$ for $a = b = 10c$. This is a purely geometric effect and was first shown for isotropic superconductors in an earlier result [75]. It is also confirmed for Ba-122 crystals. This finding is of paramount importance since it reduces the evaluation procedure to the ‘pure’ anisotropic Bean model without any tilting of the current loops. Such a tilt is problematic for two reasons. First, the calculation of J_c from m_{irr} becomes more complicated since there is no longer a closed expression. This hurdle can be tackled, but the second problem is much more difficult to solve. It concerns the currents flowing along the c -axis (J_c^c) which would come into play if the current loops were tilted. J_c^c is usually lower than the currents flowing within the ab -planes in layered superconductors. Its presence adds a third current (beside J_c and J_c^{VLF}), which makes a proper evaluation of the separate current densities nearly impossible. Therefore, the evaluation region is restricted in accordance to the individual crystal’s geometry.

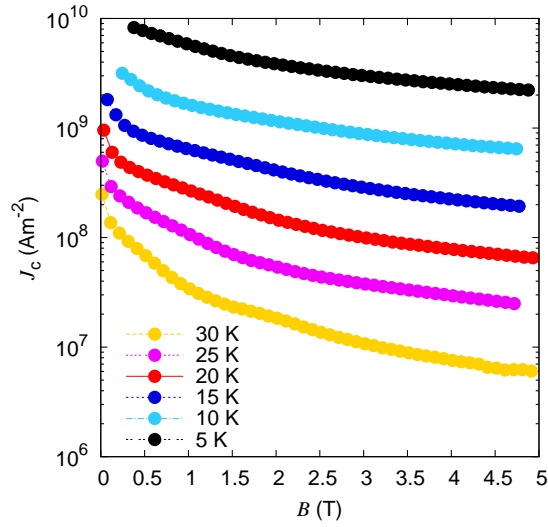
The pristine crystals have distinctively different flux pinning characteristics. The transition temperatures were all close to the maxima reported for the respective doping type (see Sec. 5.3.1). Basic measurements at $\vartheta = 0^\circ$ were first carried out which provide information regarding the critical current within the ab -planes without any influence of variable Lorenz forces. The results for the three different optimally doped crystal types are shown in Fig. 5.9. Several interesting features are revealed by these figures. The Co- and P-doped crystals show a second peak in the critical current density, while the K-doped sample does not. This effect is called the ‘fishtail’ effect and is caused by an order-disorder transition of the flux line lattice [76, 77, 78, 79]. This phenomenon has been studied extensively, therefore only a brief description is provided in the next few lines. At low fields, the flux lines in the Co- and P-doped crystals are ordered in a nearly perfect hexagonal lattice, i. e. in the configuration which is energetically most favorable as calculated by Abrikosov. This state remains unchanged until a certain number of flux lines in the crystal is reached which corresponds to a specific magnetic induction known as B_{onset} . From then on, the flux line lattice no longer has a nearly perfect hexagonal shape over the whole cross-section of the crystal. Instead, individual flux lines are pinned to defects within the superconductor and the lattice is disordered. In an interesting twist, the K-doped crystal does not show a fishtail effect, while J_c is also much lower at higher temperatures and fields in comparison to the other two crystals. These two points suggest that this particular crystal type has a weak pinning landscape, regulated by small, point-size defects. The distinctive rise of J_c with decreasing temperature can be explained with two individual arguments. First, the thermal activation of flux lines is much weaker at low temperatures as a result of the decreasing thermal energy. Both large (nm-scale) and small (point-like) defects have to compensate the same thermal energy at a given temperature. Point-like defects have lower pinning energy due to their smaller size, therefore they are less effective when higher thermal energies are present. As the temperature decreases, they become more efficient in compensating thermal depinning to the reduced thermal energy. An additional argument can be considered since ξ also decreases with decreasing temperature. At the same time, the radius of the pinning centers can be observed as nearly constant. This means that as T goes down, each pinning center saves a larger portion of a flux line’s volume, i. e. the pinning energy of each center increases, leading to a larger J_c .



(a) Co#4



(b) P#1



(c) K#5

Figure 5.9: J_c in differently doped Ba-122 single crystals in the main orientation $\vartheta = 0^\circ (H_a \parallel c)$

The weak pinning behavior in the K-doped crystal, in combination with the moderate γ of the compound, raises some very intriguing possibilities with respect to scaling of the critical current density. A well-known scaling approach was suggested by Blatter, Geshkenbein and Larkin (BGL) [80] for weak collective pinning in the special regime of single vortex pinning. The following scaling factor $\epsilon(\vartheta)$ is typically used to scale the magnetic field B :

$$\epsilon(\vartheta) = \sqrt{\gamma^{-2}\sin^2(\vartheta) + \cos^2(\vartheta)} \quad (5.6)$$

The basic idea of various scaling approaches is to derive the angular dependence of further superconducting properties by means of simple rules [80, 81]. For instance, the magnetic field B has to be replaced by $\epsilon(\vartheta)B$ in any function of B , in particular in $J_c(B)$. Current scaling is less obvious than field scaling since it is closely related to the problem of the statistical summation of elementary pinning forces. Quantitative solutions of this problem are only available in a few limiting cases, for instance for weak collective pinning. It was found that no current scaling is needed in the single vortex pinning regime, hence pure field scaling is sufficient to describe the angular dependence of J_c in this case [80]. This approach has been frequently used [82, 83, 84, 85] although neither the magnitude of the currents nor their field dependence fit the predictions of weak collective pinning theory. However, as pointed out at the beginning of the section, these studies have been carried out on thin films and not on single crystals. For the first time ever, it is possible to apply the scaling approach to J_c in single crystals with a much better defined defect structure.

The K-doped single crystal most likely fulfills the criteria set by the BGL approach. Now, the experimental side has to be tackled. One important requirement which has to be met is related to the geometry of the crystal. Since there is no data on the influence of variable Lorentz forces in Ba-122 based single crystals, it is important to ensure that the crystal has distinctively different lateral dimensions, i. e. a ratio of $a = 3b$ is preferable. This is necessary in order to apply the anisotropic Bean model as described in Sec. 2.2. To complete this objective, a K-doped crystal was cut into 2 parts with a scalpel. One of the resulting pieces is K#4, where $a \approx 3b$ (see Tab. 3.1). It is now possible to perform magnetization loops on the crystal according to the procedure described in Sec. 4.1.3. Fig. 5.10(a) shows $J_c(\vartheta)$ at different fields with $T = 25$ K. The curves show a steady increase with ϑ which is an expected result of the anisotropy of B_{c2} . To check whether a pure field scaling approach can be applied to this single crystal, it is necessary to

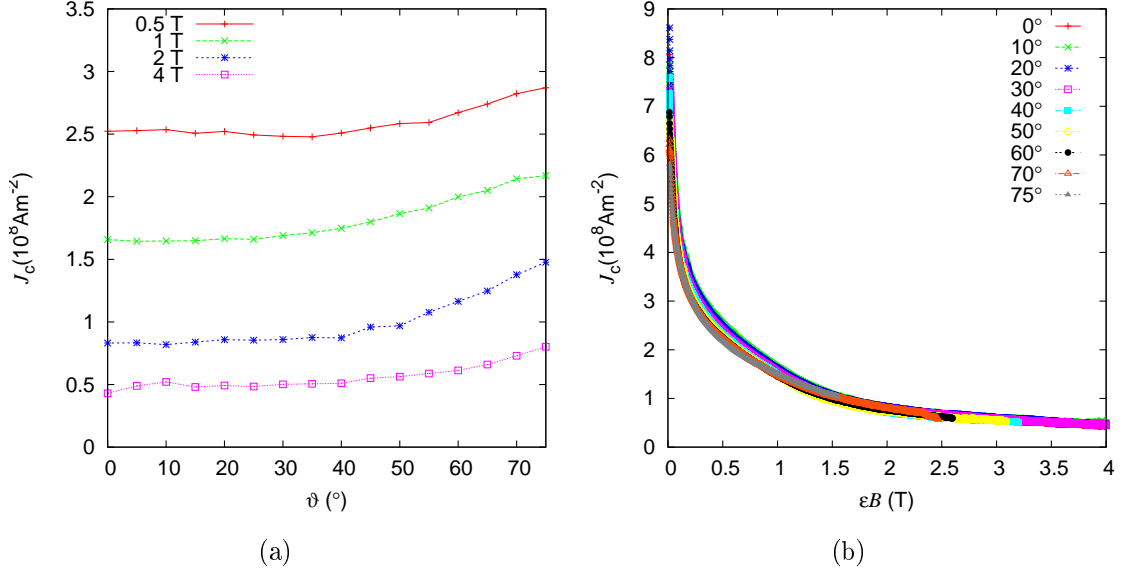


Figure 5.10: $J_c(\vartheta)$ of K#4 at 25 K and different fields (left panel) and application of pure field scaling to the results (right panel)

calculate ϵ first. The parameter γ can be either fitted, extracted from literature or, in the best case scenario, established for the crystal in question. The latter option was possible with help of resistive measurements and an extrapolated value for $\gamma \approx 2.2(T = 25 \text{ K})$ was found. Detailed results from the resistive measurements are available in Sec. 4.2.2. Having determined the scaling parameter ϵ , the scaling of $J_c(\epsilon B, \vartheta)$ is straight-forward and the results at 25 K are shown in Fig. 5.10(b). The scaling functions reasonably well, considering the fact that the approach is based on the limiting case of single vortex collective pinning.

The successful application in the case of weak collective pinning is, however, merely the first step. Of much greater interest are materials that exhibit strong pinning, particularly since they are of relevance for technological applications. Therefore, the next crystal analyzed is Co#1 which exhibited a well-pronounced fishtail effect at all temperatures (see Fig. 5.9(a)) indicative of a stronger pinning in comparison to the K-doped crystal. Showing the angular evolution of the second peak effect in J_c is another highly intriguing (and thus far unexplored) feature. Once again, the measurements were carried out in the vector VSM and evaluated in accordance with the anisotropic Bean model. A three-dimensional representation of the fishtail evolution at $T = 17.5 \text{ K}$ is shown in Fig. 5.11, where the shift in the second maximum's position is shown with a straight line in the xy -plane of the figure. Please note that here the angle $\vartheta = \angle \vec{H}_a, \vec{c}$ is replaced by $\vartheta_B = \angle \vec{B}, \vec{c}$

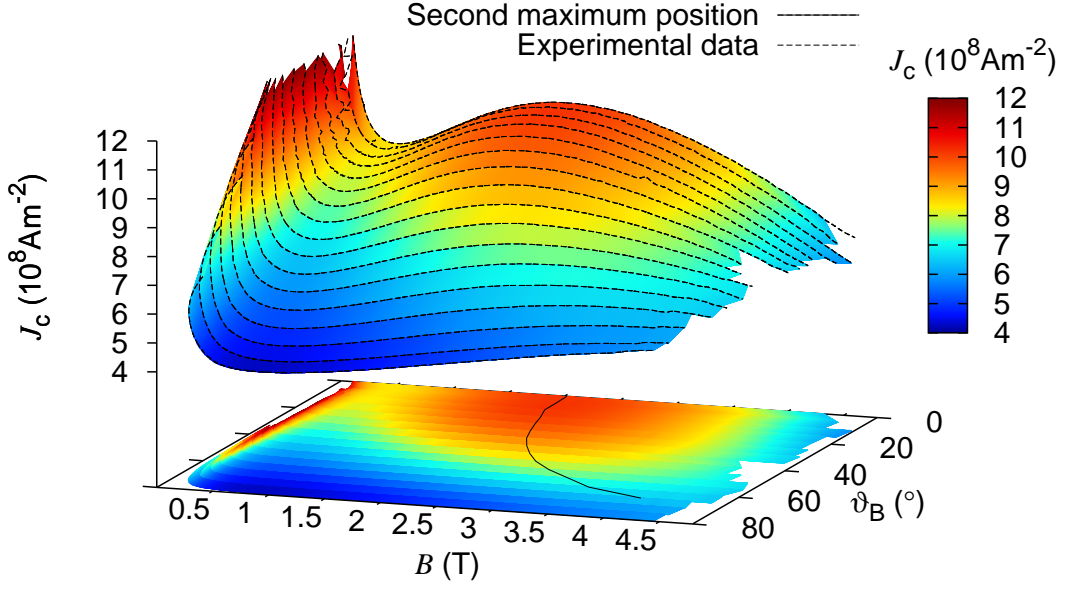


Figure 5.11: Angular evolution of the fishtail effect in a Co-doped Ba-122 single crystal at 17.5 K

in the plot. The effect is easily observed at very low fields where ϑ_B shows a strong drop towards 0° as anticipated. The graph reveals two interesting features. Firstly, the fishtail peak shifts to higher fields with increasing ϑ_B , which is expected when thinking along the lines of pure field scaling. It is plausible that reducing the field from $B \rightarrow \epsilon B$ as suggested by such an approach would align the maxima. However, it is obvious that the maximum changes not only its position, but also its magnitude. J_c at the second maximum decreases with increasing ϑ_B . This cannot be accounted for by pure field scaling, since reducing the field simply shifts the J_c curves but does not change their magnitude. Two figures help illustrate this conundrum. Fig. 5.12(a) shows the critical current density at different fields and $T = 17.5$ K for varying ϑ ($\vartheta \approx \vartheta_B$ for $\mu_0 H_a = 0.5$ T). The shift of the second maximum causes an inverse anisotropy in J_c : The critical current decreases with ϑ for fields up to about 3 T. At higher fields, an apparent crossover is reached where J_c first rises and then drops with ϑ . This effect could in theory be explained by the presence of the fishtail and its expected shift to higher fields with ϑ . These results are complemented by applying pure field scaling on the results for this crystal. The parameter $\gamma \approx 2.3(T = 17.5 \text{ K})$ was determined from resistive measurements. The curves become

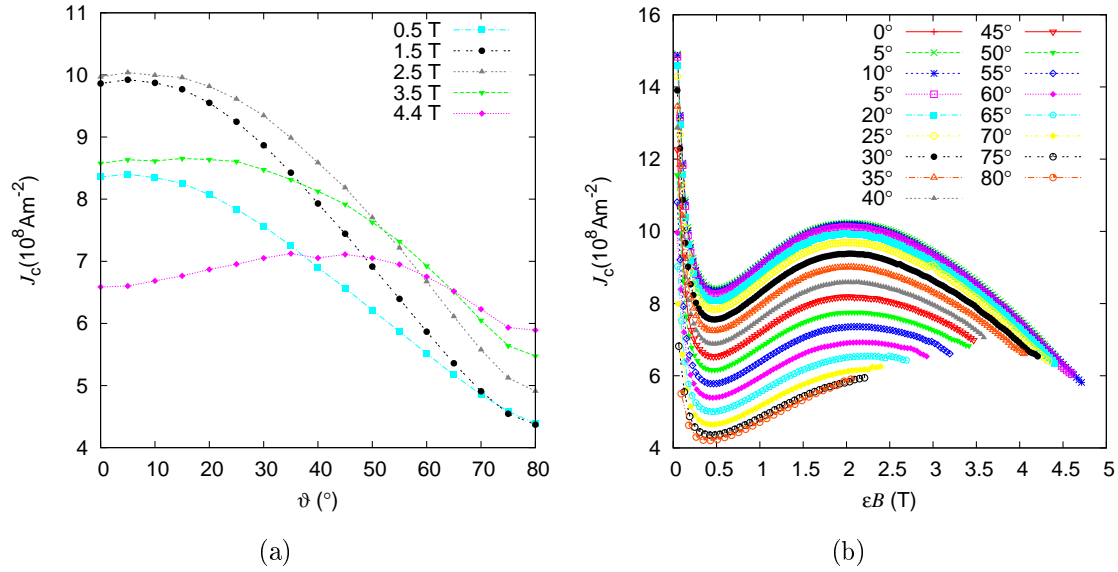


Figure 5.12: $J_c(\vartheta)$ of Co#1 at 17.5 K and different fields (left panel) and application of pure field scaling to the results (right panel)

approximately parallel to each other, but they do not collapse onto a single curve. It is apparent that pure field scaling is not sufficient to explain the angular dependence of J_c in this single crystal. To complicate matters further, the nature and shape of the defects which are responsible for pinning cannot be surmised, while the presence of an order-disorder transition makes it even more difficult to provide a quantitative description of the observed effect.

The deadlock from the previous paragraph may be solved if an isotropic pinning landscape overrides the original defect structure in the crystal. Fast neutron irradiation is a viable option for creating the necessary landscape (see Sec. 4.3). The resulting defect structure consists of spherical defects with radius up to several nanometers distributed randomly within the crystal. An additional effect from the irradiation is the disappearance of the second maximum in J_c since the flux line lattice is now disordered at all fields. Finally, the introduced pinning landscape enables the analysis of the strong pinning limit. A further Co-doped crystal, Co#3, was irradiated to a fast neutron fluence of $5.5 \times 10^{21} \text{ m}^{-2}$. Following the irradiation, the critical current rises distinctively, while the inverse anisotropy already observed in the case of the pristine Co-doped crystal perseveres as shown in Fig. 5.13(a).

Since there is no longer a second maximum in J_c , the inverse anisotropy of the critical current at low fields must have another origin. To explain this result, the interplay

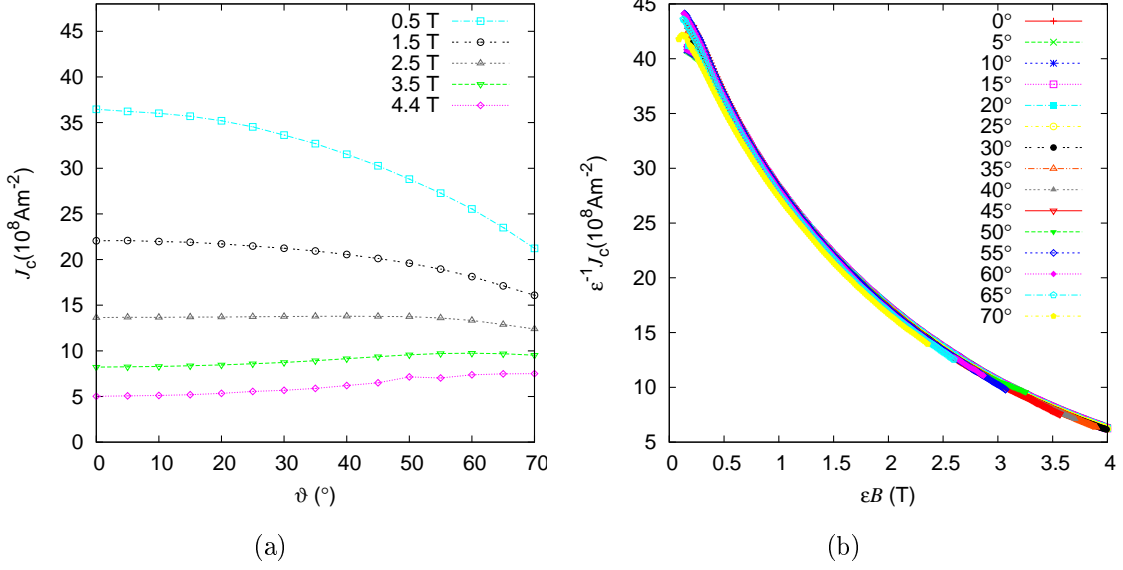


Figure 5.13: $J_c(\vartheta)$ of Co#3 at 17.5 K and different fields (left panel) and application of both field and critical current scaling to the results (right panel)

between the pinning landscape in the single crystals and the flux line lattice in both limits is considered. While weak pinning (by point-like defects) dominates in the pristine K-doped crystal, a shift to strong pinning (by nano-sized spherical defects) induced by the fast neutron irradiation is observed in the irradiated sample. The angular variation of the coherence length $\xi(\vartheta) = \xi_{ab}\epsilon(\vartheta)$ (Fig. 5.14(a) and Fig. 5.14(d)) [81, 86], together with the finite size (similar or larger than the coherence length) of the strong pinning centers, imply an angular dependence of the pinning energy $E_p \propto E_c r_d \xi_{ab} \xi(\vartheta)$ [68], where E_c and r_d denote the (isotropic) condensation energy density and the defect radius, respectively. Note that the elementary pinning force is independent of angle since $f_p \sim E_p/\xi(\vartheta)$. In a direct summation limit, this also holds true for the volume pinning force $F_p = J_c B$, which in turn implies scaling of J_c by $\epsilon(\vartheta)$. By contrast, defects with a radius smaller than ξ_c (Fig. 5.14(c) and Fig. 5.14(f), where ξ_c is the coherence length along the c -axis) always save the condensation energy in the same volume, regardless of ϑ . As a result, F_p now grows with θ ($F_p \rightarrow F_p \epsilon^{-1}$) which means that no J_c scaling is needed. This leads us back to the result of the BGL scaling for weak pinning. These geometrical arguments illustrate the crucial importance of the relation between the size of the defects and $\xi(\vartheta)$ for the pinning energy E_p . Since ξ_{ab} is between 2 and 3 nm in Ba-122 [7, 8], the irradiation induced defects fulfill the requirement $r_d > \xi_{ab}$ and E_p declines with ϑ .

These considerations lead to the idea of double scaling: The field is reduced by ϵ as in

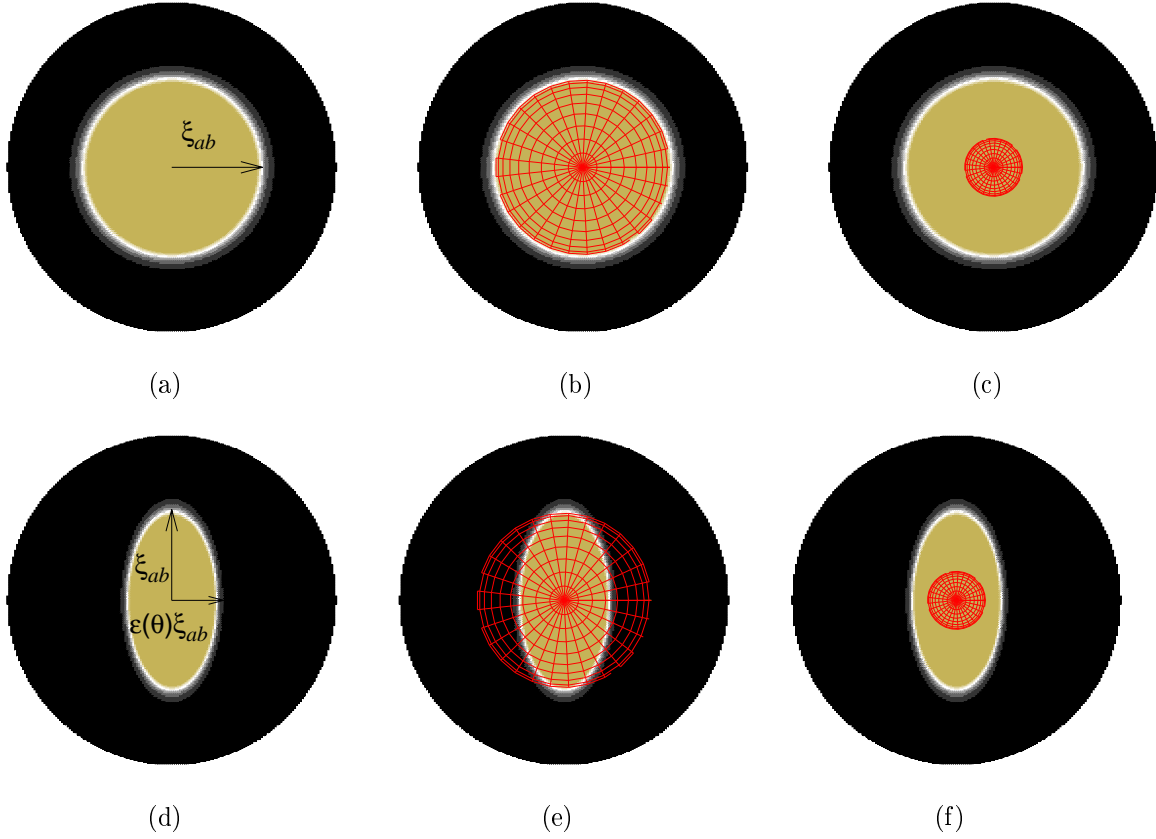


Figure 5.14: The figure shows the significance of the size of a defect which pins a vortex core. a) shows an unpinned vortex core for $H_a \parallel c$, while d) illustrates the shrinkage of a vortex core with θ . b) and e) show the change in the pinning energy from $E_p \propto \xi_{ab}^2 r_d$ to $E_p \propto \xi_{ab}^2 \epsilon(\theta) r_d$ due to the interaction of a large defect (radius $\geq \xi_{ab}$) with the vortex core in each case, while c) and f) illustrate the constant pinning energy ($E_p \propto r_d^3$) when a small defect pins the vortex core.

the pure field scaling, while the changes in the condensation energy with ϑ are accounted for by scaling the current with ϵ . The results for Co#3 are shown in Fig. 5.13(b). The curves collapse beautifully onto a single curve, indicating the successful application of the proposed approach. It should be noted that no fit parameters were used in scaling the curves since γ was determined experimentally. One important facet of this study is that scaling depends solely on the interplay between an isotropic pinning landscape within the superconductor's crystallographic structure and the flux line lattice. Therefore this model can be applied to any superconducting material which exhibits an isotropic defect structure.

A similar study which was carried out on another iron-based superconducting single crystal from the 1111 family (Nd-based) which showed a comparable effect [68]. It should be noted that the work on the Nd-1111 sample was hindered by the very small size and irregular shape of the crystal. The lateral dimensions were $0.5 \times 0.36 \text{ mm}^2$, which makes structuring the crystal with a scalpel next to impossible, therefore the crucial separation of the critical current into J_c and J_c^{VLF} is not possible. The result is that the double scaling does not work so well since the evaluated current density is an average of the two individual critical current densities. Nevertheless, the extracted results are strongly indicative that the approach described in the previous paragraph is applicable to the 1111 system too.

There are further examples in literature where pure field scaling does not function [87] or where the anisotropy parameter differed from the real γ is necessary to apply the approach successfully [82, 84]. Here, it is shown that ascribing deviations from pure BGL field scaling to an anisotropic defect structure is a priori not justified. The suggested approach provides (at the very least) a qualitative explanation for a decreasing or non-monotonic $J_c(\vartheta)$ even for an isotropic defect structure and thus explains a lot of literature data, where pure field scaling failed. In the high- T_c superconductor $\text{YBa}_2\text{Cu}_3\text{O}_7$ (Y123), for instance, BaZrO_3 particles with a diameter of 7-10 nm were introduced, whose size is larger than the coherence length of the superconductor. This meets the requirements for double scaling and a broad maximum in $J_c(\vartheta)$ centered around $H_a \parallel c$ has indeed been observed [87]. Additionally, broad peaks in the angular dependence of J_c not centered at 0 or 90° [88, 89, 90] can be explained by an isotropic defect structure. These peaks can be much more significant in $\text{YBa}_2\text{Cu}_3\text{O}_7$ than the maxima above 50° in the irradiated

iron-based crystal (Fig. 5.13(a)) because of the higher anisotropy in the cuprate-based superconductor in combination with a different $J_c(B)$. For instance, the local maxima in the angular dependence of J_c in coated conductors are a result of the introduction of an isotropic defect structure by neutron irradiation [90].

The extension of the well-known pure field scaling with current scaling to take into effect the interaction of vortices in an anisotropic superconductor with an isotropic defect landscape is the second major result achieved within the course of this PhD thesis.

5.3 Effects of fast neutron irradiation

The anisotropy of the critical current density flowing under maximum Lorentz force in superconducting single crystals was tackled in the previous section. The result was the extension of the well-established pure field scaling to a double scaling which takes into account the presence of an isotropic defect structure in the superconductor and its interaction with the flux line lattice. This effect was most certainly the highlight of the thesis in terms of scientific impact. However, a number of other important results regarding the effects of fast neutron irradiation experiments were obtained. The basic idea of irradiation, as already explained in detail in Sec. 4.3, is the introduction of artificial pinning centers in the single crystals and the subsequent characterization of their influence on the superconducting properties. The changes in four fundamental parameters (J_c, T_c, B_{c2} and the irreversibility lines) are elaborated in this section.

5.3.1 Changes in the transition temperature

The transition temperature T_c is evaluated according to the procedure described in Sec. 4.1.1. Here, the changes in the onset of superconductivity and in the transition width are highlighted since they provide thorough insight into the suppression of superconductivity by the introduction of additional impurities and scattering centers. The crystals Co#4, P#1 and K#5 underwent two irradiation steps, whereby the fast neutron fluence read $1.8 \times 10^{21} \text{ m}^{-2}$ at each step. The result is that after the second round in the reactor, the total fluence reaches a value of $3.6 \times 10^{21} \text{ m}^{-2}$. First, the results from AC susceptibility measurements performed on the differently doped crystals are shown in Fig. 5.15. Please note that the potassium doped crystal K#5 was measured with $H_a \parallel ab$

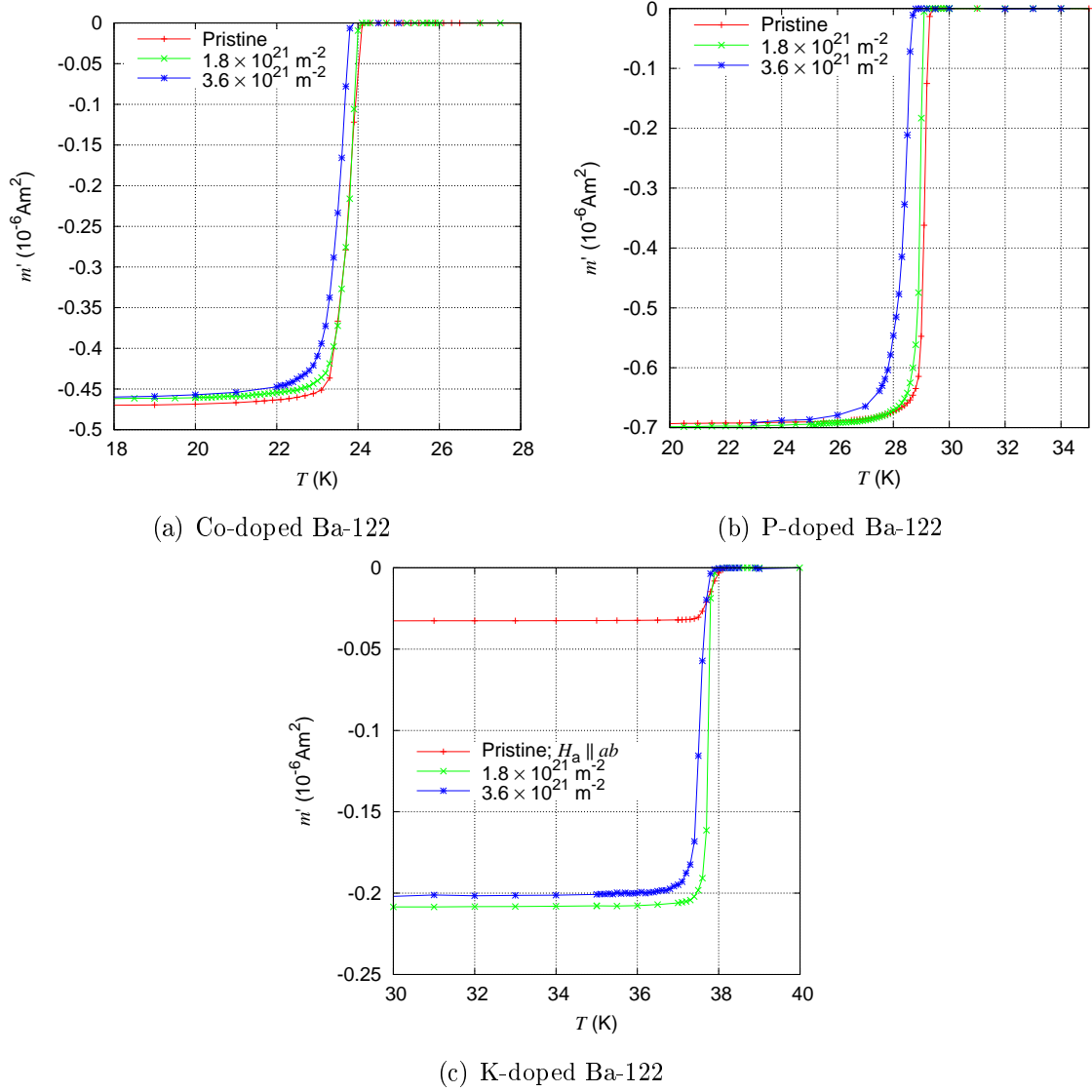


Figure 5.15: T_c in differently doped Ba-122 single crystals in the pristine state and after irradiation to different fast neutron fluences

in the pristine state. As a result, the maximum response signal is significantly lower since D is about 7 times smaller in this configuration. Additionally, the transition width cannot be determined from this measurement, therefore the result for K#4 is also shown in the table to enable a comparison of ΔT_c prior to and after irradiation for this doping type. The evaluated values of T_c^{onset} and ΔT_c are provided in Tab. 5.1. The differences in the transition widths in the pristine crystals can be explained by stronger scattering in the Fe-As planes in the Co- and P-doped crystals since the dopants replace the Fe and As atoms respectively. The table also shows that T_c drops more or less linearly with increasing fluence. The P-doped and K-doped crystals showed stronger decreases than the Co-doped one. It is conceivable that this effect is due to a higher sensitivity to air

| Sample | $T_c^{\text{onset,pris}}$ (K) | ΔT_c^{pris} (K) | $T_c^{\text{onset,irr}}$ (K) | ΔT_c^{irr} (K) | δT_c (K) | f (10^{21} m^{-2}) |
|--------|-------------------------------|--------------------------------|------------------------------|-------------------------------|------------------|----------------------------------|
| Co#4 | 24.2 | 0.7 | 24.05 | 0.7 | 0.15 | 1.8 |
| — ” — | — ” — | — ” — | 23.8 | 0.79 | 0.4 | 3.6 |
| P#1 | 29.4 | 0.4 | 29.1 | 0.5 | 0.3 | 1.8 |
| — ” — | — ” — | — ” — | 28.7 | 0.89 | 0.7 | 3.6 |
| K#4 | 38.25 | 0.1 | - | - | - | - |
| K#5 | 38.4 | - | 38.2 | 0.2 | 0.2 | 1.8 |
| — ” — | — ” — | — ” — | 37.8 | 0.39 | 0.6 | 3.6 |

Table 5.1: T_c s and transition widths of the single crystals before and after irradiation

and humidity. All three crystals were irradiated from $1.8 \times 10^{21} \text{ m}^{-2}$ to $3.6 \times 10^{21} \text{ m}^{-2}$ together in the same quartz tube and no protective gas (typically He or Ar) was used. By contrast, the first irradiation of the K#5 included enclosing the crystal in a quartz tube filled with He as means of protection against degradation. The other two doping types show better linearity in $T_c(\Phi_t)$. However, the fact that only three data points are available, as well as the measurement precision of 0.05 K makes it difficult pinpoint the exact cause for the stronger decrease in the K-doped and P-doped crystals after the second irradiation step.

The changes in the transition temperature can be compared to previous irradiation studies. Results from fast neutron, proton, electron and heavy ion irradiation experiments are available. The data from prior reports on the reduction of T_c in Co-doped Ba-122 single crystals after fast neutron irradiation show comparable results with the data acquired here [10] despite the slightly different nominal doping levels ($\text{Co}_{0.12}$ in this thesis compared to $\text{Co}_{0.2}$ in the study by Eisterer et al.).

Proton irradiation has a distinctively different defect creation mechanism than neutrons. The latter are electrically neutral and, for fast neutrons, the most common interactions are elastic collisions with nuclei in the irradiated sample. In contrast, protons have a positive electric charge, thus electronic (Coulomb) interactions dominate. The available reports on proton irradiation Co-doped Ba-122 show a much more significant drop in T_c (about 1 K) for a proton fluence of $1.2 \times 10^{20} \text{ m}^{-2}$ [11]. This is an intriguing result, since the proton fluence is less than a tenth of the fast neutron fluence used in this thesis. The more pronounced effects of proton irradiation can be explained when considering the mean free path of fast neutrons and protons. The former have a relatively large mean free path (about 20 cm), while the respective number for protons is

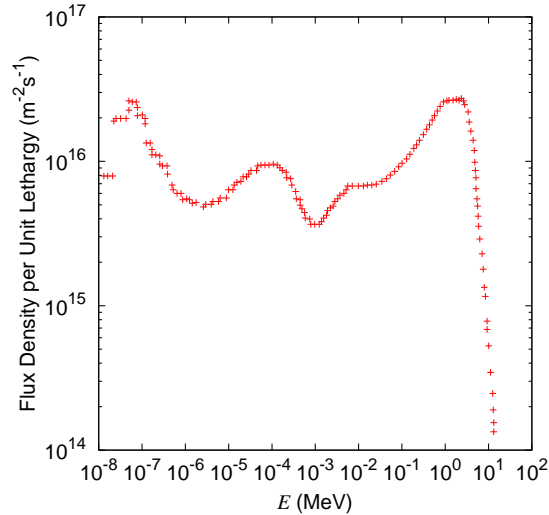


Figure 5.16: Energy dependence of the neutron fluence in the TRIGA-MARK II reactor in the Atominstitut [91]

about $50 \mu\text{m}$. Also, the interaction between protons and matter follows the well-known Bragg curve, thus almost the entire energy is transferred in a small region. The energies of the particles used in the two irradiation studies are similar. The TRIGA-MARK II reactor has a relatively broad fluence spectrum, whereby the peak for fast neutrons ($E > 0.1 \text{ MeV}$) is situated around 2 MeV (see Fig. 5.16). In the work by Nakajima et al., the protons are accelerated to an energy of 3 MeV . One more possible explanation for the large discrepancy, apart from the different interaction of fast neutrons and protons with matter, is the dependence of the T_c suppression on the doping level - the crystals analyzed in our work have the composition $\text{Ba}(\text{Fe}_{0.94}\text{Co}_{0.06})_2\text{As}_2$, while $\text{Ba}(\text{Fe}_{0.925}\text{Co}_{0.075})_2\text{As}_2$ and $\text{Ba}(\text{Fe}_{0.955}\text{Co}_{0.045})_2\text{As}_2$ are the closest chemical compositions reported by Nakajima et al. Another possible reason for the steeper drop in T_c after proton irradiation is the fact that the protons which remain in the crystal are electrically charged and act as stronger scattering centers in contrast to the electrically neutral neutrons. Thinking along these lines, the changes in the transition temperature after electron irradiation are of interest as well. The report by van der Beek et al [13] reports the suppression of T_c in Co-doped Ba-122 single crystals after irradiation with 2.5 MeV electrons, whereby the fluence is of the order of magnitude of 10^{23} m^{-2} . This number is about 100 times higher than the fast neutron fluences used in this study. The results obtained for electron irradiation show a T_c suppression of about 0.8 K . The irradiation with high-energy electrons is expected to produce point defects distributed uniformly within the sample, while defects ranging

from point-like to spherical defects with a diameter of several nanometers are expected from the irradiation with protons and neutrons. This point is probably the reason why the effects observed on the transition temperature are on a similar scale with the two other particle irradiation types despite the much larger fluence at similar energy.

A report by Kihlstrom et al [14] shows how T_c changes after irradiation with high-energy protons in a K-doped Ba-122 single crystal. Their study shows a decrease of about 0.8 K for a fluence of $7 \times 10^{20} \text{ m}^{-2}$. This number is larger than the drop $\delta T_c = 0.6$ found for fast neutron irradiation to $\Phi_t = 3.6 \times 10^{21} \text{ m}^{-2}$. This result is similar to the one obtained in the Co-doped system where Nakajima et al. also found distinctively higher decreases after proton irradiation.

A study by Tamegai et al [12] shows the effect of heavy ion (Au, Xe, U, Ni) irradiation on the transition temperature. It reveals that T_c is more strongly suppressed in comparison to the other particle irradiation techniques. This is expected since heavy ions create a correlated defect structure consisting of columnar defects. The diameter of the created defects is a few nanometers and their length ranges from 30 to 240 nm [12]. Their elongated shape and diameter close to the coherence length suggest that these defects are likely to act as strong scattering centers, explaining the stronger decrease in T_c in comparison to other particle irradiation results.

An intermaterial comparison with other superconductor classes shows that T_c does not go down as much as in cuprates ($\delta T_c \approx 0.6$ for a fluence of $1.8 \times 10^{21} \text{ m}^{-2}$ [92]), while classical superconductors such as NbTi and Nb₃Sn show a much lesser decrease [93, 94]. There are several reasons why T_c is suppressed more in cuprate-based superconductors. First of all, the Fermi surface anisotropy is larger in cuprates. What's more, the decrease in T_c is dependent on the irradiation-induced point defects which may have a higher density in cuprates due to high-mobility oxygen atoms. As regards the classical, low-temperature superconductors, the near-isotropic Fermi surface drastically reduces the effects of particle irradiation at this fluence and T_c drops only by a few hundredths of a Kelvin. At the present moment, the overwhelming opinion is that optimally doped pnictide superconductors are governed by sign-reversing s -wave ($s\pm$) [95, 96, 97, 98]. The results obtained in this study agree, at least qualitatively, with this statement since the transition temperature drops stronger in comparison to pure s -wave superconductors, while it does not drop as steeply as in d -wave superconductors (cuprates).

5.3.2 Changes in the in-plane critical current density after neutron irradiation

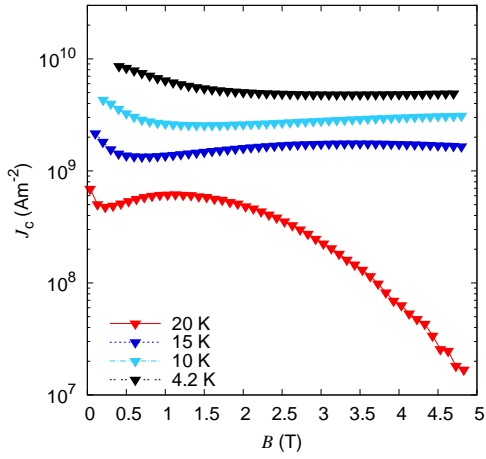
The most significant and novel result involving artificial defects resulting from fast neutron irradiation was already presented in Sec. 5.2. In addition to the angular dependence (and scaling) of J_c , it is also important to quantify the changes of the critical current in the main orientations of the single crystal, i. e. to evaluate $J_c^{ab} = J_c^{H_a \parallel c}$ as well as the two critical current components J_c^b & J_c^c which occur when $H_a \parallel ab$. This objective includes analyzing the dependence on several parameters: temperature, magnetic induction and fast neutron fluence. The following paragraphs present the case where $H_a \parallel c$, i. e. $J_c = J_c^{ab}$ for the differently doped single crystals, while the attempts to establish J_c^b & J_c^c are elaborated in the next section. The critical current density was evaluated from magnetization measurements carried out in the vector VSM.

The temperature range spanned temperatures as low as 4.2 K and as high as 32.5 K depending on T_c of the individual crystals. They were measured in the pristine state as well as after irradiation to two fluences: $1.8 \times 10^{21} \text{ m}^{-2}$ and $3.6 \times 10^{21} \text{ m}^{-2}$. As a start, the values of J_c in the pristine crystals are roughly compared to previous studies [10, 14, 99, 100]. This comparison showed good agreement between the three differently doped crystals and previous reports.

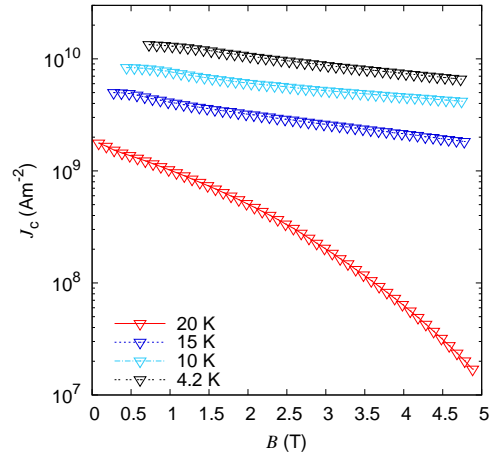
The results obtained for Co#4 are presented first. Fig. 5.17 shows a broad overview on $J_c(B, T, \Phi_t)$ as well as the enhancement factor $\frac{J_c^{\Phi_t}}{J_c^{\text{pris}}}$ at different fields and fluences.

The first three figures show how fast neutron irradiation to different fluences influences $J_c(B)$. One feature which becomes apparent immediately is the expected disappearance of the second peak in J_c . This is a confirmation that the flux line lattice is disordered at all fields, therefore no order-disorder transition takes place. The dependence of the current on B becomes less pronounced at low temperatures with increasing fluence. The rather strong drop in $J_c(T = 20 \text{ K})$ for high fields can be traced back to a lower irreversibility field at this temperature after irradiation (for details refer to the next section).

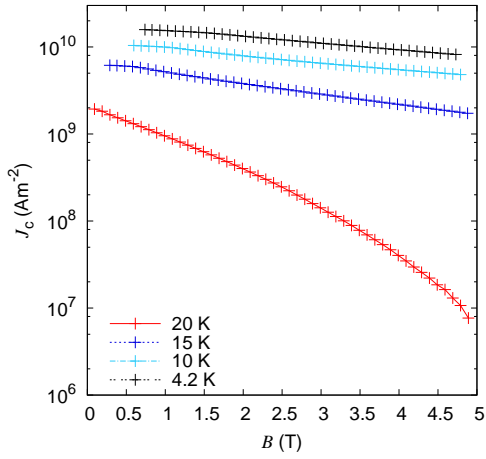
Fig. 5.17(d) shows the temperature dependence of J_c at two different fields and fluences. This plot is very useful as means of direct comparison between the changes after each irradiation step. Red denotes $B = 1.5 \text{ T}$ and black- $B = 4 \text{ T}$. The different symbols refer to the the crystal either in the pristine state, or after the first or second irradiation step. Starting with the behavior of the pristine crystal (solid circles), J_c decreases with



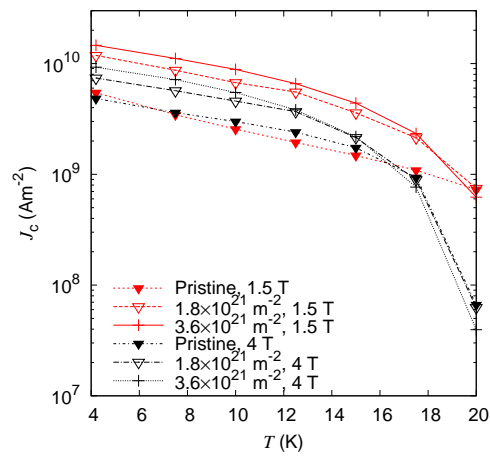
(a) Pristine Co-doped Ba-122



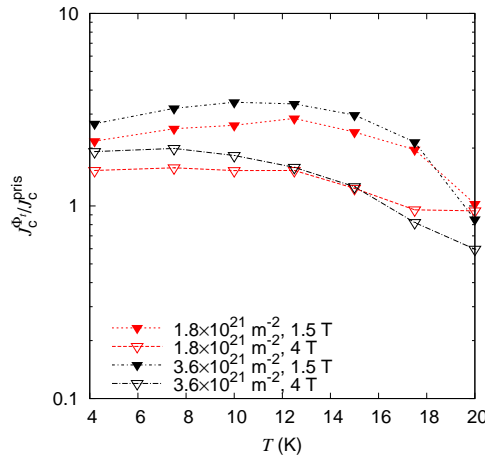
(b) Co-doped Ba-122 irradiated to $1.8 \times 10^{21} \text{ m}^{-2}$



(c) Co-doped Ba-122 irradiated to $3.6 \times 10^{21} \text{ m}^{-2}$



(d) $J_c(T, B, \Phi_t)$



(e) J_c enhancement

Figure 5.17: J_c in a Co-doped Ba-122 single crystal pristine and after irradiation to different fast neutron fluences

increasing temperature as expected. The presence of the second peak in J_c is the reason why $J_c(T, 1.5 \text{ T}) \leq J_c(T, 4 \text{ T})$ for $7.5 \leq T \leq 15 \text{ K}$.

Following the first irradiation step, J_c (open symbols) increases as a result of the additional artificial pinning centers for almost all temperatures. It is also distinctively different at the two fields, with $J_c(T, 1.5 \text{ T}) > J_c(T, 4 \text{ T})$ at all temperatures. This behavior is expected since the second peak is no longer present and a monotonic $J_c(B)$ behavior is observed in Fig. 5.17(b). It is worth noting that the very last data point, at 20 K, is basically the same as in the pristine crystal. This is a result of a combination of factors: On one hand, pinning is stronger in the irradiated sample, but on the other hand T_c is decreased. At this temperature and for both fields, the two effects more or less cancel each other out, leading to similar J_c values prior and after the first irradiation step.

Next, the total fast neutron fluence is increased to $3.6 \times 10^{21} \text{ m}^{-2}$ (crosses). Once again, the critical current rises as the density of pinning sites increases. However, the increase is obviously not as strong as after the first irradiation, while at temperatures $\geq 17.5 \text{ K}$ the 4 T data is lower than in both the pristine state and after the first irradiation. The latter shows the effect of the further drop in T_c and likely B_c . In particular, the critical current decreases strongly at 20 K where B_{irr} drops from approximately 7 T in the pristine state to about 6 T after the second irradiation step (see Sec. 5.3.4 for detailed analysis of the change in B_{irr} with increasing fast neutron fluence).

A quantitative analysis of the respective J_c enhancements is possible with help of Fig. 5.17(e). The rise in the critical current density is more substantial at 1.5 T. The results at this field will be discussed first. The special case of $T = 20 \text{ K}$ was already explained in detail in connection with the dependence of J_c on T and will not be elaborated upon further. The critical current is increased by about 2-2.5 times for $T < 20 \text{ K}$ after the first irradiation step. As regards the second irradiation step, the enhancement in comparison to the pristine crystal is between 2-3.3 times. As for the higher field (4 T), the observed factors are above 1 only for $T < 17.5 \text{ K}$ for both irradiation steps. At $\Phi_t = 1.8 \times 10^{21} \text{ m}^{-2}$, the maximum enhancement factor is 1.6 ($T = 7.5 \text{ K}$), while at $\Phi_t = 3.6 \times 10^{21} \text{ m}^{-2}$ the respective value is 2 (also at $T = 7.5 \text{ K}$). A careful look at the curves reveals an interesting trend: The increase of the critical current density does not follow a linear dependence on the fluence. This effect has been observed previously

in fast neutron irradiated $\text{YBa}_2\text{Cu}_3\text{O}_{7-\delta}$ single crystals [92]. The explanation provided by Sauerzopf et al. is that the defects grow larger with increasing fluence while also becoming too dense to act as effective pinning centers for the flux line lattice.

The maximum critical current density in the Co-doped crystal, obtained at $B_{\text{sf}} \approx 0.75$ T, $T = 4.2$ K and $\Phi_t = 3.6 \times 10^{21}$ m⁻², amounted to about 1.6×10^{10} Am⁻². It is interesting to compare this number with the expected depairing current density for this compound as means to calculate the effective pinning parameter η_{pin} . Both of these parameters will be determined and presented in a table for all three crystal types later in the section to allow an easier comparison between the individual doping types.

The next crystal is P#1. There were no significant differences from the measurement procedure used for Co#4. Due to the higher transition temperature in P#1, magnetization loops were carried out at two additional temperatures (22.5 and 25 K). The evaluated critical current density as a function of the magnetic induction in the pristine state and for the two irradiation steps is presented in Figs. 5.18(a)- 5.18(c). The pristine crystal shows similar characteristics as the Co-doped one as far as a second peak in J_c is concerned. The magnitude of the critical current is clearly lower in comparison to the pristine Co#4 for medium and high temperatures ($T \geq 15$ K). This is probably due to a less pronounced pinning in this crystal since $B_{\text{irr}}^{\text{P\#1}}(T) > B_{\text{irr}}^{\text{Co\#4}}$ (details available in Sec. 5.3.4). The fast neutron irradiation eradicates the second peak here as well, but it becomes immediately apparent that the increase in J_c is distinctively larger than in Co#4. This is in part due to the lower values of the critical current density in the pristine P#1 in comparison to the pristine Co#4. Additionally, J_c in the irradiated P#1 reaches higher values when compared to Co#4.

There are no significant differences from Co#4 when taking a look at the temperature dependence of J_c (see Fig. 5.18(d)). Particularly the results after irradiation are very similar in form to the ones obtained for the Co-doped crystal. This is a result from the nearly identical pinning landscape created by the fast neutrons in the two differently doped single crystals. The $J_c(T)$ in the pristine state shows a non-monotonic behavior which is due to the fishtail effect and the changes in the onset field B_{onset} with temperature. B_{onset} is defined as the field where the order-disorder transition of the flux line lattice begins. It is evaluated from the m_+ branch of the magnetization curves. Two straight lines are necessary to evaluate B_{onset} . One is fitted through the region about 0.1 T prior

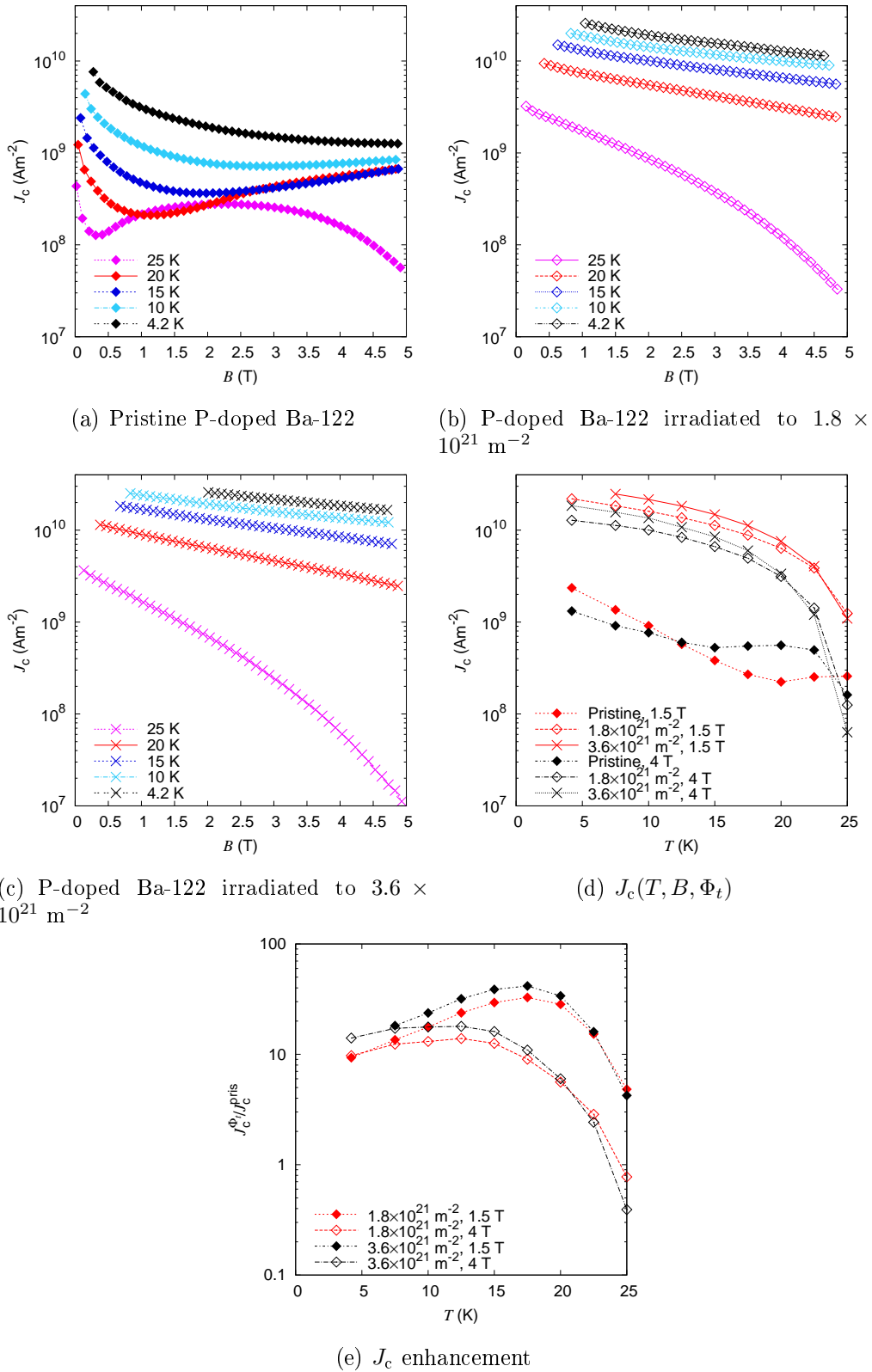


Figure 5.18: J_c in a P-doped Ba-122 single crystal pristine and after irradiation to different fast neutron fluences

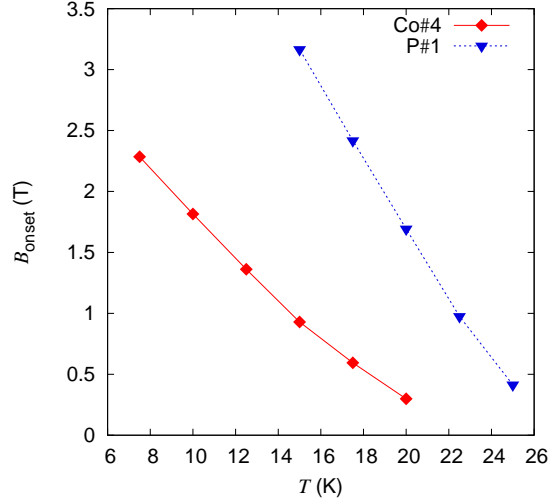


Figure 5.19: B_{onset} of the pristine Co- and P-doped crystals

to the local minimum after which the critical current density starts rising again. The second line is fitted through the steepest region of the subsequent increase of the critical current as the order-disorder transition takes place. The crossing point of the two lines is defined as B_{onset} . Fig. 5.19 shows the onset field for both Co#4 and P#1. Due to the higher B_{onset} and more pronounced fish-tail in the pristine P-doped crystal, $J_c(17.5\text{K} \leq T \leq 22.5\text{K}, 4\text{ T})$ is larger by a factor of about 2.5 than $J_c(17.5\text{K} \leq T \leq 22.5\text{K}, 1.5\text{ T})$. By contrast, even though the tendency is observed in the pristine Co-doped crystal as well, the difference between the critical current density is not as large (about 20%).

The enhancement factor in P#1 is plotted in Fig. 5.18(e). The difference in magnitude with the Co-doped crystal is now clearer: At 1.5 T, a maximum enhancement of above 40 times the original current is achieved at $\Phi_t = 3.6 \times 10^{21}\text{ m}^{-2}$ at 17.5 K. It is important to note that the presence of the second peak in the pristine sample causes much lesser enhancements for most temperatures at 4 T since the flux line lattice is already either partially ($10\text{ K} < T < 25\text{ K}$) or entirely ($T = 25\text{ K}$) disordered in the pristine state. Also, the factor is nearly identical for both fields at low temperatures as is expected when $B_{\text{onset}} > 4\text{ T}$. The lesser increase after the second irradiation is once again observed. Another feature observed in both crystals is the crossover at high temperatures ($T \geq 22.5\text{ K}$ for P#1): The critical current enhancement is stronger for the lower fluence.

The maximum in-plane critical current density achieved at 4.2 K is about $3 \times 10^{10}\text{ Am}^{-2}$. This number is about twice as high as the maximum critical current density in the Co-doped crystal which was established at the same temperature.

The final crystal (K#5) is also the most interesting one. The measurements for the pristine crystal and after the first irradiation were carried out in the VSM, similarly to the previous two crystals. However, due to the extremely high currents and the geometry of the crystal, it was impossible to fully magnetize it after the second irradiation step at low temperature with the 5 T magnet of the VSM, even when using field-cooling. The 7 T SQUID represented a viable exit strategy. However, another problem emerged, namely flux jumps at $T \leq 15$ K (see Sec. 4.1.2 and Fig. 4.3). This effect makes the evaluation of J_c at low temperatures very difficult. The situation was compounded by an apparent drop in the magnetic moment between consecutive measurements in the SQUID and the VSM. The signal decreased by about 30% (see Fig. 5.20), which led to fears that the crystal was compromised. There are two possible reasons for such a decrease: a drop in J_c , or a mechanical splitting of the crystal which would deform the current loops, thus changing the measured magnetic moment. A close observation of the crystal via optical microscope revealed a deep chasm in the crystal which ran almost diagonally across it. This was identified as the reason for the decrease in m since the current couldn't pass through the chasm, thus the loops were deformed. This case was the 'lesser evil', so to speak, because it was possible to cut out a small, cuboidal piece out of the large single crystal which would then be used for magnetization measurements. This small piece is K#5₁ and it allowed the evaluation of $J_c(\Phi_t = 3.6 \times 10^{21} \text{ m}^{-2})$ via RSO magnetization loops in the 7 T SQUID. Its transition temperature was basically identical with the one of the original K#5, as expected. In addition, the smaller size of the crystal helped prevent flux jumps since less total flux has to be pinned in the crystal. The larger remaining part of K#5 was used for resistive measurements. A part of the chasm was still clearly visible on the larger part of the original K#5.

K#5 showed remarkably high J_c after fast neutron irradiation, while the currents were rather low in the pristine state in comparison to the other two doping types. The latter result was already discussed in detail in Sec. 5.2. The introduction of artificial pinning centers and the transition to strong pinning result in drastic increases in J_c (see Fig. 5.21(a) - 5.21(c)). Note that the three figures do NOT cover the same range in J_c since the current changes so dramatically after irradiation. Interestingly, a small second peak appears after the first irradiation step and is also visible after the second one. Taking a look at the temperature dependence of the critical current in Fig. 5.21(d), one finds the

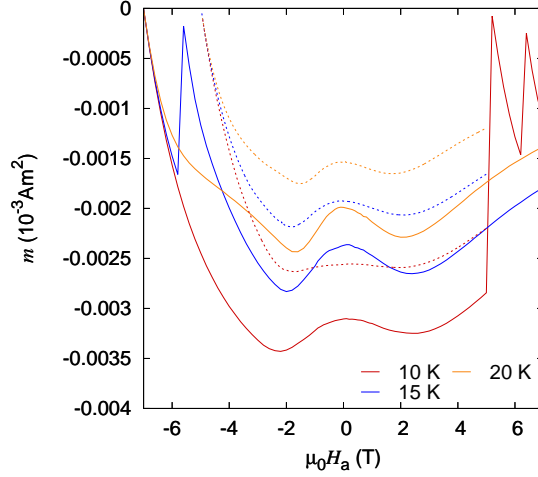
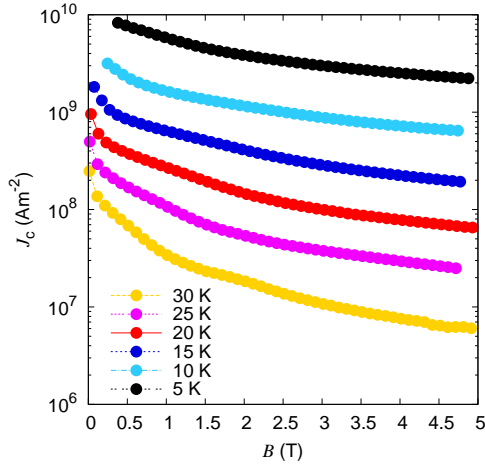


Figure 5.20: Difference in the magnetic moment in two subsequent magnetization measurements in the SQUID (solid line) and in the VSM (dotted line)

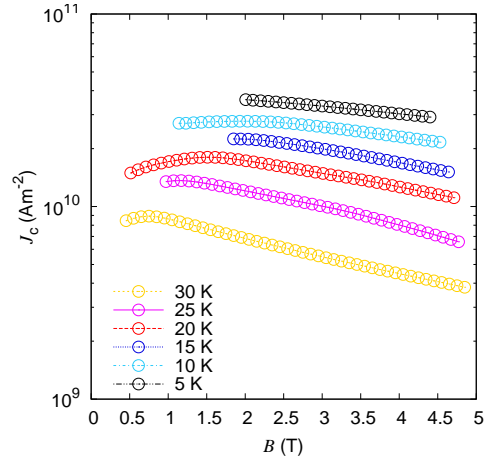
already familiar curve shapes after irradiation, despite the distinctively different behavior in the pristine state. This is one further confirmation that the introduced pinning centers control the pinning properties and in turn the critical current density of all single crystals, regardless of their doping.

The enhancement factor in the K-doped crystal reaches values up to almost 1000 at 4 T and high temperatures. This is thoroughly in line with the finding that weak pinning by point-like defects (ineffective at high temperatures and fields) dominates in the pristine state. This also explains why the current is enhanced more in the K-doped crystal (weak pinning, no fishtail in the pristine state) as compared to the other two crystals (higher J_c , fishtail in the pristine state). Moreover, the previously observed feature of a weaker-than-linear increase in the enhancement factor with the fluence steps used in this work is even more pronounced in this case.

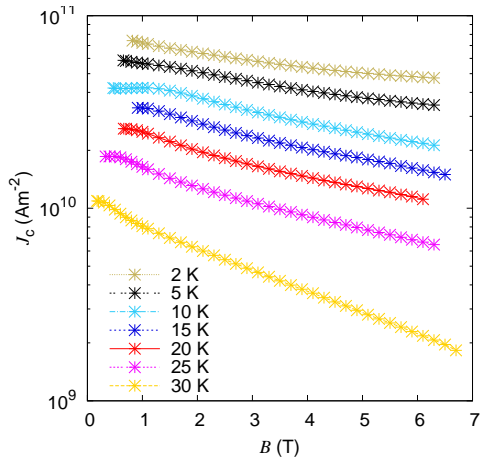
The highest current reached in K#5₁ was about $7.4 \times 10^{10} \text{ Am}^{-2}$ at 2 K and a self-field of slightly over 0.8 T. To the knowledge of the author, this is the highest current obtained in a Ba-122 based single crystal. A recent report by Kihlstrom et al [14] includes a study on the influence of spherical artificial defects created by proton irradiation. The values of J_c obtained after neutron irradiation are higher than the ones acquired after proton irradiation. For instance, at 1 T and 5 K, J_c is about $5.2 \times 10^{10} \text{ Am}^{-2}$ in the latter case, while it eclipses $5.6 \times 10^{10} \text{ Am}^{-2}$ in the former. At the same temperature but higher fields (6 T), the respective numbers are $\approx 3 \times 10^{10} \text{ Am}^{-2}$ and $\approx 3.5 \times 10^{10} \text{ Am}^{-2}$. A comparison



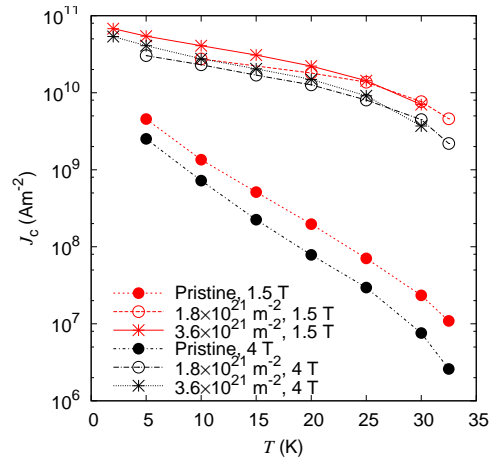
(a) Pristine K-doped Ba-122



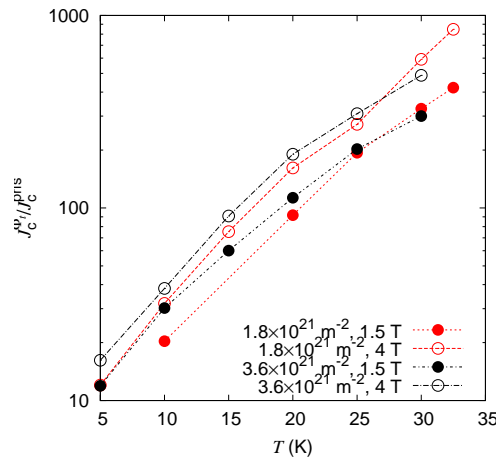
(b) K-doped Ba-122 irradiated to $1.8 \times 10^{21} \text{ m}^{-2}$



(c) K-doped Ba-122 irradiated to $3.6 \times 10^{21} \text{ m}^{-2}$



(d) $J_c(T, B, \Phi_t)$



(e) J_c enhancement

Figure 5.21: J_c in a K-doped Ba-122 single crystal pristine and after irradiation to different fast neutron fluences

at higher 30 K and 0.2 T returns $0.92 \times 10^{10} \text{ Am}^{-2}$ for proton and $1.09 \times 10^{10} \text{ Am}^{-2}$ for fast neutron irradiation. At high fields, the values are $0.3 \times 10^{10} \text{ Am}^{-2}$ and $0.37 \times 10^{10} \text{ Am}^{-2}$ respectively. The favorable comparison shows that the higher potential in terms of critical current density of the crystal analyzed in this work when similar defect structures are considered.

A further point which should be discussed are the fluence dependencies of J_c in the cases of proton and neutron irradiation. In Kihlstrom's paper, the crystal was irradiated with high energy ($E = 4 \text{ MeV}$) protons thrice: $\Phi_t^{1,2,3} = 1 \times 10^{20} \text{ m}^{-2}$, $4 \times 10^{20} \text{ m}^{-2}$, and $7 \times 10^{20} \text{ m}^{-2}$. It is important to elaborate upon the enhancement factor of the critical current at each irradiation step. Please note that in this paragraph the enhancement is not expressed as a normalization to the current density in the pristine state. Here it is more advantageous to analyze the changes from each irradiation step to the next one. Kihlstrom et al report that at $T = 5 \text{ K}$, the current increases about 2.3 times at 0 T (presumably self-field measurement) and about 5 times at 4 T for $\Phi_t = 1 \times 10^{20} \text{ m}^{-2}$. After the second irradiation step, with $\Phi_t = 4 \times 10^{20} \text{ m}^{-2}$, the numbers read 1.7 and 2.3 respectively. At the third and final total fluence of $\Phi_t = 7 \times 10^{20} \text{ m}^{-2}$, the enhancement is distinctively lower: 1.07 and 1.23, respectively. The modest increase when comparing J_c at the last two irradiation steps indicates that the potential for J_c enhancement by using only proton irradiation has been nearly saturated. Next, the data for the fast neutron irradiated crystal for $T = 5 \text{ K}$ is analyzed. Following the initial irradiation to a fluence of $1.8 \times 10^{21} \text{ m}^{-2}$, the current increases 9.4 times at $B = 2 \text{ T}$ (lower field data unavailable for $\Phi_t = 1.8 \times 10^{21} \text{ m}^{-2}$) and 12.1 times at $B = 4 \text{ T}$. The enhancement of J_c after Φ_t is incremented from $1.8 \times 10^{21} \text{ m}^{-2}$ to $3.6 \times 10^{21} \text{ m}^{-2}$ is about 1.4 times for $B = 2 \text{ T}$ and about 1.35 for $B = 4 \text{ T}$. While the increase in J_c is not as drastic as after the first irradiation step, the numbers suggest that there is still a more pronounced potential for improving the critical current density merely by increasing the total neutron fluence.

To see where the highest obtained J_c ranks among all of the iron-based materials, a comparison is made to the record value reported by [101]. The study by Fang et al reports J_c in a Sm-1111 with columnar defects. The maximum critical current density reaches almost $2 \times 10^{11} \text{ Am}^{-2}$ at zero applied field and 5 K. Since the self-field of the neutron irradiated K-doped crystal at 5 K is almost 1 T, a comparison at this field is more sensible. The Sm-1111 sample has a critical current density of $\approx 1.2 \times 10^{11} \text{ Am}^{-2}$

| Sample | ξ (nm) | λ (nm) | J_d (10^{11}Am^{-2}) | η_{pin} (%) |
|--|--------------|----------------|-----------------------------------|-------------------------|
| $\text{Ba}(\text{Fe}_{0.94}\text{Co}_{0.06})_2\text{As}_2$ | 2.7 [8, 102] | 200 [103] | 9.3 | 2.1 |
| $\text{BaFe}_2(\text{As}_{0.7}\text{P}_{0.3})_2$ | 2.14 [104] | 300 [105] | 5.2 | 7.2 |
| $\text{Ba}_{0.6}\text{K}_{0.4}\text{Fe}_2\text{As}_2$ | 1.88 [6] | 180 [106] | 16.6 | 5.1 |

Table 5.2: Depairing current density and effective pinning parameter of the differently doped single crystals

as compared to $\approx 5.3 \times 10^{11} \text{ Am}^{-2}$ in the K#5₁. The factor of above two distinguishes the 1111 crystal as the clear winner, but it should not be forgotten that the columnar defect structure is much more effective for achieving stronger pinning than the spherical defects produced by fast neutron irradiation. As already shown by Kihlstrom et al, a composite defect structure consisting of both columnar and spherical defects results in excellent pinning properties and a very rigid $J_c(B)$ behavior.

The previous paragraphs presented the dependence of the in-plane critical density on temperature, magnetic flux and doping. As already mentioned earlier, a good tool for evaluating the efficiency of the pinning structure as well as for establishing the theoretically attainable J_c is the depairing current density J_d (see Eq. 2.12). The equation already shows the parameters which are necessary for the calculation of the latter, namely $\lambda(0 \text{ K})$ and $\xi(0 \text{ K})$. These figures can be obtained from literature. The following table shows the coherence length, penetration depth, J_d and the effective pinning parameter $\eta_{\text{pin}} = \frac{J_c(0 \text{ K}, B_{\text{sf}})}{J_d}$. $J_c(0 \text{ K}, B_{\text{sf}})$ is extrapolated from the available data for $\Phi_t = 3.6 \times 10^{21} \text{ m}^{-2}$. Note that since the table shows data obtained for $H_a \parallel c$, the coherence length and penetration depth here correspond to $\xi_{ab}(0 \text{ K})$ and $\lambda_{ab}(0 \text{ K})$.

The table reveals that the the K-doped system has the highest potential in terms of J_d : $16.6 \times 10^{11} \text{ Am}^{-2}$. The values obtained for η_{pin} are in the order of magnitude of several percent for all crystals, while the highest attainable η_{pin} is 20% and requires a pinning structure consisting of line defects which pin the whole length of the individual flux lines. Since fast neutrons produce defects with various radii, ranging from point-like to ones with a radius of several nanometers, it pins only parts of the flux line, thus η_{pin} cannot reach its theoretical maximum. Still, it is important to note that the K-doped system has a very high J_d , which shows its potential for applications. Even if η_{pin} is only about 5% as is the case in this study, the critical current density eclipses $5 \times 10^{10} \text{ Am}^{-2}$ at 5 K and 1 T. If the theoretical maximum of J_c is reached, the extrapolated critical

current density at 0 K would be above $3.5 \times 10^{11} \text{ Am}^{-2}$. Combined with its relatively cheap production costs, this makes the material an intriguing option for applications, at least from the perspective of its intrinsic properties. The best wires based on pnictide superconductors use K-doped Ba-122 [9].

5.3.3 The J_c -anisotropy conundrum for $H_a \parallel ab$

Ideally, one would like to measure the critical current density at $H_a \parallel ab$ as well. By contrast to the case where $H_a \parallel c$ ($J_c^a = J_c^b = J_c^{ab}$), the situation is not quite so simple here. The problem comes from the emergence of the so-called c -currents (J_c^c), i. e. currents which are normal to the ab -planes and by definition parallel to the c -axis. Typically, these currents are lower than the current flowing along the Fe-As planes. This means that a proper evaluation of a measurement where $H_a \parallel ab$ involves applying the anisotropic Bean model (see Sec. 2.2). The procedure requires two individual measurements, with $H_a \parallel a$ and $H_a \parallel b$, respectively (note that here a and b denote the geometric sides of the crystal). From these measurements, it is possible to separate the two components of the critical current density, J_c^c and J_c^b , by using Eq. 2.10 and 2.11.

The experiments were carried out on pristine crystals from all three systems, as well as on an irradiated Co-doped crystal. However, the obtained results showed large discrepancies with previously reported values for J_c^c . The magnitude of J_c^c was distinctively lower in comparison to prior studies. The most glaring example being the K-doped system where $J_c^c \approx 0.03J_c^b$ [107]. Even though a microscopic study would be necessary to determine the exact reason for the small J_c^c , it is possible to formulate one factor which strongly reduce this component of the critical current density. It is conceivable that there are badly connected planes within the crystal which impede the current flow. The results of the experiments will not be elaborated upon in detail, but are available in the master thesis of David Fischer [107] which was co-supervised by the author of this PhD thesis. One very important detail has to be mentioned, though. Despite the fact the obvious discrepancies between the measured J_c^c and previously reported values, this does not concern the in-plane current density and the angular anisotropy of J_c which were discussed in prior sections.

5.3.4 Upper critical fields, irreversibility lines and coherence lengths

Having examined in detail the critical current density, its angular anisotropy and changes with fast neutron irradiation, it is time to tackle the upper critical field in the differently doped crystals. The measurement procedure was already presented in Sec. 4.2.2. Each crystal is measured in the two main orientations: $H_a \parallel ab$ and $H_a \parallel c$. This is necessary due to the anisotropy of the upper critical field in the Ba-122 compounds. The transport current used for the resistive measurements flows steadily along the ab -planes. The adapter used for the experiment had multiple advantages as pointed out in Sec. 4.2.2, but also one drawback. The high ductility of indium allows good electrical connectivity, but also means that it is difficult to calculate the exact distance between the voltage contacts after the crystal had been pressed onto the In pads. The result is that it is nearly impossible to evaluate the absolute value of the resistivity ρ from

$$R(T) = \frac{U(T)}{I} = \rho(T) \frac{l}{A} \Rightarrow \rho(T) = \frac{U(T)A}{Il} \quad (5.7)$$

where U is the voltage drop, I is the constant transport current (typically a few mA), A is the cross-section of the superconductor and l is the distance between the voltage contacts. l is typically in between 200 and 500 μm . It is unfortunate that the absolute value of ρ cannot be calculated, but it is still possible to evaluate the residual resistivity ratio (RRR) = $\frac{\rho(300\text{ K})}{\rho_{\text{t}}}$ where ρ_{t} is the resistivity a few Kelvin prior to the transition into the superconducting state. The only assumption necessary to justify the calculation of RRR is that l remains constant as the crystal is being cooled down. The crystal is pressed strongly onto the indium pads by a second resin plate which is tightened by brass screws, therefore any further deforming of the indium contacts is highly unlikely in most cases. The exception to this rule are the cases when the brass screws are not tightened properly. During the course of the experiments, this occurred twice and prevented the evaluation of the RRR in the respective case (Co#4 and P#1 at $\Phi_t = 3.6 \times 10^{21} \text{ m}^{-2}$).

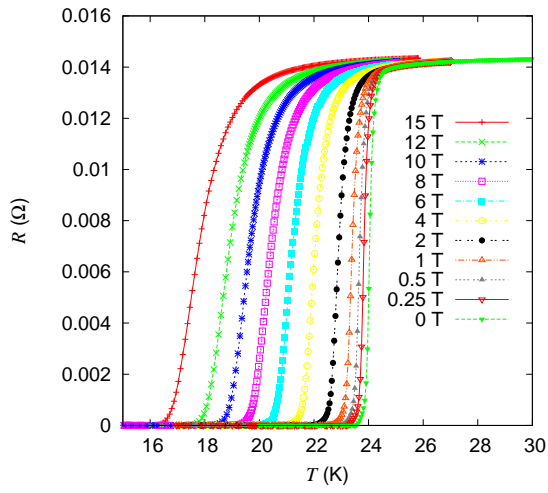
Another difficulty posed by the non-determinable distance l is the evaluation of the irreversibility line B_{irr} , also known as the IL. It involves an electric field criterion, thus the gap between the voltage leads is needed for the calculation of the respective voltage criterion from $E_{\text{cr}} = 1\mu\text{V}/\text{cm}$. However, this is only a minor difficulty as a result of the sharp fall of U in the voltage region of interest (between 20 nV and 50 nV). The

transport current in these measurements is either 1 or 5 mA, depending on the crystal geometry, allowing a calculation of the $R = U/I \approx 10^{-5}\Omega$. The fall of U (and of R , consequently) is steep in this region, therefore it is possible to use an average distance of 300 μm (as controlled for each crystal via optical microscope) in most cases when evaluating B_{irr} . In the rare case that the contacts are much closer to each other than usual, a nominal distance of 100 μm is used for the calculation of the voltage criterion (Co#4 for $\Phi_t = 3.6 \times 10^{21} \text{ m}^{-2}$ and $H_a \parallel c$).

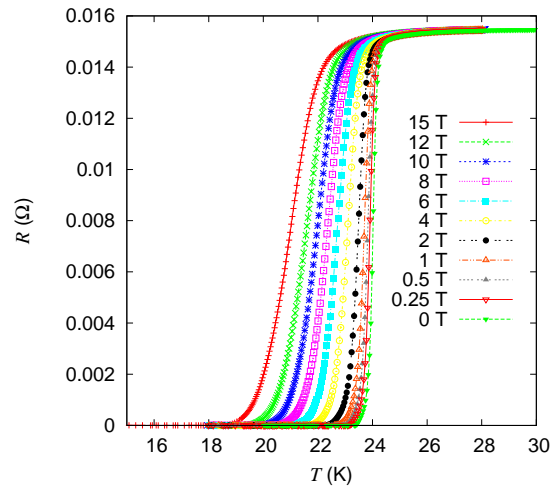
The resistive transitions in the pristine crystals (Co#1,P#2,K#4) are shown in Fig. 5.22. All three crystal types show clear superconducting transitions to zero resistivity. Please note that the irradiated crystals measured (Co#4,P#1,K#5) are not the same samples as the pristine ones, but they originated from the same respective synthesis batches and showed very similar basic properties (T_c and J_c^{ab}). The transitions after each irradiation step ($\Phi_t = 1.8 \times 10^{21} \text{ m}^{-2}$ and $\Phi_t = 3.6 \times 10^{21} \text{ m}^{-2}$) are shown in Figs. 5.23 and 5.24.

The curves allow the extraction of RRR (together with measurements at room temperature), $B_{c2}^{c,ab}$ and $B_{\text{irr}}^{c,ab}$. Tab. 5.3 lists the RRRs for the pristine and the irradiated crystals. The dopant dependence of RRR is evident, with a lower value indicating larger impurity scattering. The ranking of the crystals with respect to their respective RRRs matches well with the differences in the transition temperature widths and critical current densities. As already mentioned, the lower the RRR the more scattering centers are present in the superconductor, which automatically means higher density of potential pinning centers and higher ΔT_c . We observe only minor differences in the range of a few percent after the first irradiation. The small decreases for the Co- and P-doped systems can be explained by additional scattering centers resulting from the irradiation. The RRR rises very slightly in the K-doped system, which is an unexpected result. However, the magnitude of the changes is so small that it is difficult to determine whether they are caused by the irradiation or due to very slight differences in the doping level of the pristine and irradiated single crystals.

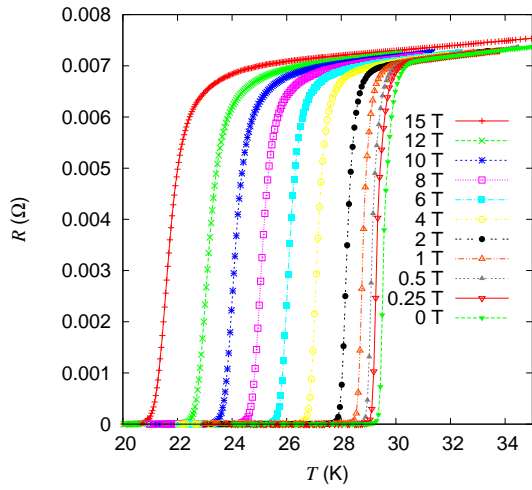
After the second irradiation step, the fluence is increased to $\Phi_t = 3.6 \times 10^{21} \text{ m}^{-2}$. It was already mentioned that the RRR could not be established for Co#4 and P#1 due to experimental deficiencies. The RRR established for K#5 after the second irradiation showed a very large drop from the value in the pristine state and after the first irradiation. This could be due to a combination of the mechanical damage sustained by the crystal



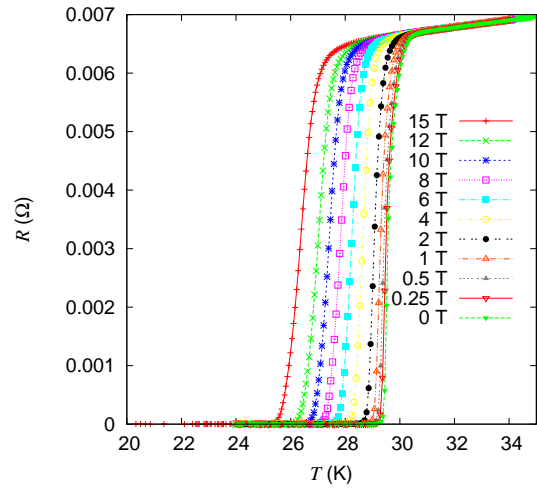
(a) Co-doped, $H_a \parallel c$



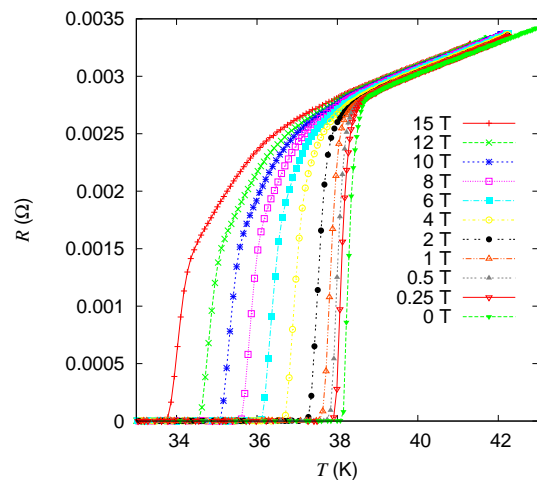
(b) Co-doped, $H_a \parallel ab$



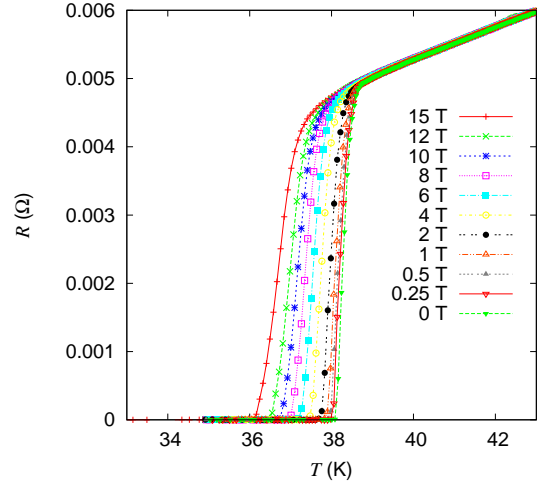
(c) P-doped, $H_a \parallel c$



(d) P-doped, $H_a \parallel ab$

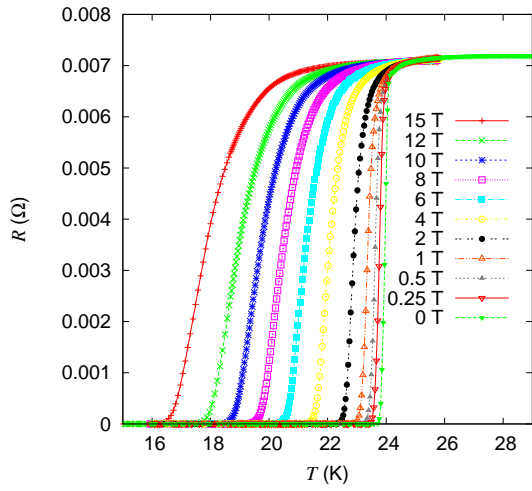


(e) K-doped, $H_a \parallel c$

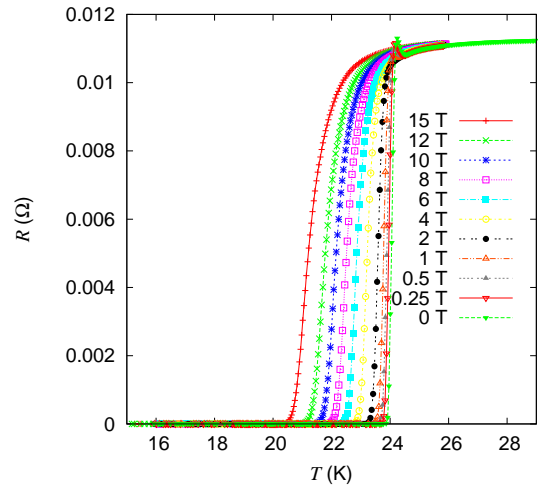


(f) K-doped, $H_a \parallel ab$

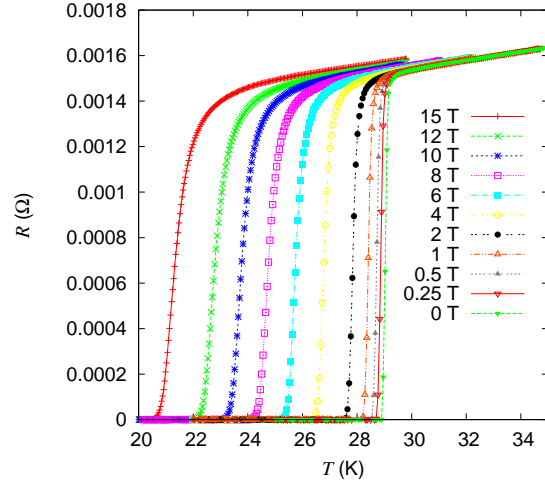
Figure 5.22: Resistive transitions for the three crystal types in the pristine state



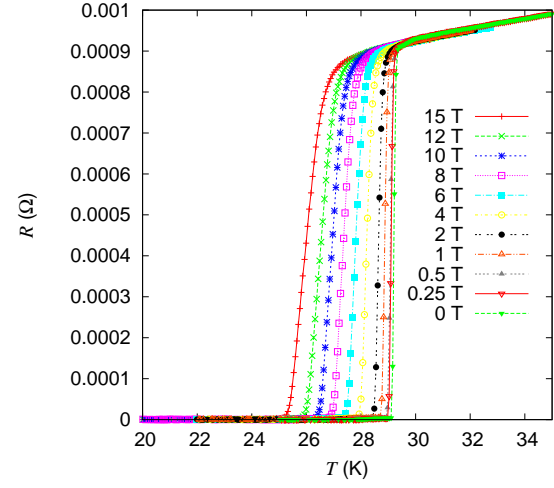
(a) Co-doped, $H_a \parallel c$



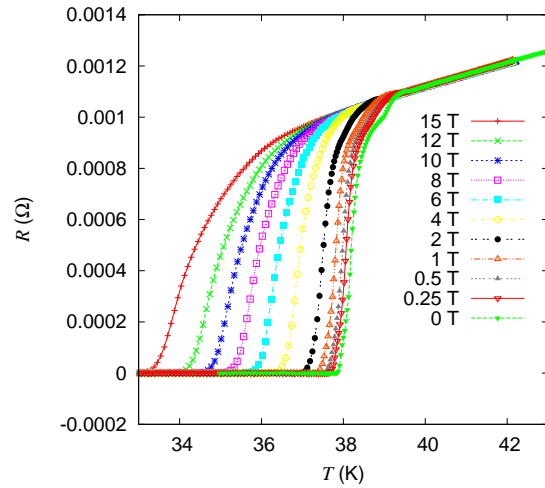
(b) Co-doped, $H_a \parallel ab$



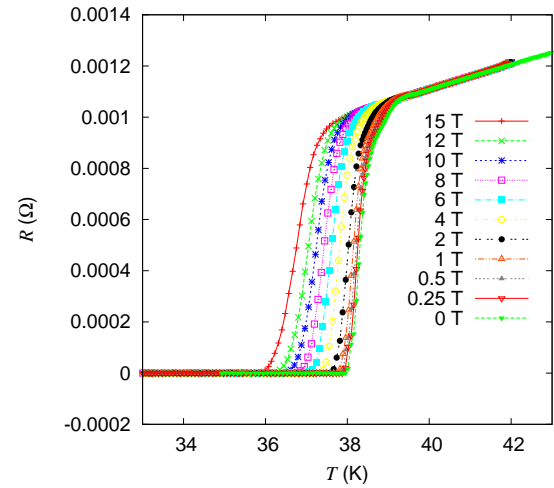
(c) P-doped, $H_a \parallel c$



(d) P-doped, $H_a \parallel ab$

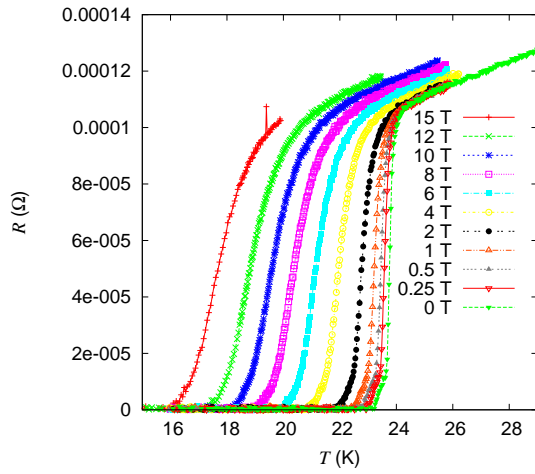


(e) K-doped, $H_a \parallel c$

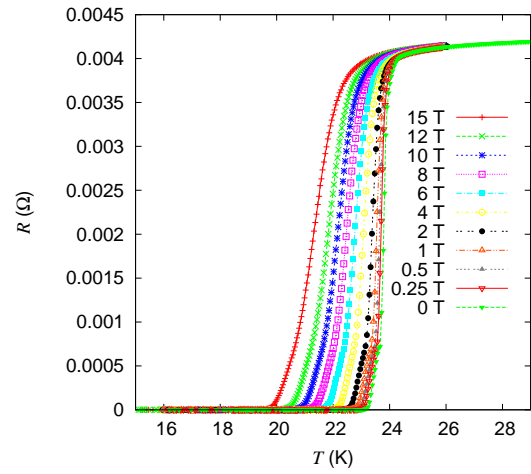


(f) K-doped, $H_a \parallel ab$

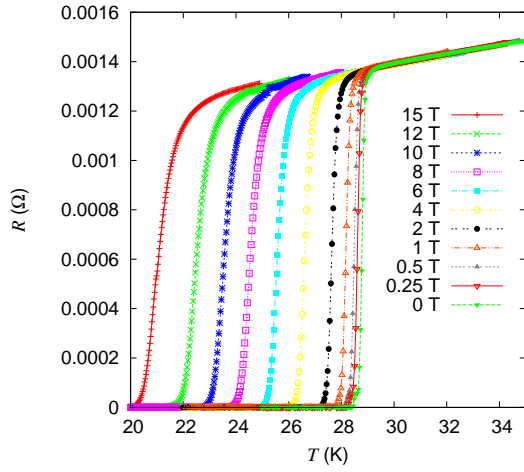
Figure 5.23: Resistive transitions for the three crystal types after irradiation to $\Phi_t = 1.8 \times 10^{21} \text{ m}^{-2}$



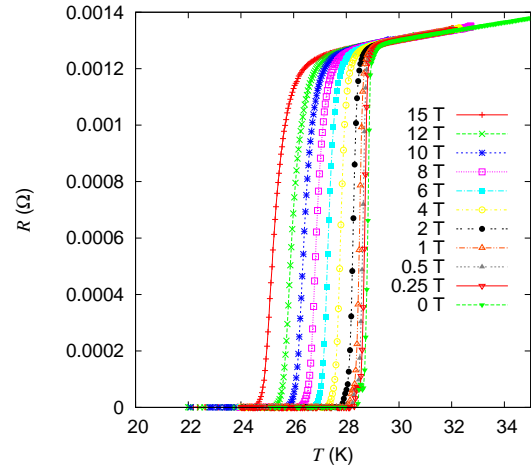
(a) Co-doped, $H_a \parallel c$



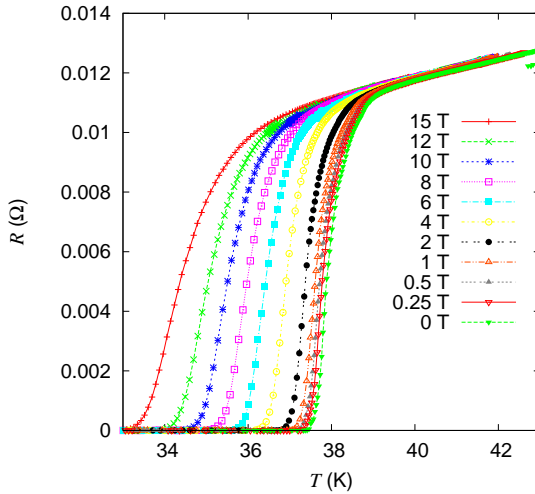
(b) Co-doped, $H_a \parallel ab$



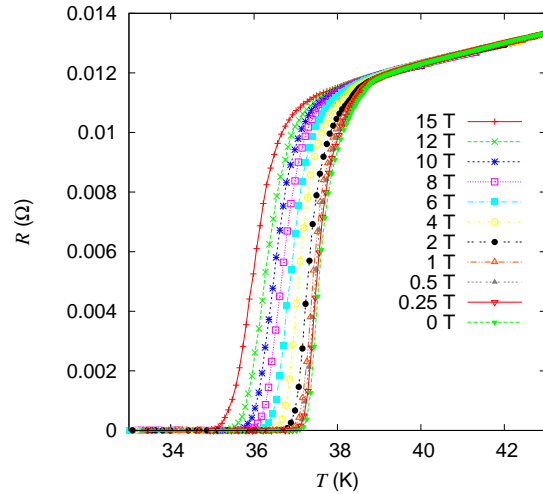
(c) P-doped, $H_a \parallel c$



(d) P-doped, $H_a \parallel ab$



(e) K-doped, $H_a \parallel c$



(f) K-doped, $H_a \parallel ab$

Figure 5.24: Resistive transitions for the three crystal types after irradiation to $\Phi_t = 3.6 \times 10^{21} \text{ m}^{-2}$

| Dopant | RRR_{pris} | $RRR_{\Phi_t=1.8 \times 10^{21} \text{ m}^{-2}}$ | $RRR_{\Phi_t=3.6 \times 10^{21} \text{ m}^{-2}}$ | $T(\text{ K})$ |
|--------|---------------------|--|--|----------------|
| Co | 1.86 | 1.76 | - | 26 |
| P | 4.16 | 3.92 | - | 33 |
| K | 10.2 | 10.5 | 5 | 42 |

Table 5.3: Resistivity ratios of the pristine and irradiated crystals

(chasm) during the magnetization measurements, while the surface of the crystal was not in good condition after the second irradiation as well. In fact, the two large sides of all crystals (Co#4, P#1, K#5) were so degraded that the contact resistance amounted to hundreds of Ohm. This necessitated a thorough cleaning. Using the chemical solvent xylol is advantageous since experiments in the 1 T SQUID showed it has no effect on the shielded volume fraction or T_c of a pristine K-doped crystal, leading to the conclusion that it is safe to use on the samples in question. Unfortunately, the surface of the crystals was still clearly passivated even after the thorough cleaning with xylol. This left only one option-mechanically removing the upper-most layers of each crystal. This was a painstaking assignment since these are irradiated samples which means extra care has to be taken to avoid any contamination of the working place. The selected tool was a scalpel (edge thickness of about several micrometers). The edge was immersed into vacuum grease so as to avoid any dust spreading during the cleaning of the crystals. Each crystal was placed under an optical microscope and 5 to 10 micrometers were removed from one of its large surfaces. Only one side was treated per sample in order placing electrical contacts on it. Although great care was taken not to exert too much force while removing the passivated layers from the crystals, it is conceivable that the cleaning procedure resulted in a deterioration of the crystals. For instance the small tail-like effects visible in the resistive transitions of Co#4 (Figs. 5.24(a) and 5.24(b)) and P#1 (Figs. 5.24(c) and 5.24(d)) might be caused by the preparation of the crystals' surfaces.

Due to the very high B_{c2} values in the Ba-122 system (B_{c2}^{ab} up to over 100 T for K-doped crystals [6]) and the limit of the applied field (15 T), the upper critical field is obtained only in a limited temperature range. Fig. 5.25 shows B_{c2}^{ab} and B_{c2}^c as well as the respective irreversibility lines of all three crystal types in the pristine state and after each of the two irradiation steps. When linking Figs. 5.17(d), 5.18(d), 5.21(d) to Figs. 5.25(a), 5.25(d) and 5.25(g), it becomes apparent that the significantly higher values of B_{c2}^c and B_{irr}^c in the P- and K-doped pristine crystals do not translate to a

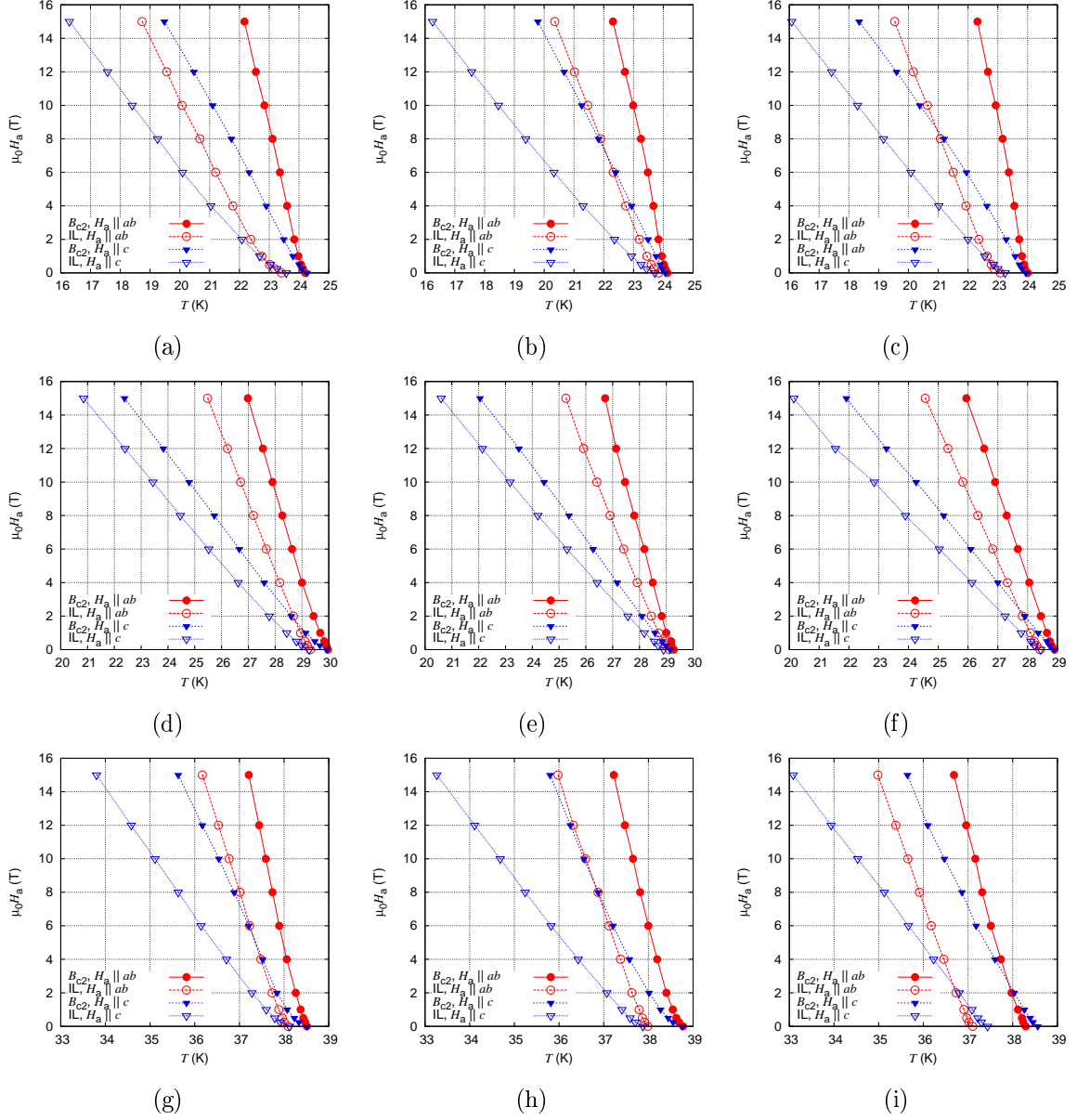


Figure 5.25: B_{c2} s and ILs of the differently doped Ba-122 single crystals: (a) Co-doped crystal, pristine; (b) Co-doped crystal, $\Phi_t = 1.8 \times 10^{21} \text{ m}^{-2}$; (c) Co-doped crystal, $\Phi_t = 3.6 \times 10^{21} \text{ m}^{-2}$; (d) P-doped crystal, pristine; (e) P-doped crystal, $\Phi_t = 1.8 \times 10^{21} \text{ m}^{-2}$; (f) P-doped crystal, $\Phi_t = 3.6 \times 10^{21} \text{ m}^{-2}$; (g) K-doped crystal, pristine; (h) K-doped crystal, $\Phi_t = 1.8 \times 10^{21} \text{ m}^{-2}$; (i) K-doped crystal, $\Phi_t = 3.6 \times 10^{21} \text{ m}^{-2}$;

higher $J_c(B = B_{sf})$. The P- and K-doped single crystals show much smaller margins between their respective B_{c2s} and B_{irr} s than the Co-doped crystal, which is one further manifestation of the highest degree of impurities and disorder in the latter system. All crystals show similar upper critical field anisotropies $\gamma = \frac{B_{c2}^{ab}}{B_{c2}^c}$ of about 2.5-3 at the maximum applied field $B = B_{c2}^{ab} = 15$ T. These gammas are comparable with values found in literature [8, 7, 102, 108].

The evaluated B_{c2s} and B_{irr} s of the irradiated crystals ($\Phi_t = 1.8 \times 10^{21} \text{ m}^{-2}$) are shown in Figs. 5.25(c), 5.25(e) and 5.25(h). A comparison with the results for the pristine samples reveals that the irradiation had no strong effect on B_{c2} . In addition, no significant influence on the irreversibility lines was found in the P-doped system. By contrast, some changes were observed for the Co- and K-doped systems. In the former, B_{irr}^{ab} shifted noticeably closer to B_{c2}^{ab} , while B_{irr}^c moved away from B_{c2}^c in the latter. In both crystals, a closer examination of the resistive transitions gives an indication for the reason behind these differences. In the case of the pristine Co-doped crystal, ρ tails off slightly before vanishing. B_{irr} is evaluated in the region of this small tail, leading to reduced values in comparison to the irradiated crystal where no tail was observed just before ρ becomes zero. The reversed effect is found in the K-doped system: ρ in the irradiated crystal shows a slight tailing off before disappearing in noise, while the pristine crystal does not have such a feature. This leads to a conclusion that the tail feature is not caused by the irradiation. It could arise due to minor differences in the doping level, inhomogeneities in the crystals or mechanical damage caused by handling and or cleaning.

The results obtained after the second irradiation step ($\Phi_t = 3.6 \times 10^{21} \text{ m}^{-2}$) are shown in Figs. 5.25(b), 5.25(f) and 5.25(i). The P-doped crystal showed only minor changes in its B_{c2s} and irreversibility lines after the second irradiation which could be traced back to the reduced T_c . By contrast, the Co- and K-doped crystals showed some more pronounced alterations of these two magnitudes. Starting with the Co-doped system, there was a clear decrease of B_{c2}^c , while B_{c2}^{ab} remained unchanged. When observing the irreversibility lines, the trend is as follows: B_{irr}^{ab} drops distinctively, while B_{irr}^c slightly decreases from the values obtained after the previous irradiation step. After taking a closer look at the respective resistive transitions for $H_a \parallel c$ and $H_a \parallel ab$ (Fig. 5.24(a) and Fig. 5.24(b)), it is possible to explain these changes at least to a degree. Both figures

reveal that the curves have a tail feature near the zero resistivity point. This is the reason for the decline of the irreversibility lines, whereby the change is more pronounced for the orientation $H_a \parallel ab$ (compare Fig. 5.25(b) to Fig. 5.25(c)). As for the change in the upper critical field B_{irr}^c , there is one quite trivial reason why it apparently declines so much in between the two irradiation steps. Fig. 5.24(a) shows a much higher magneto resistance effect in comparison to Fig. 5.23(a). Since the criterion used for the evaluation of B_{c2} is obtained from the curve at 0 T and held constant, the R increasing with B can lead to apparently smaller values for the upper critical field in this orientation. By contrast, the same sample showed almost no distinguishable magneto resistance effects in the orientation $H_a \parallel ab$. The final crystal is the K-doped one (Fig. 5.25(i)) and several changes can be found here. First of all, it is important to note the decrease in T_c (about 0.25 K). Another important thing is the relatively large difference between the values at 0 T for the two field orientations which should in reality collapse onto a single point, barring the remnant field of the superconducting magnet and the self-field induced by the small transport current. This effect is likely caused by different positioning of the temperature sensor during the two measurements. Care was taken to ensure that its position is almost same for all measurements, but it cannot be excluded that the author of this work made an experimental error in this case, resulting in the observed effect. After taking these two factors into consideration, it becomes evident that the change in the upper critical fields when comparing Fig. 5.25(i) to Fig. 5.25(h) is basically due to the reduced transition temperature. As regards the irreversibility lines, they move farther away from the respective B_{c2} as the degree of disorder in the crystal increases.

As a conclusion, the general trend found in all crystals is that the changes in the upper critical fields and the irreversibility lines are mostly due to the decrease in the transition temperature. The presence of a tail in the resistivity results in distinctively lower values of B_{irr} in the relevant cases. When linking the obtained results to the already evaluated in-plane J_c s of the crystals, it becomes apparent that high values for B_{irr} and B_{c2} do not necessarily translate to high critical currents. Continuing this line of thoughts, the role of a proper pinning landscape is once again highlighted when considering the K-doped system. There, the pristine crystal has the highest $B_{\text{irr}}(T)$, but it requires a strong pinning landscape to reach the massive currents reported in Sec. 5.3.2. The fact that $B_{c2}(T)$ does not change by much with each irradiation step means that the coherence

| Sample | $\xi_{ab}(0 \text{ K})$ (nm) | $\xi_c(0 \text{ K})$ (nm) |
|--------|------------------------------|---------------------------|
| Co#1 | 2.7 | 1.1 |
| P#2 | 3 | 1 |
| K#4 | 1.6 | 0.8 |

Table 5.4: Extrapolated coherence lengths in the pristine single crystals

lengths also remain close to constant while the anisotropy parameter also shows only minor changes (a few percent). While it is not possible to say whether the irradiation has a pronounced influence on λ and in turn on H_c and E_c , it is very tempting to assume that these magnitudes also remain close to their original values in the pristine state, thus confirming the leading role of artificial pinning centers for the high critical currents in the irradiated crystals.

The available data allows an estimation of the coherence length $\xi(0 \text{ K})$ in the three crystal types. First, the evaluated $B_{c2}^c(T)$ is used to calculate $\xi_{ab}(T) = \sqrt{\frac{\phi_0}{2\pi B_{c2}^c(T)}}$ where $\phi_0 = 2.07 \cdot 10^{-15} \text{ Wb}$ is the elementary flux quantum. Then a fit function of the form $\xi(T) = \xi(0 \text{ K})(1 - t^{1.5})^{-0.5}$ is used to estimate $\xi_{ab,0}$. Next, the coherence length $\xi_c(T) = \frac{\phi_0}{2\pi B_{c2}^c \xi_{ab}}(T)$ is calculated. A summary of the results for the pristine crystals is provided in Tab. 5.4. We find that the estimated coherence lengths at 0 K are between 0.8 and 3 nm. These figures are comparable to previous reports for these systems [6, 102, 104, 109]. Since it was already found that irradiation with fast neutrons had little impact on the B_{c2} s of the crystals, the coherence lengths also remain largely unchanged.

5.3.5 Analysis of the volume pinning force

The volume pinning force $F_p = J_c B$ can be used as an indicator for the nature of the dominant pinning regime. A study on non-layered, isotropic superconductors was performed [110]. Despite the obvious differences in Ba-122 based superconductors (layered structure, B_{c2} anisotropy), the work by Dew-Hughes is often used to deduce the dominant pinning contribution in such crystals [8, 100, 102, 111]. F_p is usually normed to its maximum value $F_p^{max}(T)$ and plotted as a function of the reduced field $b(T) = \frac{B}{B_{c2}(T)}$. The dominant pinning regime is usually deduced from the peak position and shape of the curve. However, it is important to note once again that the study by Dew Hughes handles non-layered, isotropic superconductors, whereas the Ba-122 superconducting single crystals are all layered systems with upper critical field anisotropies of about 2-3.

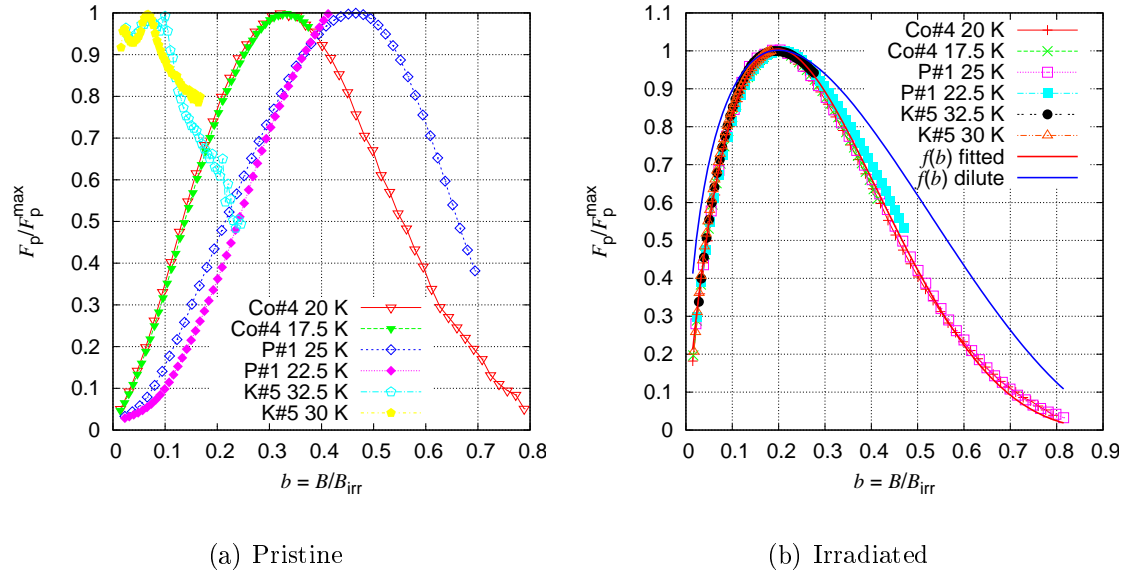


Figure 5.26: Normalized volume pinning force as a function of the reduced field in pristine (left panel) and irradiated (right panel) differently doped Ba-122 single crystals

Therefore, it is questionable whether the values excerpted from his study can be used without modifications in this case. Nevertheless, it is possible to extract valuable information, for instance the behavior of the pinning force in the differently doped crystals after irradiation.

In this work, B is normed by B_{irr} instead of B_{c2} since J_c disappears at the irreversibility field, prompting F_p to drop to zero. When discussing volume pinning force curves as a function of reduced field, a function of the form

$$f(b) = cb^n(1 - b)^m \quad (5.8)$$

is usually fitted to the experimental data. The coefficients n and m are particularly significant. In the dilute pinning limit, $n = 0.5$ and $m = 2$ [25]. Fig. 5.3.5 illustrates $\frac{F_p(b)}{F_p^{\text{max}}(b)}$ in all three crystal types in the pristine (left panel) and irradiated state (right panel) at different temperatures. It is apparent from the drastically different pinning force curves that different pinning mechanisms dominate in the the pristine crystals. As regards the results after irradiation, two additional curves are plotted, namely $f(b)$ where $c \approx 9, n \approx 0.88, m \approx 3.56$ are fitted and $f(b)$ with $n = 0.5$ and $m = 2$ as expected in the dilute pinning limit. The curves show the results obtained from VSM measurements. In

the case of Co#4 and P#1, the data acquired for $\Phi_t = 3.6 \times 10^{21} \text{ m}^{-2}$ is used, while the data from the lesser fluence $\Phi_t = 1.8 \times 10^{21} \text{ m}^{-2}$ is used for K#5. The reason is that the currents in the potassium doped crystal after irradiation to $\Phi_t = 3.6 \times 10^{21} \text{ m}^{-2}$ were so strong that the limit of the applied field in the VSM was insufficient to fully magnetize the crystal even when employing field cooling. The dependencies of $\frac{F_p(b)}{F_p^{\max}(b)}$ collapse onto a single curve for all crystals. This is an indication that the radiation induced defects govern pinning in all samples, regardless of their doping. Another interesting result is that the peak $h_{\text{peak}} \approx 0.2$ has the same position as in the dilute pinning regime, but the coefficients n and m do not coincide with the respective expected values. These are interesting findings which should be studied in more detail in a future work.

Chapter 6

Conclusion

The work done on the Ba-122 system during this thesis provided a lot of information about flux pinning. A large amount of data regarding the effects of irradiation to different fast neutron fluences on fundamental parameters such as the in-plane critical current density, transition temperature and upper critical field was presented. These numbers are of primary interest when discussing the Ba-122 family as potential candidates for technological applications. Additionally, the role played by planar defects in a single crystalline film with respect to flux pinning was interpreted successfully. It was found that in this scenario the out-of-plane Lorentz force has no influence on the critical current density, thus J_c can be mapped onto a single curve by using a single parameter, resulting in a one-dimensional pinning model. A further milestone achievement was the successful extension of the well-established pure field scaling for anisotropic superconductors. By taking into account the anisotropy of the flux lines, using geometric arguments and working within a direct summation limit, the critical current density was successfully scaled to a single curve by scaling both the field and the critical current density. The importance of this result is not least due to its independence on the researched superconductor as it only requires a uniform and isotropic defect structure consisting of spherical defects. Obtaining the last result was very challenging, not least because of the sophisticated measurement procedure necessary to extract the critical currents flowing under maximum Lorentz force. In the course of obtaining this parameter, the currents flowing under variable Lorentz force were also extracted. The availability of both these parameters offers new research possibilities. There are no quantitative studies regarding the dependence of the critical current density on Lorentz force in single crystals, let alone

in crystals with different pinning regimes. However, the novel magnetometry technique presented in this work provides an opportunity to study this phenomenon, enhancing the understanding of flux pinning not only in the Ba-122 family, but also in superconductors as a whole.

Bibliography

- [1] Y Kamihara, T Watanabe, M Hirano, and H Hosono, *Iron-Based Layered Superconductor $LaO_{1-x}F_xFeAs$ ($x = 0.05-0.12$) with $T_c = 26$ K*, J. Am. Chem. Soc. **130**, 32963297, (2008)
- [2] A S Sefat, R Jin, M A McGuire, B C Sales, D J Singh, and D Mandrus, *Superconductivity at 22 K in Co-Doped $BaFe_2As_2$ Crystals*, Phys. Rev. Lett. **101**, 117004 (2008)
- [3] M Rotter, M Tegel, and D Johrendt, *Superconductivity at 38 K in the Iron Arsenide $(Ba_{1-x}K_x)Fe_2As_2$* , Phys. Rev. Lett. **101**, 107006 (2008)
- [4] S Kasahara, T Shibauchi, K Hashimoto, K Ikada, S Tonegawa, R Okazaki, H Shishido, H Ikeda, H Takeya, K Hirata, T Terashima, and Y Matsuda *Evolution from non-Fermi-to Fermi-liquid transport via isovalent doping in $BaFe_2(As_{1-x}P_x)_2$* , Phys. Rev. B **81**, 184519(2010)
- [5] S Jiang, H Xing, G Xuan, C Wang, Z Ren, C Feng, J Dai, Z Xu, and G Cao *Superconductivity up to 30 K in the vicinity of the quantum critical point in $BaFe_2(As_{1-x}P_x)_2$* , J. Phys. Condens. Matter **21**, 382203 (2009)
- [6] C Tarantini, A Gurevich, J Jaroszynski, F Balakirev, E Bellingeri, I Pallecchi, C Ferdeghini, B Shen, H H Wen, and D C Larbalestier, *Significant enhancement of upper critical fields by doping and strain in iron-based superconductors*, Phys. Rev. B **84**, 184522 (2011)
- [7] H Q Yuan, J Singleton, F F Balakirev, S. A. Baily, G F Chen, J L Luo, and N L Wang, *Nearly isotropic superconductivity in $(Ba,K)Fe_2As_2$* , Nature **457**, 565-568 (2009)

- [8] A Yamamoto, J Jaroszynski, C Tarantini, L Balicas, J Jiang, A Gurevich, and D C Larbalestier, *Small anisotropy, weak thermal fluctuations, and high field superconductivity in Co-doped iron pnictide $Ba(Fe_{1-x}Co_x)_2As_2$* , Appl. Phys. Lett. **94**, 062511 (2009)
- [9] J D Weiss, C Tarantini, J Jiang, F Kametani, A A Polyanskii, D C Larbalestier, and E E Hellstrom, *High intergrain critical current density in fine-grain $(Ba_{0.6}K_{0.4})Fe_2As_2$ wires and bulks*, Nat. Mat. **11**, 682 (2012)
- [10] M Eisterer, M Zehetmayer, H W Weber, J Jiang, J D Weiss, A Yamamoto, and E E Hellstrom, *Effects of disorder on the superconducting properties of $BaFe_{1.8}Co_{0.2}As_2$ single crystals*, Supercond. Sci. Technol. **22**, 095011 (2009)
- [11] Y Nakajima, T Taen, Y Tsuchiya, T Tamegai, H Kitamura, and T Murakami, *Suppression of the critical temperature of superconducting $Ba(Fe_{1-x}Co_x)_2As_2$ by point defects from proton irradiation*, Phys. Rev. B **82**, 220504(R) (2010)
- [12] T Tamegai, T Taen, H Yagyuda, Y Tsuchiya, S Mohan, T Taniguchi, Y Nakajima, S Okayasu, M Sasase, H Kitamura, T Murakami, T Kambara, and Y Kanai, *Effects of particle irradiations on vortex states in iron-based superconductors*, Supercond. Sci. Technol. **25**, 084008 (2012)
- [13] C J van der Beek, S Demirdis, D Colson, F Rullier-Albenque, Y Fasano, T Shibauchi, Y Matsuda, S Kasahara, P Gierlowski, and M Konczykowski *Electron irradiation of Co, Ni, and P-doped $BaFe_2As_2$ type iron-based superconductors*, Jour. Phys. Conf. Ser. **449**, 012023 (2013)
- [14] K J Kihlstrom, L Fang, Y Jia, B Shen, A E Koshelev, U Welp, G W Crabtree, W K Kwok, A Kayani, S F Zhu, and H H Wen, *High-field critical current enhancement by irradiation induced correlated and random defects in $(Ba_{0.6}K_{0.4})Fe_2As_2$* , Appl. Phys. Lett. **103**, 202601 (2013)
- [15] A A Abrikosov, *Vliyanie razmerov na kriticheskoe pole sverkhprovodnikov vtoroi gruppy*, Dokl. Akad. Nauk SSSR **86**, 489 (1952)
- [16] V L Ginzburg and L Landau, *On the theory of superconductivity*, Zh. Eksp. Teor. Fiz. **20**, 1064 (1950)

- [17] W Meissner and R Ochsenfeld, *Ein neuer Effekt bei Eintritt der Supraleitfähigkeit*, Naturwiss. **21**, 787 (1933)
- [18] A Meshkovsky and A Schalnikov, Zh. Eksp. i Teor. Fiz. **11**, 1 (1947)
- [19] B M Balashova and Y V Sharvin, *Structure of intermediate state of superconductors*, Zh. Eksp. i Teor. Fiz. **31**, 40 (1956)
- [20] A L Schawlow and G D Devlin, *Intermediate State of Superconductors: Influence of Crystal Structure*, Phys. Rev. **110**, 1011 (1958)
- [21] Y V Sharvin, Zh. Eksp. i Teor. Fiz. **33**, 1341 (1957)
- [22] A A Abrikosov, *On the Magnetic Properties of Superconductors of the Second Group*, J. Exptl. Theoret. Phys. (U.S.S.R.) **32**, 1442-1452 (1957)
- [23] C P Bean, *Magnetization of Hard Superconductors*, Phys. Rev. Letters **8**, 250 (1962)
- [24] H London, *Alternating current losses in superconductors of the second kind*, Phys. Lett. **6**, 162 (1963)
- [25] A M Campbell and J E Evetts, *Critical Currents in Superconductors*, Adv. Physics **21**, 199 (1972)
- [26] C P Bean, *Magnetization of High-Field Superconductors*, Rev. Mod. Phys. **36**, 3139 (1964)
- [27] Poster: *Tiefe Temperaturen / Supraleitung*, Low Temperature Physics Department, Atominstytut, Vienna University of Technology
- [28] E. M. Gyorgy, R. B. van Dover, K. A. Jackson, L. F. Schneemeyer, and J. V. Waszczak, *Anisotropic critical currents in $Ba_2YCu_3O_7$ analyzed using an extended Bean model*, Appl. Phys. Lett. **55**, 283 (1989)
- [29] P W Anderson and Y B Kim, *Hard Superconductivity: Theory of the Motion of Abrikosov Flux Lines*, Rev. Mod. Phys **36**, 39-43 (1964)
- [30] L J Azevedo, W G Clark, G Deutscher, R L Greene, G B Street, and L J Suter *The upper critical field of superconducting polysulfur nitride, $(SN)_x$* , Solid State Comm. **19**, 197-201 (1976)

- [31] J G Bednorz and K A Müller *Possible high T_c superconductivity in the Ba-La-Cu-O system*, Z. Physik B, **64**, 2, 189-193 (1986)
- [32] A Gurevich, *Upper critical field and the Fulde-Ferrel-Larkin-Ovchinnikov transition in multiband superconductors*, Phys. Rev. B **82**, 184504 (2010)
- [33] P L Alireza, Y T C Ko, J Gillett, C M Petrone, J M Cole, G G Lonzarich, and S E Sebastian *Superconductivity up to 29 K in $SrFe_2As_2$ and $BaFe_2As_2$ at high pressures*, J. Phys. Condens. Matter **21**, 012208 (2009)
- [34] E Colombier, S L Budko, N Ni, and P C Canfield, *Complete pressure-dependent phase diagrams for $SrFe_2As_2$ and $BaFe_2As_2$* , Phys. Rev. B **79**, 224518 (2009)
- [35] F Ishikawa, N Eguchi, M Kodama, K Fujimaki, M Einaga, A Ohmura, A Nakayama, A Mitsuda, and Y Yamada, *Zero-resistance superconducting phase in $BaFe_2As_2$ under high pressure*, Phys. Rev. B **79**, 172506 (2009)
- [36] H Fukazawa, N Takeshita, T Yamazaki, K Kondo, K Hirayama, Y Kohori, K Miyazawa, H Kito, H Eisaki, and A Iyo, *Suppression of Magnetic Order by Pressure in $BaFe_2As_2$* , J. Phys. Soc. Jpn **77**, 105004 (2008)
- [37] K Matsubayashi, N Katayama, K Ohgushi, A Yamada, K Munakata, T Matsumoto, and Y Uwatoko, *Intrinsic Properties of AFe_2As_2 ($A = Ba, Sr$) Single Crystal under Highly Hydrostatic Pressure Conditions*, J. Phys. Soc. Jpn **78**, 073706 (2009)
- [38] J Paglione and R L Greene, *High-temperature superconductivity in iron-based materials*, Nat. Phys. **6**, 645658 (2010)
- [39] S Foner, *Versatile and Sensitive Vibrating-Sample Magnetometer*, Rev. Sci. Instrum. **30**, 548 (1959)
- [40] J Mallison, *Magnetometer Coils and Reciprocity*, J. Appl. Phys. **37**, 2514-5 (1966)
- [41] Y B Kim, C F Hempstead, and A R Strnad, *Magnetization and Critical Supercurrents*, Phys. Rev. **129**, 528 (1963)
- [42] J E Evetts, A M Campbell, and D Dew-hughes, *Flux instabilities in hard superconductors*, Phil. Mag. **10**, 339 (1964)

- [43] M Zehetmayer, *Simulation of the current dynamics in superconductors: Application to magnetometry measurement*, Phys. Rev. B **80**, 104512 (2009)
- [44] M Nakajima, S Ishida, K Kihou, Y Tomioka, T Ito, Y Yoshida, C H Lee, H Kito, A Iyo, H Eisaki, K M Kojima, and S Uchida, *Evolution of the optical spectrum with doping in $Ba(Fe_{1-x}Co_x)_2As_2$* , Phys. Rev. B **81**, 104528 (2010)
- [45] M Nakajima, S Uchida, K Kihou, C H Lee, A Iyo, and Hiroshi Eisaki, *Growth of $BaFe_2(As_{1-x}P_x)_2$ Single Crystals ($0 \leq x \leq 1$) by Ba_2As_3/Ba_2P_3 -Flux Method*, J. Phys. Soc. Jpn **81**, 104710 (2012)
- [46] K Kihou, T Saito, S Ishida, M Nakajima, Y Tomioka, H Fukazawa, Y Kohori, T Ito, S Uchida, A Iyo, C H Lee, and H Eisaki *Single Crystal Growth and Characterization of the Iron-Based Superconductor KFe_2As_2 Synthesized by KAs Flux Method*, Jour. Phys. Soc. Jap. **79**, 124713 (2010)
- [47] J Karpinsky, N D Zhigadlo, S Katrych, Z Bukowski, P Moll, S Weyeneth, H Keller, R Puzniak, M Tortello, D Daghero, R Gonnelli, I Maggio-April, Y Fasano, Ø Fischer, K Rogacki, and B Batlogg, *Single crystals of $LnFeAsO_{1-x}F_x$ ($Ln = La, Pr, Nd, Sm, Gd$) and $Ba_{1-x}Rb_xFe_2As_2$: Growth, structure and superconducting properties*, Physica C **469**, 370-380 (2009)
- [48] N Zhigadlo, S Weyeneth, S Katrych, P J W Moll, K Rogacki, S Bosma, R Puzniak, J Karpinski, and B Batlogg, *High-pressure flux growth, structural, and superconducting properties of $LnFeAsO$ ($Ln = Pr, Nd, Sm$) single crystals*, Phys. Rev. B **86**, 214509 (2012)
- [49] M Tegel *Iron pnictide superconductors*, PhD thesis Ludwig-Maximilians-Universität (München), (2011)
- [50] K Iida, S Haindl, T Thersleff, J Hänisch, F Kurth, M Kidszun, R Hühne, I Mönch, L Schultz, B Holzapfel, and R Heller, *Influence of Fe buffer thickness on the crystalline quality and the transport properties of $Fe/Ba(Fe_{1-x}Co_x)_2As_2$ bilayers*, Appl. Phys. Lett. **97** 172507 (2010)

- [51] V Mishev, W Seeböck, M Eisterer, K Iida, F Kurth, J Hänisch, E Reich, and B Holzapfel *One-dimensional pinning behavior in Co-doped BaFe₂As₂ thin films*, Appl. Phys. Lett. **103**, 232601 (2013)
- [52] Philip J W Moll, L Balicas, V Geshkenbein, G Blatter, J Karpinski, N D Zhigadlo, and B Batlogg, *Transition from slow Abrikosov to fast moving Josephson vortices in iron pnictide superconductors*, Nat. Mat. **12**, 134 (2013)
- [53] Quantum Design, *Measuring Large Moment Samples in the Magnetic Property Measurement System (MPMS)*, Application Note, 1014-824 (2003)
- [54] V Mishev, M Zehetmayer, D X Fischer, M Nakajima, H Eisaki, and M Eisterer *Interaction of vortices in anisotropic superconductors with an isotropic defect landscape*, Submitted to Phys. Rev. X
- [55] M Weigand, *Untersuchung des Mischzustandes von Wismut-Strontium-Kalzium-Kupfer-Oxid-(Bi2223)-Einkristallen*, Diploma thesis TU Wien, (2006)
- [56] R Schöppl, *Grain Boundaries in High Temperature Superconductors*, PhD thesis TU Wien, (2011)
- [57] T Williams and C Kelley, <http://www.gnuplot.info/>, Version 4.6.x, (2012)
- [58] M C Frischherz, M A Kirk, J P Zhang , and H W Weber, *Transmission electron microscopy of defect cascades in YBa₂Cu₃O_{7-δ} produced by ion irradiation*, Philos. Mag. A **67**, 1347 (1993)
- [59] M Zehetmayer, F Sauerzopf, H W. Weber, J Karpinski, and M Murakami, *Comparative study of sequential neutron irradiation and annealing effects in superconducting YBa₂Cu₃O_{7-δ} , Y₂Ba₄Cu₈O₁₆ and NdBa₂Cu₃O_{7-δ} single crystals*, Phys. C **383**, 232 (2002)
- [60] M Eisterer, R Fuger, M Chudy, F Hengstberger, and H W Weber, *Neutron irradiation of coated conductors*, Supercond. Sci. and Technol. **23**, 1 (2010)
- [61] M Chudy, R Fuger, M Eisterer, and H W Weber, *Characterization of commercial YBCO coated conductors after neutron irradiation*, IEEE Trans. Appl. Supercond. **21**, 3162 (2011)

- [62] R Flükiger, T Baumgartner, M Eisterer, H W Weber, and T Spina, *Variation of $(J_c/J_{c0})_{max}$ of Binary and Ternary Alloyed RRP and PIT Nb₃Sn Wires Exposed to Fast Neutron Irradiation at Ambient Reactor Temperature*, IEEE Trans. Appl. Supercond. **23**, 1 (2013)
- [63] T Baumgartner, M Eisterer, H W Weber, R Flükiger, C Scheuerlein, and L Bottura, *Effects of neutron irradiation on pinning force scaling in stateoftheart Nb₃Sn wires*, Supercond. Sci. Technol. **27**, 015005-1 (2014)
- [64] M Eisterer, M Zehetmayer, S Tönies, H W Weber, M Kambara, N Hari Babu, D A Cardwell, and L R Greenwood, *Neutron irradiation of MgB₂ bulk superconductors*, Supercond. Sci. Technol. **15**, 9 (2002)
- [65] M Zehetmayer, M Eisterer, J Jun, S M Kazakov, J Karpinski, B Birajdar, O Eibl, and H W Weber, *Fishtail effect in neutron-irradiated superconducting MgB₂ single crystals*, Phys. Rev. B **69**, 054510 (2004)
- [66] M Weigand, M Eisterer, E Giannini, and H W Weber, *Mixed state properties of Bi₂Sr₂Ca₂Cu₃O_{10+δ} single crystals before and after neutron irradiation*, Physical Review B, 81 (2010), S. 014516-1 - 014516-7.
- [67] M Eisterer, H W Weber, J Jiang, J D Weiss, A Yamamoto, A A Polyanskii, E E Hellstrom, and D C Larbalestier, *Neutron irradiation of SmFeAsO_{1-x}F_x* Supercon. Sci. Technol. **22**, 065015-1 (2009)
- [68] M Eisterer, V Mishev, M Zehetmayer, N D Zhigadlo, S. Katrych, and J Karpinski, *Critical current anisotropy in Nd-1111 single crystals and the influence of neutron irradiation*, Supercond. Sci. Technol. **27**, 044009-1 (2014)
- [69] L Civale, A D Marwick, M W McElfresh, T K Worthington, A P Malozemoff, F H Holtzberg, J R Thompson, and M A Kirk, *Defect independence of the irreversibility line in proton-irradiated Y-Ba-Cu-O crystals*, Phys. Rev. Lett. **65**, 1164 (1990)
- [70] S Harrington, J MacManus-Driscoll, and J H Durrell *Practical vortex diodes from pinning enhanced YBa₂Cu₃O_{7-δ}*, Appl. Phys. Lett. **95**, 022518 (2009)

- [71] J Hänisch, K Iida, S Haindl, F Kurth, A Kauffmann, M Kidszun, T Thersleff, J Freudenberger, L Schultz, and B Holzapfel, *J_c Scaling and Anisotropies in Co-Doped Ba-122 Thin Films*, IEEE Trans. Appl. Supercond. **21**, 2887 (2011)
- [72] B Maiorov, Q X Jia, H Zhou, Y Li, A Kursunovic, J L MacManus-Driscoll, T J Haugan, P N Barnes, S R Foltyn, and L Civale, *Effects of the Variable Lorentz Force on the Critical Current in Anisotropic Superconducting Thin Films*, IEEE Trans. Appl. Supercond. **17**, 3697 (2007)
- [73] M Tachiki and S Takahashi, *Strong vortex pinning intrinsic in high- T_c oxide superconductors*, Solid State Commun. **72**, 1083 (1989)
- [74] S R Foltyn, L Civale, J L MacManus-Driscoll, Q X Jia, B Maiorov, H Wang, and M Maley, *Materials science challenges for high-temperature superconducting wire*, Nat. Mat. **6**, 631 (2007)
- [75] V Mishev, M Eisterer, and H W Weber, *Magnetization measurements in oblique magnetic fields: The influence of geometry and correlated pinning*, Poster: International Conference on Materials and Mechanisms of Superconductivity (M2S 2012), Washington, USA; 29.07.2012 - 03.08.2012
- [76] T Giamarchi and P Le Doussal, *Phase diagrams of flux lattices with disorder*, Phys. Rev. B **55**, 6577 (1997)
- [77] G Mikitik and E H Brandt, *Peak effect, vortex-lattice melting line, and order-disorder transition in conventional and high- T_c superconductors*, Phys. Rev. B **64**, 184514 (2001)
- [78] M Iavarone, R Di Capua, G Karapetrov, A E Koshelev, D Rosenmann, H Claus, C D Malliakas, M G Kanatzidis, T Nishizaki, and N Kobayashi, *Effect of magnetic impurities on the vortex lattice properties in NbSe₂ single crystals*, Phys. Rev. B **78**, 174518 (2008)
- [79] J Hecher, M Zehetmayer, and H W Weber, *How the macroscopic current correlates with the microscopic flux-line distribution in a type-II superconductor: an experimental study*, Supercond. Sci. Technol. **27**, 075004 (2014)
- [80] G Blatter, V B Geshkenbein, and A Larkin, *From isotropic to anisotropic superconductors: A scaling approach*, Phys. Rev. Lett. **68**, 875 (1992)

- [81] R A Klemm and J R Clem, *Lower critical field of an anisotropic type-II superconductor*, Phys. Rev. B **21**, 1868 (1980)
- [82] J Gutiérrez, A Llordés, J Gázquez, M Gibert, N Romà, S Ricart, A Pomar, F Sandiumenge, N Mestres, T Puig, and X Obradors, *Strong isotropic flux pinning in solution-derived $YBa_2Cu_3O_{7-x}$ nanocomposite superconductor films*, Nat. Mater. **6**, 367 (2007)
- [83] T G Holesinger, L Civale, B Maiorov, D M Feldmann, J Y Coulter, D J Miller, V A Maroni, Z Chen, D C Larbalestier, R Feenstra, X Li, Y Huang, T Kodenkandath, W Zhang, M W Rupich, and A P Malozemoff, *Progress in nano-engineered microstructures for tunable high-current, high temperature superconducting wires*, Adv. Mater. Prog. Rep. **20**, 391 (2008)
- [84] A Llordés, A Palau, J Gázquez, M Coll, R Vlad, A Pomar, J Arbiol, R Guzmán, S Ye, V Rouco, F Sandiumenge, S Ricart, T Puig, M Varela, D Chateigner, J Vanacken, J Gutiérrez, V Moshchalkov, G Deutscher, C Magen, and X Obradors, *Nanoscale strain-induced pair suppression as a vortex-pinning mechanism in hightemperature superconductors*, Nat. Mater. **11**, 329 (2012)
- [85] M Kidszun, S Haindl, T Thersleff, J Hänisch, A Kauffmann, K Iida, J Freudenberger, L Schultz, and B Holzapfel, *Critical Current Scaling and Anisotropy in Oxypnictide Superconductors*, Phys. Rev. Lett. **106**, 137001 (2011)
- [86] G Blatter, M V Feigelman, V B Geshkenbein, A I Larkin, and V M. Vinokur, *Vortices in high-temperature superconductors.*, Rev. Mod. Phys. **66**, 1125 (1994)
- [87] B Maiorov, S A Baily, H Zhou, O Ugurlu, J A Kennison, P C Dowden, T G Holesinger, S R Foltyn, and L Civale, *Synergetic combination of different types of defect to optimize pinning landscape using $BaZrO_3$ -doped $YBa_2Cu_3O_{7-\delta}$* , Nature Mater. **8**, 398-404 (2009)
- [88] S C Wimbush, N J and Long, *The interpretation of the field angle dependence of the critical current in defect-engineered superconductors.*, New J. Phys. **14**, 083017 (2012)
- [89] G Ercolano, M Bianchetti, S C Wimbush, S A Harrington, H Wang, J H Lee, and J L MacManus-Driscoll, *State-of-the-art flux pinning in $YBa_2Cu_3O_{7-\delta}$ by the creation of*

- highly linear, segmented nanorods of $Ba_2(Y/Gd)(Nb/Ta)O_6$ together with nanoparticles of $(Y/Gd)_2O_3$ and $(Y/Gd)Ba_2Cu_4O_{8-x}$* , Supercond. Sci. Technol. **24**, 095012 (2011).
- [90] M Chudy, R Fuger, M Eisterer, and H W Weber, *Characterization of Commercial YBCO Coated Conductors After Neutron Irradiation.*, IEEE Tran. Appl. Supercond. **21**, 3162 (2011).
- [91] H W Weber, H Böck, E Unfried, and L R Greenwood *Neutron flux density distribution in the central irradiation thimble of the TRIGA Mark II reactor in Vienna*, **10** biennial U.S. TRIGA users' conference
- [92] F M Sauerzopf, H P Wiesinger, W Kritscha, H W Weber, G W Crabtree, and J Z Liu, *Neutron-irradiation effects on critical current densities in single-crystalline $YBa_2Cu_3O_{7-\delta}$* , Phys. Rev. B **43**, 3091 (1991)
- [93] H W Weber, F Nardai, C Schwinghammer, and R K Maix, *Neutron irradiation of NbTi with different flux pinning structures*, Adv. Cryog. Engin. **28**, 329 (1982)
- [94] R Flükiger, T Baumgartner, M Eisterer, H W Weber, T Spina, C Scheuerlein, C Senatore, A Ballarino, and L Bottura, *Variation of $(J_c/J_{c0})_{max}$ of Binary and Ternary Alloyed RRP and PIT Nb3Sn Wires Exposed to Fast Neutron Irradiation at Ambient Reactor Temperature*, IEEE Trans. Appl. Supercond. **23**, 8001404 (2013)
- [95] I I Mazin, D J Singh, M D Johannes, and M H Du, *Unconventional Superconductivity with a Sign Reversal in the Order Parameter of $LaFeAsO_{1-x}F_x$* , Phys. Rev. Lett. **101**, 057003 (2008)
- [96] F Wang, H Zhai, Y Ran, A Vishwanath, and D H Lee, *Functional Renormalization-Group Study of the Pairing Symmetry and Pairing Mechanism of the FeAs-Based High-Temperature Superconductor*, Phys. Rev. Lett. **102**, 047005 (2009)
- [97] Y Senga and H Kontani, *Impurity-induced in-gap state and T_c in sign-reversing s-wave superconductors: analysis of iron oxypnictide superconductors*, New J. Phys. **11**, 035005 (2009) s
- [98] D Watanabe, T Yamashita, Y Kawamoto, S Kurata, Y Mizukami, T Ohta, S Kasahara, M Yamashita, T Saito, H Fukazawa, Y Kohori, S Ishida, K Kihou, C H Lee, A

- Iyo, H Eisaki, A B Vorontsov, T Shibauchi, and Y Matsuda *Doping evolution of the quasiparticle excitations in heavily hole-doped $Ba_{1-x}K_xFe_2As_2$: A possible superconducting gap with sign-reversal between hole pockets*, Phys. Rev. B **89**, 115112 (2014)
- [99] B Shen, P Cheng, Z Wang, L Fang, C Ren, L Shan, and H H Wen, *Flux dynamics and vortex phase diagram in $Ba(Fe_{1-x}Co_x)_2As_2$ single crystals revealed by magnetization and its relaxation*, Phys. Rev. B **81**, 014503 (2010)
- [100] L Fang, Y Jia, J A Schlueter, A Kayani, Z L Xiao, H Claus, U Welp, A E Koshelev, G W Crabtree, and W K Kwok, *Doping- and irradiation-controlled pinning of vortices in $BaFe_2(As_{1-x}P_x)_2$ single crystals*, Phys. Rev. B **84**, 140504(R) (2011)
- [101] L Fang, Y Jia, V Mishra, C Chaparro, V K Vlasko-Vlasov, A E Koshelev, U Welp, G W Crabtree, S Zhu, N D Zhigadlo, S Katrych, J Karpinski, and W K Kwok, *Huge critical current density and tailored superconducting anisotropy in $SmFeAsO_{0.8}F_{0.15}$ by low-density columnar-defect incorporation*, Nat. Comm. **4**, 2655 (2013)
- [102] D L Sun, Y Liu, and C T Lin, *Comparative study of upper critical field H_{c2} and second magnetization peak H_{spin} in hole- and electron-doped $BaFe_2As_2$ superconductor*, Phys. Rev. B **80**, 144515 (2009)
- [103] R T Gordon, H Kim, N Salovich, R W Giannetta, R M Fernandes, V G Kogan, T Prozorov, S L Budko, P C Canfield, M A Tanatar, and R Prozorov, *Doping evolution of the absolute value of the London penetration depth and superfluid density in single crystals of $Ba(Fe_{1-x}Co_x)_2As_2$* , Phys. Rev. B **82**, 054507 (2010)
- [104] C Chaparro, L Fang, H Claus, A Rydh, G W Crabtree, V Stanev, W K Kwok, and U Welp, *Doping dependence of the specific heat of single-crystal $BaFe_2(As_{1-x}P_x)_2$* , Phys. Rev. B **85**, 184525 (2012)
- [105] K Hashimoto, K Cho, T Shibauchi, S Kasahara, Y Mizukami, R Katsumata, Y Tsuruhara, T Terashima, H Ikeda, M A Tanatar, H Kitano, N Salovich, R W Giannetta, P Walmsley, A Carrington, R Prozorov, and Y Matsuda, *A Sharp Peak of the Zero-Temperature Penetration Depth at Optimal Composition in $BaFe_2(As_{1-x}P_x)_2$* , Science **336**, 1554 (2012)

- [106] G Li, W Z Hu, J Dong, Z Li, P Zheng, G F Chen, J L Luo, and N L Wang, *Probing the Superconducting Energy Gap from Infrared Spectroscopy on a $Ba_{0.6}K_{0.4}Fe_2As_2$ Single Crystal with $T_c=37$ K*, Phys. Rev. Lett **101**, 107004 (2008)
- [107] D Fischer, *Anisotropie der kritischen Ströme in Eisensupraleitern*, Master thesis <http://permalink.obvsg.at/AC11434181>, (2014)
- [108] U Welp, R Xie, A E Koshelev, W K Kwok, H Q Luo, Z S Wang, G Mu, and H H Wen, *Anisotropic phase diagram and strong coupling effects in $Ba_{1-x}K_xFe_2As_2$ from specific-heat measurements*, Phys. Rev. B **79**, 094505 (2009)
- [109] Y Yin, M Zech, T L Williams, X F Wang, G Wu, X H Chen, and J E Hoffman *Scanning Tunneling Spectroscopy and Vortex Imaging in the Iron Pnictide Superconductor $BaFe_{1.8}Co_{0.2}As_2$* , Phys. Rev. Lett. **102**, 097002 (2009)
- [110] D Dew-Hughes, *Flux pinning mechanisms in type II superconductors*, Phil. Mag. **30**, 293 (1974)
- [111] K S Pervakov, V A Vlasenko, E P Khlybov, A Zaleski, V M Pudalov, and Y F Eltsev, *Bulk magnetization and strong intrinsic pinning in Ni-doped $BaFe_2As_2$ single crystals*, Supercond. Sci. Technol. **26**, 015008 (2013)

Curriculum Vitae

Name: Ventsislav Mishev

Date of birth: June 13, 1986

Place of birth: Sofia, Bulgaria

Address: Hohlweggasse 32/2/6, 1030 Vienna, Austria

Education and experience:

2011-2015 PhD research at the Atominstitut, Vienna University of Technology; Project Assistant

2005-2011 Physics Studies at the Vienna University of Technology
Diploma thesis: Aufbau eines Anisotropie-Messplatzes für Zugversuche an YBCO-Bandleitern

2000-2005 Fremdsprachgymnasium Tsar Ivan Asen der 2., Sofia, Bulgarien

1993-2000 31. Mittelschule für Fremdsprachen und Management, Sofia, Bulgarien

Publications

'One-dimensional pinning behavior in Co-doped BaFe₂As₂ thin films', V Mishev, W Seeböck, M Eisterer, K Iida, F Kurth, J Hänisch, E Reich, and B Holzapfel, Applied Physics Letters **103**, 232601 (2013)

'Critical current anisotropy in Nd-1111 single crystals and the influence of neutron irradiation', M Eisterer, V Mishev, M Zehetmayer, N D Zhigadlo, S. Katrych, and J Karpinski, Superconductor Science and Technology **27**, 044009-1 (2014)

'Interaction of vortices in anisotropic superconductors with an isotropic defect landscape', V Mishev, M Zehetmayer, D X Fischer, M Nakajima, H Eisaki, and M Eisterer, Submitted to Phys. Rev. X